



UNIVERSIDAD NACIONAL AUTÓNOMA DE MÉXICO

POSGRADO EN CIENCIA E INGENIERÍA EN MATERIALES

INSTITUTO DE INVESTIGACIONES EN MATERIALES

**FABRICATION AND STUDY OF ELECTROLUMINESCENT
STRUCTURES BASED ON SILICON NANOCRYSTALS**

TESIS

**QUE PARA OPTAR POR EL GRADO DE
DOCTORA EN CIENCIA E INGENIERÍA EN MATERIALES**

PRESENTA

ANA LUZ MUÑOZ ROSAS

TUTOR

**DR. JUAN CARLOS ALONSO HUITRÓN
INSTITUTO DE INVESTIGACIONES EN MATERIALES**

COMITÉ TUTOR

**DRA. ANA MARÍA MARTÍNEZ VÁZQUEZ
INSTITUTO DE INVESTIGACIONES EN MATERIALES**

**DR. JUAN CARLOS CHEANG WONG
INSTITUTO DE FÍSICA**

CIUDAD DE MÉXICO, OCTUBRE DE 2016



Universidad Nacional
Autónoma de México

Dirección General de Bibliotecas de la UNAM

Biblioteca Central



UNAM – Dirección General de Bibliotecas
Tesis Digitales
Restricciones de uso

DERECHOS RESERVADOS ©
PROHIBIDA SU REPRODUCCIÓN TOTAL O PARCIAL

Todo el material contenido en esta tesis esta protegido por la Ley Federal del Derecho de Autor (LFDA) de los Estados Unidos Mexicanos (México).

El uso de imágenes, fragmentos de videos, y demás material que sea objeto de protección de los derechos de autor, será exclusivamente para fines educativos e informativos y deberá citar la fuente donde la obtuvo mencionando el autor o autores. Cualquier uso distinto como el lucro, reproducción, edición o modificación, será perseguido y sancionado por el respectivo titular de los Derechos de Autor.

“Be less curious about people and more curious about ideas”

M. Curie-Sklodowska

To my nephew and nieces

My shining stars

Acknowledgements

I feel fortunate for having studied in the National University Autonomous of Mexico; my gratitude to this institution for opening this door of opportunity.

I am also grateful of the financial funding I received through the CONACyT fellowship.

My thankfulness to my supervisor, Dr. Juan Carlos Alonso Huitrón for let me carry out all ideas that came to me during my PhD studies in his laboratory. From the successes and mistakes I learned a lot.

I would like to thank my committee members, Dra. Ana María Martínez Vázquez, and especially to Dr. Juan Carlos Cheang Wong for his observations and opinions about this thesis.

My gratitude to Dr. Arturo Rodríguez Gómez for his continuous support, collaboration and discussion throughout the course of this work. Likewise, I would like to express my sincere gratitude to Dr. Manuel Corona Galindo for his guidance and encouragement through all my post-graduate studies.

I would like to express my acknowledgement to all people whose help has been essential for the developing of this work:

- M. A. Canseco Martínez, for his assistance in FTIR measurements.
- C. Flores Morales for the AFM measurements.
- L. Huerta Arcos for the XPS measurements.
- O. Novelo Peralta and J. E. Romero for the SEM images.
- J. A. Martínez and R. Hernández for the HRTEM images.

Additionally, I would want to thank and acknowledge my thesis examination committee, Dra. Alicia María Oliver y Gutiérrez, Dr. Augusto García Valenzuela, Dr. Arturo Rodríguez Gómez, and Dr. Mathieu Christian Anne Hautefeuille. All their observations and opinions have improved significantly this work.

My thanks to all the friends and coworkers whom I had the pleasure to meet and work with them during my researching work. From each one I have learned something.

Last but not least, my love and gratitude to all my family for their continual support and encouragement over the years.

Abstract

Since the discovering of light emission from nanostructured silicon, attributed to a quantum confinement effect, great efforts have been carried out to integrate the silicon as a light source compatible with complementary-metal-oxide-semiconductor (CMOS) technology. Even though many types of electroluminescent devices based on silicon technology have been developed, its efficiency is still low. In this work, the experimental results of improved efficiency of silicon quantum dots (SiQDs)-based-light emitting devices are presented.

In order to fabricate these devices, the chemical and optical properties of the SiQDs active film under different thermal treatments were studied. Metal-insulating-metal (MIM) devices were fabricated using four different thicknesses of the active film to investigate the electroluminescence behavior through this configuration. From these devices, the sample with better optical and electrical properties was chosen to further investigation.

Moreover, the optical and morphological properties of gold nanoparticles were studied in order to properly achieve its coupling with the emission from SiQDs. A two-fold photoluminescence intensity enhancement was observed when the interdistance between the SiQDs film and gold nanoparticles (2.9 nm diameter) was 10 ± 2 nm. This separation distance was achieved through a non-radiative silicon nitride layer. It was demonstrated that the metal-insulating-semiconductor (MIS) devices fabricated using these layered structures with noble metal nanostructures, exhibit also higher electroluminescence efficiency with regard to those reference devices without gold metal.

Contents

INTRODUCTION	1
Thesis objectives.....	4
Outline of this thesis.....	5
CHAPTER I. BACKGROUND	6
1.1 Silicon Photonics.....	6
1.2 Silicon for photonics applications	7
1.3 Photoluminescence from silicon quantum dots	8
1.2 Light emitting devices based in silicon	10
CHAPTER II. EXPERIMENTAL METHODOLOGY	12
2.1 Deposition techniques	12
2.1.1 Remote Plasma Chemical Vapor Deposition (RPECVD) system	12
2.1.2 DC Sputtering.....	14
2.1.3 Ultrasonic Spray Pyrolytic deposition.....	15
2.2 Characterization techniques.....	17
2.2.1 Fourier Transform Infrared Spectroscopy (FTIR).....	17
2.2.2 Ultraviolet-visible spectroscopy (Uv-vis).....	19
2.2.3 Null ellipsometry	19
2.2.4 X-Ray Photoelectron Spectroscopy (XPS)	21
2.2.5 Atomic Force Microscopy (AFM).....	22
2.2.6 High Resolution Transmission Electron Microscopy (HRTEM).....	24
2.2.7 Scanning electron microscopy.....	26
2.2.8 Photoluminescence measurements.....	27
2.2.9 Electroluminescence measurements	28
CHAPTER III. PHOTOLUMINESCENCE OF THE SILICON QUANTUM DOTS ACTIVE FILM	29
3.1 Quantum confined model	29
3.2 Surface passivation.....	31
3.3 Defect related luminescence	33
3.4 SiQDs embedded in a chlorinated silicon nitride matrix (SiN _x :Cl).....	35
3.5 Deposition of SiQDs thin films and thermal treatments.....	35
3.5.1 Fabrication process steps.....	36
3.5.2 Chemical and optical characterization.....	36
3.6 Conclusions	41
CHAPTER IV. LIGHT EMISSION OF SILICON QUANTUM DOTS DEVICES	42
4.1 Current transport processes in metal-semiconductor contacts.....	42

4.2 Basic conduction process in insulators	43
4.3 SiQDs-based electroluminescent devices on glass	45
4.3.1 Fabrication process steps.....	45
4.4 Thickness effect of the active film on the EL properties.....	47
4.4.1 Optical and electrical characterization	47
4.5 Conclusions	62
CHAPTER V. PHOTOLUMINESCENCE ENHANCEMENT.....	63
5.1 Luminescent films in the vicinity of nanostructured noble metals	63
5.2 Gold nanostructures fabricated by sputtering	64
5.2.1 Morphological and optical characterization	64
5.3 Coupling of SiQDs and Au nanostructures fields.....	68
5.3.1 Fabrication process steps.....	70
5.3.2 Optical characterization	72
5.4 Conclusions	75
CHAPTER VI. METAL-INSULATOR-SEMICONDUCTOR DEVICES.....	76
6.1 Metal-insulator-semiconductor capacitors	76
6.2 First stage of fabrication of metal-insulator-semiconductor devices based on SiQDs	77
6.2.1 Fabrication process steps.....	78
6.2.2 Optical and electrical characterization	80
6.3 Second stage of fabrication of metal-insulating-semiconductor devices based on SiQDs ..	90
6.3.1 Optical and electrical characterization	90
6.4 Conclusions	93
Bibliography	95
Appendix A	98
Appendix B	100

INTRODUCTION

Currently, it is technologically feasible to produce metal oxide semiconductor field effect transistors (MOSFETs) with gate lengths smaller than 50 nm (figure 1) and silicon dioxide thickness less than 1.3 nm [1]. The foregoing, due to some intrinsic qualities of thermal silicon dioxide like thickness control, uniformity, stable interface with silicon substrate and low density of defects at the interface, which has allowed the scale integration of devices and therefore better performance.

However, at very low scale the roughness plays a critical role on the increase of leakage current through the insulator and moreover when the thickness decreases to an atomic level the local electronic structure of bulk silicon dioxide is not reproduced [1]. Additionally, as the number of transistors in an integrated circuit increases, more interconnecting wires must be included in the chip to link those transistors together. When information is sent along these wires high power consumption appears in the circuit as well as problems related with speed-limiting circuit delay. Further scaling will increase parasitic capacitance effects in the wires controlling the performance of the integrated circuit (bottleneck of interconnect technology). In order to overcome these disadvantages temporarily, high conductive materials like copper and dielectrics of low k like infill materials have been employed.

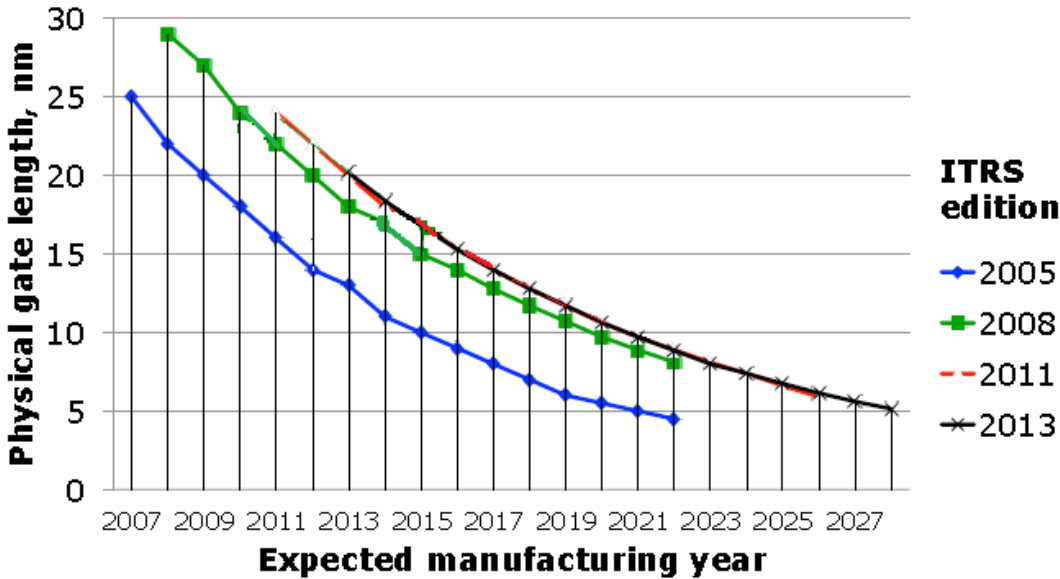


Figure (1) International technology roadmap for semiconductors (ITRS) projections for gate lengths (nm) vs. expected manufacturing year for 2005, 2008, 2011 and 2013 editions [2].

Despite the fact the technological limit, the demand of functionality for on-chip circuits continues and have pushed the industry to recognize that electronics technology will progressively require

integration with photonics to keep up scaling, either through monolithic or heterogeneous integration [3]. Moreover, the need of high speed data transmission (nowadays over a bit-rate of 10 Gb/s) makes photonic interconnects more suitable to implement than electrical interconnects in which losses are important. Therefore, high efficiency and low dimensionality of chips could be achieved if optical interconnects and electronic circuits perform like a system.

The essential photonics components of figure (2) convert an initially optical signal to an electrical signal to get data transmission on a common silicon platform. A high quantum efficiency laser implemented on-chip or off-chip can provide the optical power to an optical circuit [3].

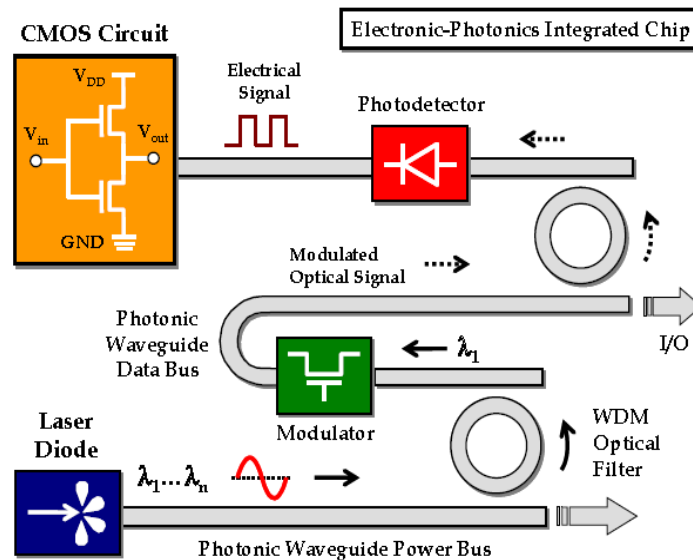


Figure (2) Basic building blocks required to convert an optical signal to an electrical signal on a common silicon platform [3].

Some of the advantages to accomplish a scheme like the latter include elimination of delay, cross talk, and power dissipation in signal propagation, even though important new challenges will be introduced. The chip-scale integration of the very best photonic technologies available today, e.g., laser sources, interferometric modulators, dense wavelength division multiplexing (WDM), and low loss planar waveguides will be demanded by optical interconnects. These all will be necessary components of an optical interconnect system that can offer an acceptable per-wire information bandwidth-per-watt figure of merit [4].

Different approaches of integration based in silicon photonics have been developed successfully during years to obtain waveguides, modulators and detectors. However, until now an all-silicon source (light emission diode (LED) or laser) has still not been demonstrated because of its indirect band gap and consequently very long radiative lifetimes (ms range), which means that most of the excited carriers recombine non-radiatively [5].

Nowadays, the complementary metal oxide semiconductor (CMOS) devices in electronic circuits are fabricated basically of silicon. Likewise, the only viable technology for an on chip silicon-based light injection laser is a hybrid technology using III-V semiconductors. Despite this fact, researchers have tried to exploit different strategies to turn silicon into a light emission material like band structure engineering or quantum confinement effect in low dimensional silicon [5].

The discovery of bright visible light emission at room temperature in porous silicon (PS) which had been etched under carefully controlled conditions by Canham [6] in 1990, motivated investigation on quantum confinement of carriers in other silicon-based nanostructures including nanoclusters, quantum wells, wires, and dots. Furthermore, the possibility of electroluminescence (EL) was also explored to obtain silicon-based optoelectronic devices. To achieve efficient and stable emission from electrically excited silicon-based components is an important issue since this would lead to the integration of light sources such as light emission devices (LED) or lasers. However, until now electroluminescent structures fabricated with porous silicon exhibit some problems in stability and operation voltage [7].

An alternative to using porous silicon has been the fabrication of silicon-based light emitting devices (LEDs) built with silicon quantum dots (SiQDs) or silicon nanocrystals (Si-nc) embedded in a silica matrix. These films take advantage of the quality and stability of the SiX_x/Si interface and the improved emission properties of quantum confined silicon. Additionally, compatible techniques with CMOS technology are commonly used to form SiQDs like Plasma Enhanced Chemical Vapor Deposition (PECVD) [8-10], Low Pressure Chemical Vapor Deposition (LPCVD) [11] and silicon ion implantation into silicon-based dielectrics [12, 13]. These techniques are based on the deposition of sub-stoichiometric silica films, with a significant excess of silicon, sometimes followed by a high temperature annealing.

Moreover, in the past few years great effort has been directed towards the system silicon rich silicon nitride (SRN) to obtain silicon quantum dots due to its luminescence properties, as well as the better control of carrier injection for light emitting devices. Silicon nitride based structures offer, over oxide based active materials, a considerable reduction in the electron hole injection barriers at the silicon/silicon nitride interfaces, resulting in the fabrication of low-voltage electroluminescent devices with improved electrical stability.

However, external quantum efficiency reported in this type of light emission devices is still not enough to be competitive with the modern requirements of microelectronics. With the aim of improving efficiency of SiN_x -based LEDs some methods have been developed as multilayers [14, 15], high doped thin films or metal nanostructures [16-18]. With respect to the last method, increasing the radiative recombination rate by coupling excitons to localized surface plasmons has been recently investigated, even though the role of this effect is unclear in photoluminescence and electroluminescence enhancement.

Thesis objectives

The aim of this thesis was the fabrication and study of efficient electroluminescent devices based on silicon quantum dots embedded in chlorinated silicon nitride thin films deposited by RPECVD (Remote Plasma Enhanced Chemical Vapor Deposition) system.

To obtain the chemical, physical and electrical properties of the luminescent structures the following specific goals were carried out:

- ❖ The chemical and optical characterization of the active film of SiQDs undergoing different thermal treatments in order to know how different temperatures in subsequent process stages could change properties of the layer.
- ❖ Fabrication of the simple electroluminescent MIM (metal-insulating-metal) devices: ZnO:Al/SiQDs/Al on glass, and investigation of their luminescent and electrical properties as a function of the thickness of the active film, in order to get the optimal thickness for further investigation.
- ❖ Additionally, the photoluminescence enhancement of these films was studied by means of gold nanostructures in their vicinity. In order to vary the interdistance between gold nanostructures and SiQDs, multilayered structures of chemically different silicon nitride were deposited.
- ❖ Furthermore, metal-insulator-semiconductor (MIS) light emission devices were fabricated using the more efficient configurations obtained in the previous points in order to investigate the optical and electrical response of these structures when they are electrically excited.

Outline of this thesis

The chapters in this thesis are organized as follows:

Chapter 1 and 2 are the background about silicon photonics and the experimental methodology employed in this work, respectively.

In chapter 3, a short introduction of some luminescence models developed to explain the emission in SiQDs films are presented. Additionally, in this chapter the chemical and optical properties of the silicon quantum dots films deposited in this work under different thermal treatments are studied.

Chapter 4 describes briefly the conduction mechanisms in insulators. Likewise, in this section of the thesis the fabrication and characterization of metal-insulator-metal (MIM) devices is carried out. In these devices the thickness of the insulating film (the active SiQDs film) was varied.

Chapter 5 presents the optical and morphological characterization of gold monolayers of different thicknesses deposited by sputtering. The coupling of the emission from SiQDs in the vicinity of the noble metal nanostructures was studied systematically through photoluminescence measurements.

Finally, in chapter 6 the more efficient structures obtained in chapter 5 were chosen to fabricate metal-insulating-semiconductor (MIS) electroluminescent devices in order to investigate, at least indirectly, the efficiency in these light emission devices in the vicinity of metal nanostructures.

CHAPTER I. BACKGROUND

1.1 Silicon Photonics

Photonics is the science associated with generation, processing, transmission and detection of light. Some of the principal photonic devices are lasers, waveguides, modulators, detectors, and optical fibers. In the last decade, optical communication technologies have required to develop low cost and efficient optical solutions to the continuous necessity of connection. At present, optical devices are large, bulky and mostly not fabricated from silicon. Most optical components are made from III–V-based compounds such as indium phosphide (InP), gallium arsenide (GaAs) or the electro-optic crystal lithium niobate (LiNbO₃) [19]. These optical devices are often assembled from discrete components and typically with very little automation. The net result of all this is that these optical devices are relatively expensive. The future of optical networking rests on the ability to bring optical technology may be some day directly to the microprocessor.

The convergence of Si-based electronics with photonics has largely required the development of hybrid technologies for devices like light emitters and modulators which are often both expensive and complicated to produce. Even though, integrated photonic circuits where active III-V lasers and diodes are combined with passive silicon based optical components are commercially available, the principal focus is on combining III–V semiconductor laser diodes with Si integrated circuits for optical fiber communications or optical interconnects. However, this is not an easy task. For GaAs and Si the lattice mismatch of 4% between them, the different thermal expansion coefficients and the fact that Si is a fast diffusing impurity for III–V semiconductors generate severe difficulties in maintaining the required low defect density in GaAs for laser production. Moreover, dislocations produced by relaxation of the GaAs epitaxial layer are detrimental to device performance and life [20].

To overcome these disadvantages, the extensive experience in Si fabrication and processing could be put to best use to obtain optoelectronic and photonic devices created entirely from Si-based materials. The major failing in Si-based optoelectronic devices remains the need of suitable light emitters and lasers. Research in this field is rapidly progressing and to improve the low light emission in bulk Si ($\sim 10^{-6}$ quantum efficiency at 300K in standard electronic grade silicon, where the quantum efficiency is defined as the ratio of the number of photons generated over the number of excited electron–hole pairs), various approaches have been proposed and actively explored. Some of these are Si_{1-x}Ge_x quantum wells or Si/Ge superlattice structures, which depend on band structure engineering, while others rely on quantum confinement effects in low dimensional structures, as typified by silicon quantum dots or porous silicon (PS).

1.2 Silicon for photonics applications

The energy band structure in semiconductors is derived from the relationship between the energy and momentum of a charge carrier. The band structure is often quite complex because it depends not only on the crystal structure but also on the bonding between atoms, the respective bond lengths, and the chemical species. For example silicon has the space lattice of diamond which is face-centered cubic with tetrahedral bonding. The diamond structure is an example of the directional covalent bonding found in column IV of the periodic table. For silicon the lattice constant is $a=5.43 \text{ \AA}$ [21]. In zinc-blende semiconductors such as GaAs, the Ga and As atoms lie on separate sublattices, and thus the inversion symmetry of Si is lost in polar III–V binary compounds. The difference in the crystal structures underlies the disparate electronic and optical properties of Si and GaAs .

The dispersion relations for the energy $E(k)$ of an electron (positive energy) or hole (negative energy) for wave vectors k within the first Brillouin zone of Si and GaAs are shown in figure (3).

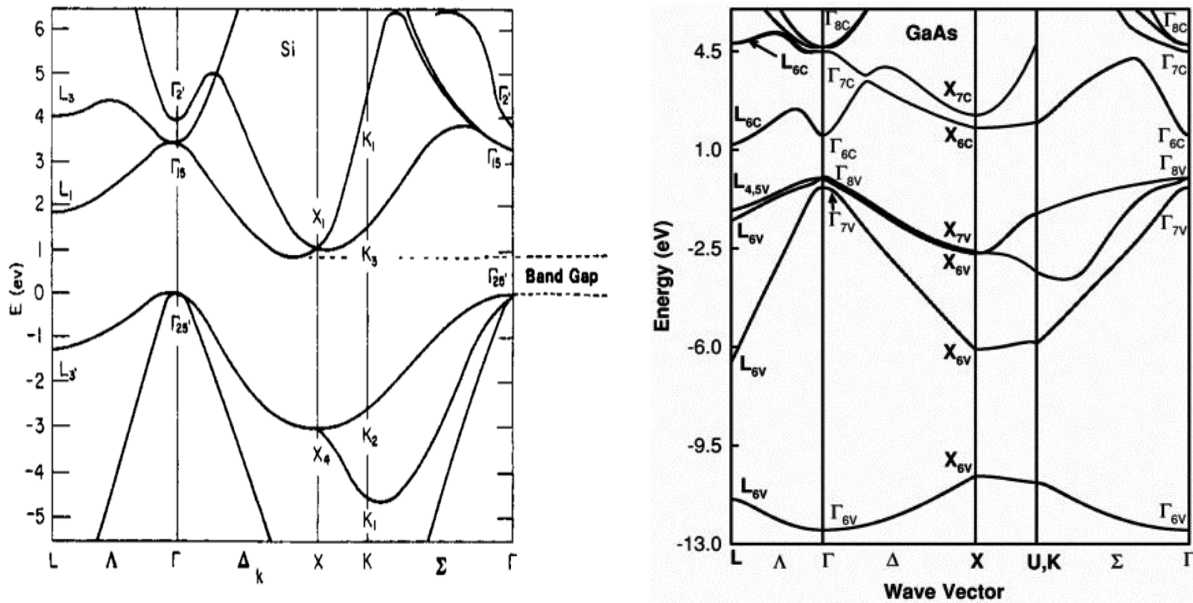


Figure (3). Band structures of Si and GaAs.

The notable difference between Si and GaAs is that the degeneracy in the $\Gamma_{25'}$ band maximum at $k=0$ is removed in the case of GaAs, because of the spin-orbit interaction, into Γ_7 and Γ_8 sub-bands. In the case of Si, the lowest point in the conduction band occurs away from high symmetry points near the X point at the Brillouin zone boundary (along $\langle 001 \rangle$), whereas in GaAs it occurs at the Γ point. The energy gap in a semiconductor is defined as the separation between this absolute conduction band minimum and the valence band maximum at the Γ point. For GaAs, the energy gap is classified as direct, because the maximum and minimum occur at the same k and an electronic transition can occur directly at $k = 0$ between initial and final states having the same wave vector.

Correspondingly, Si is termed an indirect gap semiconductor, because the initial and final states have different wave vectors [20].

Energy and momentum is conserved in optical transitions. Since silicon is an indirect semiconductor the electron–hole radiative recombination process can only occur in Si with the assistance of a further process to conserve the momentum. In pure silicon this occurs via the transfer of the electron momentum to a phonon that is created with equal and opposite wave vector to that of the initial state in the conduction band. Such a three-body process is quite inefficient compared with direct gap recombination. Thus, the probability of spontaneous emission is very low for Si and high for GaAs. The spontaneous emission or radiative lifetime in silicon is very long (millisecond range) while in direct gap III–V semiconductors it is short (nanosecond range).

The indirect band-gap of Si is 1.12 eV at room temperature (Fig. 3). The weak band-to-band emission at this energy in the near infrared was observed using visible light excitation or by forward-biasing Si diodes. Electron–hole pairs created either optically or electrically in Si may bind to each other to form excitons, which can be either free or tied to impurities or defects. Exciton recombination dominates the optical emission process at low temperatures and is characterized by very narrow emission lines. At high temperatures, however, excitons are thermally dissociated and emission is due to direct band-to-band recombination. Excitonic emission is under active investigation in quantum well, wire, and dot structures corresponding to carrier confinement in one, two and three dimensions, respectively.

1.3 Photoluminescence from silicon quantum dots

Investigation for light generation and amplification in silicon has found that the optical and electronic properties of silicon can be tuned by controlling its bandgap. This can be achieved with the reduction of silicon in the nanoregime to less than its Bohr’s exciton radius (4.3 nm). Therefore, the properties of silicon at nanoscale behave totally different than bulk. This form of silicon is known as nanocrystals (Si-nc) or quantum dots (SiQDs). Moreover, the electronic properties also depend on the chemical environment near to SiQDs. Hence, SiQDs and its adjacent chemical environment play an important role in the performance of the modern photoelectronic devices [22]. When silicon is confined in a dielectric material having bandgap higher than Si (e.g. SiO₂, silicon nitride (Si₃N₄), and silicon carbide (SiC)), the electrons wavefunctions overlap and shift the energy level on higher side. Some of the parameters of SiQDs/dielectric matrices such as QD size, barrier height, QD spacing, etc. have an important role in determining its optical and electrical properties. High Resolution Transmission Electron Microscopy (HRTEM) image of SiQDs embedded in a dielectric matrix is shown in figure (4).

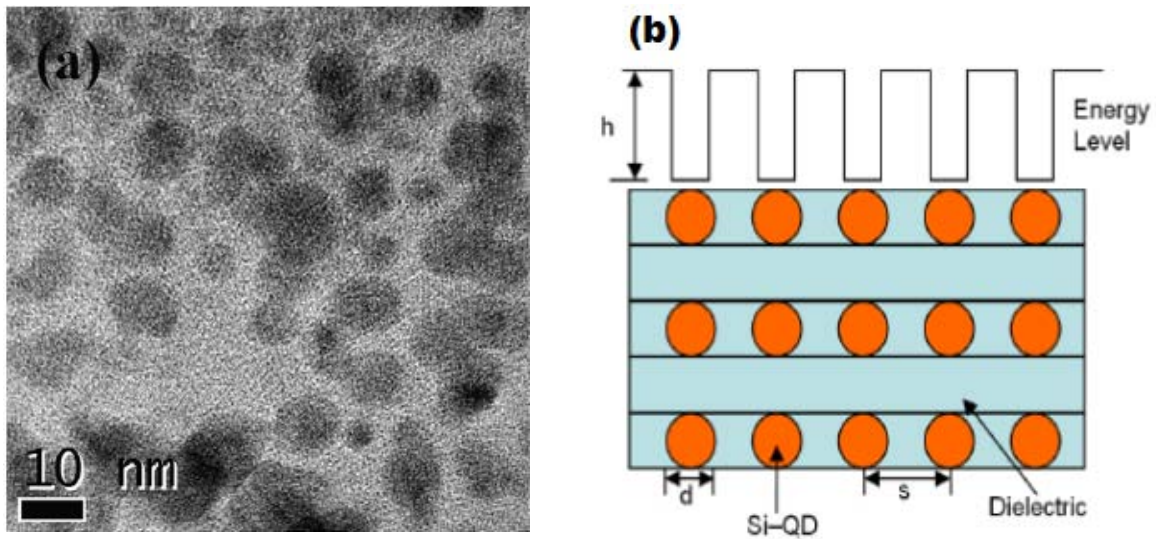


Figure (4) (a) HRTEM micrograph of silicon nanocrystals embedded in a dielectric matrix [23]. (b) Schematic set of SiQDs embedded in a dielectric with dot size d , inter-dot separation s , and energy barrier height h [22].

Thus, through the manipulation of the system dimension and shape at the nanometer scale it is possible to obtain some desirable properties. Investigation of phenomena such as the Stokes shift (difference between absorption and emission energies), the PL emission energy versus nanocrystals size, the doping properties, the radiative lifetimes, the nonlinear optical properties, the quantum-confined Stark effect (QCSE), and more can give a fundamental contribution to the understanding of how the optical response of such systems can be tuned.

Silicon nanocrystals have been produced through several techniques including annealing of Si-rich oxide, electrochemical etching, laser-assisted processing, solution synthesis, ion implantation, plasma chemical vapor deposition, sputtering and annealing of Si/dielectric superlattices. The annealing induces a precipitation transformation where the metastable Si-rich dielectric film decomposes into two phases: Si clusters and a matrix, which is closer in composition to the equilibrium (stoichiometric) composition. Once nucleation occurs with the formation of critically sized nuclei, cluster growth is governed by processes of coalescence or ripening, which minimizes the overall surface energy of the system by promoting the growth of large clusters at the expense of smaller clusters. Taking into account these principles of nucleation and growth, the parameters of Si content, annealing temperature, and annealing time can be used to fabricate nanocrystal ensembles with the desired size and density [24].

Moreover, single doping has been investigated both in spherical and in faceted-like Si-nc with the incorporation of group III (B and Al), group IV (C and Ge), and group V (N and P) impurities. Si-nc of spherical form are built with all the Si atoms contained within a sphere of a defined radius and terminating the surface dangling bonds with H, meanwhile the faceted Si-nc are built from a shell-by-shell construction process that starts from a central atom and adds shells of atoms continually. The substitutional impurity site is the one of the Si atom at the center of the silicon nanocrystal. Distortions occur in the neighborhood of the impurity sites and the bond lengths show dependence with respect to the size and shape of the silicon nanocrystals [25]. Additionally, another option to

overcome the physical limitation of silicon for optical applications has been embed rare-earth elements within silicon nanostructures to exploit quantum confined effect to change the electronic structure of semiconductor hosts in such a way as to enhance the radiative efficiency of the rare-earth dopant [24].

1.2 Light emitting devices based in silicon

Oleg Vladimirovich Losev discovered light emission from rectifier diodes made of zinc oxide and silicon carbide crystal around mid-1920s. Losev determined in his first paper on the light emission devices (LED), the current threshold for the start of light emission from the point contact between a metal wire and a silicon carbide crystal and he was able to record the spectrum of this light. The researcher realized the ‘cold’ (non-thermal) nature of the emission, measured its current threshold and understood that LED emission was related to diode action [26].

The electroluminescence (EL) is defined as the emission in excess of blackbody radiation excited by an electric field, and this effect can arise from a variety of systems under different conditions. Some examples are gas discharges and emission due to impact ionization in thin films. The most efficient kind of electroluminescence is that caused by carrier injection in semiconductors. Recently there has been a great commitment to obtain technologically viable and efficient light emission from silicon both in the visible and infrared regions of the spectrum. A wide range of combination of Si-based materials and fabrication methods have been used and demonstrated so far for electroluminescence [5].

In the visible region porous silicon (PS) has attracted much interest due to the property that it luminesces efficiently even at room temperature. PS has been applied in a wide variety of applications, such as insulating layer in the silicon-on-insulator (SOI), a sensing layer in chemical sensors, a sacrificial layer in micromachining, in optoelectronic, photovoltaic device and biomedical applications among others [27]. While in porous silicon liquid-contact devices exhibit EL with high external quantum efficiencies comparable to that of PL, the EL efficiency of industrially important solid-state-contact devices was quite low at the early stage. The efficiency has been improved up to about 0.01%–0.2% by using PS layers made by anodizing *pn* junctions [7]. However, there remain some problems related to the performance of the devices made of porous silicon as well as the need of wet processing, not compatible with CMOS technology.

With regard to optical gain materials based on silicon, Er-doping has been the expected choice, tracing the technical success of Er-doping into silica fiber. It was found in 1997, that the Er^{3+} emission is strongly enhanced by using crystalline Si-nc as sensitizers in silica when co-doped with Er. Er-doped Si-nc have been widely considered as one of the most promising Si based gain materials, independently of its aggregation phase. LEDs of SiO_2 doped with Er have been demonstrated to show 0.2% power efficiency [5]. In this system silicon nanoparticles are able to transfer its excitonic energy to Er ions, and LEDs emitting under this principle have been proved. Despite of promising results, insufficient results about the signal enhancement and little progress on the device development using Er doped Si-nc has been made until now. Some reasons for this fact

include strong carrier absorption, no increase of emission cross-section, and the low fraction of Er^{3+} ions coupled to Si-nc.

One of the main advantages of using Si-nc into silicon dioxide or silicon nitride as nonlinear optical material relies on their full process compatibility with ruling CMOS technology, which has allowed the attainment of practical, low cost, compact and low switching power all-silicon devices. It has also been reported that the self-organization of the nc-Si (nanocrystalline silicon) in the layer-grown direction could be promoted in nc-Si superlattice structures, through which resonant tunneling occurs and facilitates the carrier transport perpendicular to the layers [28, 29]. Improved carrier injection in superlattices is achieved by reducing the barrier thickness to a value where direct tunneling occurs. This fact decreases driving voltage making more reliable devices. Enhanced PL and EL by easy charge tunneling into the silicon nanocrystals, suggested higher power efficiency in multilayer LED.

Moreover, some groups have studied light emission enhancement of silicon quantum dots coupled to metal nanostructures of silver (Ag) and gold (Au) by means of light extraction efficiency or increased spontaneous emission.

F. Wang et al. [18] reported the enhanced local electric field from silver nanoparticles with different sizes on EL when the metal was deposited onto SiN_x luminescence layers. They achieved to tailor the EL wavelength of SiN_x -based LEDs by the tuning of dipolar resonance peaks of Ag nanoparticles. The EL modulation independent of the voltage was achieved by the adjustment of the sizes of Ag nanoparticles from 40 to 240 nm and the EL intensity variation by injected currents. They found that the increase of the dimension of Ag nanoparticles red-shifted the EL peaks. Likewise, in the same group D. Li et al [17] studied electroluminescence efficiency enhancement from silicon nitride-based light emitting devices (SiN_x -based LEDs) by introducing a nanostructural silver layer underneath the matrix. They showed the improvement of the EL efficiency and the efficiency droop phenomenon in their devices by using elongated Ag nanostructures with the diameter of the longer axis ~ 400 nm and that of the shorter axis ~ 240 nm formed after a rapid thermal treatment. They attributed the higher current injection obtained to the enhanced local electromagnetic fields at the interface between the SiN_x matrix and the substrate.

Also, luminescent emission has been reported in III-V quantum well light emitting diodes in [30] and [31] through the incorporation of metal nanoparticles (~ 15 nm) or nanostructures in the vicinity of the light emitter film, respectively. These works found increased spontaneous emission rate and an improvement of the internal quantum efficiency in the coupled samples with metal nanostructures.

All previous groups who have worked with the addition of noble metal structures in light emitting devices have attributed the significantly enhanced radiative recombination rates via the Purcell effect which takes place when energy of excitons from the active layer is close to the electron vibration energy of surface plasmons (SP).

CHAPTER II. Experimental methodology

In this chapter the main deposition techniques used for fabrication of the luminescent and non-luminescent thin films employed in this thesis will be reviewed. Additionally, the chemical, optical, and electrical characterization techniques utilized for analysis of the samples are also described.

2.1 Deposition techniques

2.1.1 Remote Plasma Chemical Vapor Deposition (RPECVD) system

Chemical vapor deposition (CVD) is a technique for synthesizing materials in which chemical precursors in vapor phase are thermally decomposed and react to form a solid film at some surface. The occurrence of a chemical reaction is central to this means of thin film growth, as is the requirement that the reactants must start out in the vapor phase. Ability to control the components of the gas phase, and the physical conditions of the gas phase, the solid surface, and the envelope that surrounds them determines our capability to control the properties of the thin films that are produced. The sequential process of deposition starts from the initial vapor phase and progresses through the next series of quasi steady-state sub-processes (figure (5)):

- Diffusion of gaseous reactants to the surface.
- Adsorption of the reacting species on to surface sites, often after some migration on the surface.
- Surface chemical reaction between the reactants, usually catalyzed by the surface.
- Desorption of the reaction by-products.
- Diffusion of the by-products away from the surface.
- Incorporation of the condensed solid product into the microstructure of the growing film.

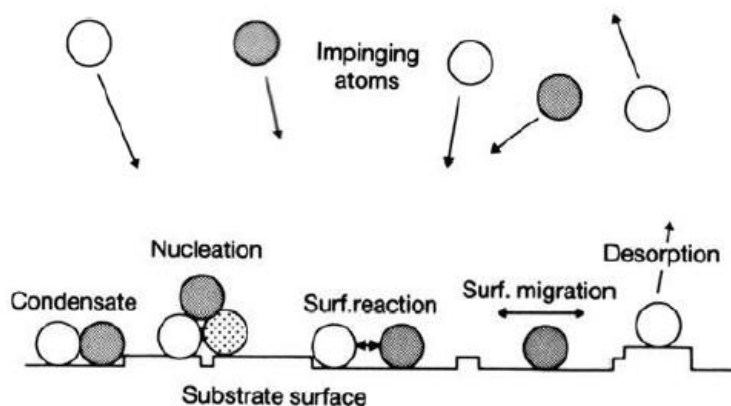


Figure (5) Schematic of events that occur around the substrate surface. Summation of these events leads to deposition on the wafer [32].

Interactions involving charged particles produced in a plasma have been effectively utilized in various CVD processes to reduce reaction temperature, which is needed for lowering the

temperature in microelectronics processes. The lowering of the activation energy through the formation of excited species X^* allows the forward reaction to proceed at lower substrate temperatures or at increased rates for the same temperature when compared with thermal CVD.

Thus, instead of depend on thermal energy to begin and sustain chemical reactions, plasma enhanced chemical vapor deposition (PECVD) uses an rf-induced glow discharge to transfer energy into the reactant gases. The latter allows the substrate to remain at a lower temperature than in low pressure chemical vapor deposition process (LPCVD). An rf electric field applied to a low pressure gas generate the plasma, thereby accelerating free electrons from ionized atoms within the discharge region. After this process the electrons gain sufficient energy from the electric field so they collide with gas molecule, and then a gas-phase dissociation and ionization of the reactant gases (e.g. silane and nitrogen or oxygen-containing species) can occur. The energetic species (predominantly radicals) are adsorbed on the film surface. The radicals usually have high sticking coefficients, and also appear to migrate easily along the surface after adsorption. Upon being adsorbed on the substrate, they are subjected to ion and electron bombardment, rearrangements, reactions with other adsorbed species, new bond formations and film formation and growth. Adatom rearrangement includes the diffusion of the adsorbed atoms onto stable sites and concurrent desorption of reaction products. Desorption rates are dependent on substrate temperature, and higher temperatures produce films with fewer entrapped by-products [33].

A schematic of the deposition system used in this thesis is shown in figure (6). The entrance chamber for inward of samples and the main chamber of deposition were home designed and manufactured by the company MV-Systems Inc. The main vacuum-deposition chamber (26 500 cm³ total volume) contained a boron–nitride hot plate, coupled to a proportional and integral differential temperature controller which was able to rise substrate temperatures from ambient up to 700 °C. The top part of the chamber consists of a quartz tube 4 in. in diameter and 20 cm in height. This quartz tube was surrounded by a water-cooled copper coil that at the same time was responsible for the power transfer from the radio frequency (rf) source (13.56 MHz) to the plasma. An initial pressure of 10⁻⁶Torr in the main chamber was settled by means of a turbomolecular-mechanical vacuum-pump system [34].

For depositing silicon nanocrystals embedded in a chlorinated silicon–nitride matrix the gases used in this work were SiH₂Cl₂, NH₃, Ar and H₂. NH₃ and Ar gases were fed into the plasma zone of the chamber from the top end of the quartz tube. Meanwhile, the SiH₂Cl₂ and H₂ gases were introduced under the plasma by means of dispersal rings laid a few centimeters over the substrate holder. The flow rate of gases was controlled automatically by means of MKS electronic mass-flow meters.

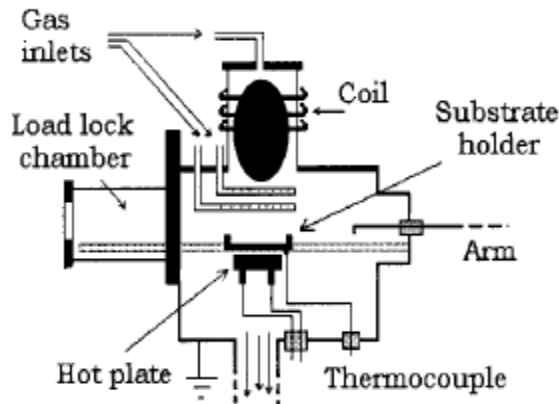


Figure (6) Schematic diagram of the RPECVD system used in this work. The NH_3 and Ar gases were supplied from the top inlet line. The SiH_2Cl_2 and H_2 gases were fed downstream through one dispersal ring [34].

2.1.2 DC Sputtering

Sputtering is the mechanism in which atoms are dislodged from the surface of a material by collision with high energy particles. As can be seen in figure (7) a target of the material to be deposited is located inside a vacuum chamber where it is connected to the negative terminal of a DC power supply. Facing the cathode/target is the substrate, which may be electrically floating, grounded or biased. An inert working gas, typically Ar, is introduced and serves as the medium in which an electrical glow discharge is initiated and sustained. Imposed by the electric field, ions of the working gas, Ar^+ , accelerate at high energy towards the target material, causing sputtering of target atoms upon impact with the cathode. The sputtered atoms transit through the discharge and condense onto the substrate, thus providing film growth. When the DC voltage is first applied to the electrodes, a small number of charge carriers initially present in the working gas create a small current. Due to inelastic collisions in the gas more electron-ion pairs are created, and the current density increases. The Ar^+ ions bombard the cathode surface, resulting in the generation of secondary electrons from the cathode surface (and sputtering of target atoms). The secondary electrons are accelerated away from the cathode and increase the ionization of the gas via inelastic collisions. This charge multiplication causes the current to increase rapidly. When the applied voltage is so high that the number of Ar^+ ions produced by collisions with one secondary electron are sufficiently high to regenerate another secondary electron, the discharge becomes self-sustaining and starts to glow. The light emitted from the discharge is due to excitation of gas atoms. The degree of ionization in a typical self-sustaining DC glow discharge or plasma is $\sim 10^{-4}$ [35].

The secondary-electron emission coefficient, i.e. the number of secondary electrons emitted at the cathode per incident ion, is about 0.1 for most metals when bombarded with ~ 100 eV Ar^+ . Thus, in order to sustain the plasma the probability of collisions between electrons and neutral gas atoms has to be sufficiently high. If the gas pressure is too low, the collision probability is small due to a large

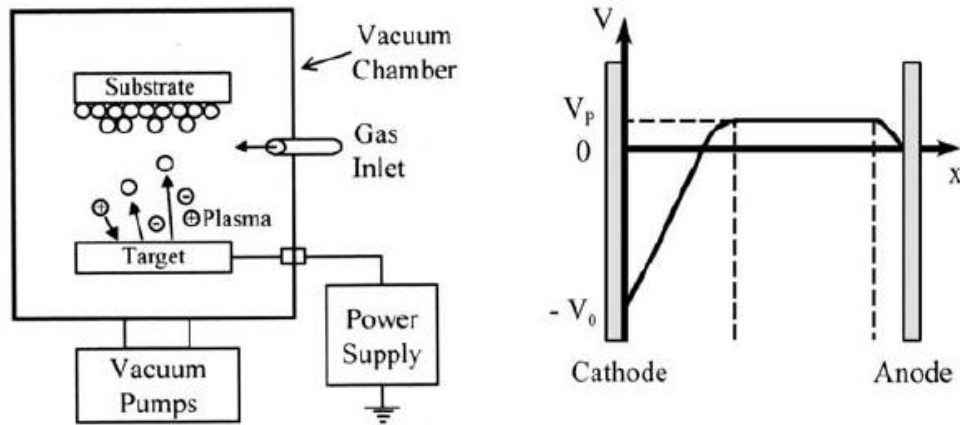


Figure (7) (a) Plot of a simple DC sputtering, (b) Schematic voltage distribution across a DC glow discharge [35].

electron mean free path, which causes loss of electrons to the chamber walls, and the number of ionized gas atoms to be inadequate. On the other hand, at too high pressures frequent collisions prevent the electrons from acquiring sufficient energy to ionize gas atoms, which will eventually quench the discharge. This means that at either extreme the ion-generation rates are low and very high voltages are required to sustain the plasma. An optimum pressure range, typically around 1–10 Pa, exists for simple DC sputtering systems, where a self-sustained glow discharge can be created at reasonable voltages, usually 200–1000 V [35].

In this work, very thin films of Au were deposited using a magnetron sputtering Cressington 108 Sputter Coater with Au target (99.9999% purity) in 0.8 mbar argon atmosphere. Quartz, glass and crystalline silicon were used as substrates.

2.1.3 Ultrasonic Spray Pyrolytic deposition

Spray pyrolysis has been applied to deposit a wide variety of thin films. These films were used in various devices such as solar cells, sensors, electrochromic devices and solid oxide fuel cells. Parameters that affect the quality of the deposited film include solution flow rate, substrate temperature, precursor solution and the size of droplets. The substrate surface temperature is the most critical parameter as it influences film roughness, cracking, crystallinity, etc. Typical spray pyrolysis equipment consists of an atomizer, precursor solution, substrate heater, and temperature controller. A variety of inexpensive metal salts can be used as precursors. Large scale production is possible due to simple equipment and mild operating conditions.

Two major disadvantages of conventional spray pyrolysis are related to particle morphology and phase homogeneity. However, this has largely been remedied by the introduction of ultrasonic nebulizers which produce a fine, homogeneous mist. Ultrasonic spray pyrolysis has the advantages of low cost, simple and continuous operation, high purity, uniform particle size distribution, controllable size from micrometer to submicrometer and excellent control of chemical uniformity and stoichiometry in a mixed oxide system.

Many processes occur either sequentially or simultaneously during film formation by spray pyrolysis. These processes include precursor solution atomization, droplet transport and evaporation, spreading on the substrate, drying and decomposition of the precursor salt. Understanding these processes will help to improve film quality. Thin film deposition using spray pyrolysis can be divided into three main steps: atomization of the precursor solution, transportation of the resultant aerosol and decomposition of the precursor on the substrate. Four types of processes that may occur during deposition are shown in figure (8). During process 1, the droplet splashes on the substrate, vaporizes, and leaves a dry precipitate in which decomposition occurs. In process 2, the solvent evaporates before the droplet reaches the surface and the precipitate impinges upon the surface where decomposition occurs. In process 3, the solvent vaporizes as the droplet approaches the substrate, then the solid melts and vaporizes (or sublimates) and the vapor diffuses to the substrate to undergo a heterogeneous reaction there. This is true CVD. In process 4, at the highest temperatures, the metallic compound vaporizes before it reaches the substrate and the chemical reaction takes place in the vapor phase [36].

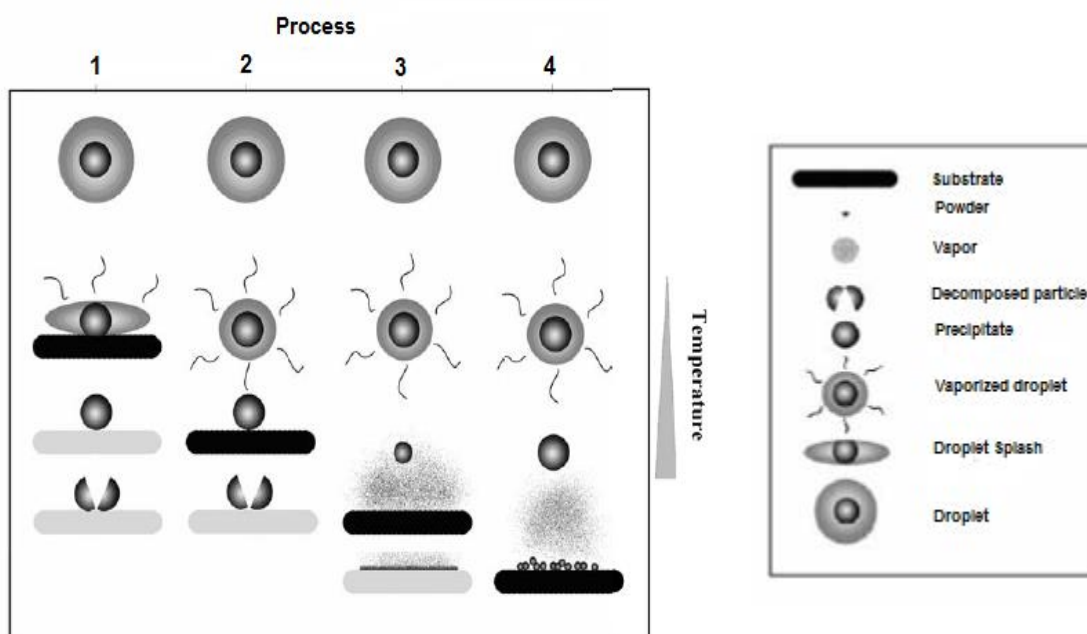


Figure (8) Schematic depicting different deposition processes that occur as the nozzle-to-substrate distance and deposition temperature change [37].

The type of spray technique used in this study was ultrasonic spray pyrolysis. In this method, the precursor solution was nebulized for depositing transparent conductive contacts (TCC) layers of ZnO:Al. The precursors utilized for depositing these TCC layers were zinc acetate and aluminum acetylacetonate. The TCC films were deposited on silicon and glass substrates at 450°C for ~20 minutes. Thickness of $1 \pm 0.2 \mu\text{m}$ of ZnO:Al gave rise a sheet resistance of 70-150 Ω/\square and transmittance of 70-80% from 450nm to 1100nm . A schematic of the deposition method is depicted in figure (9).

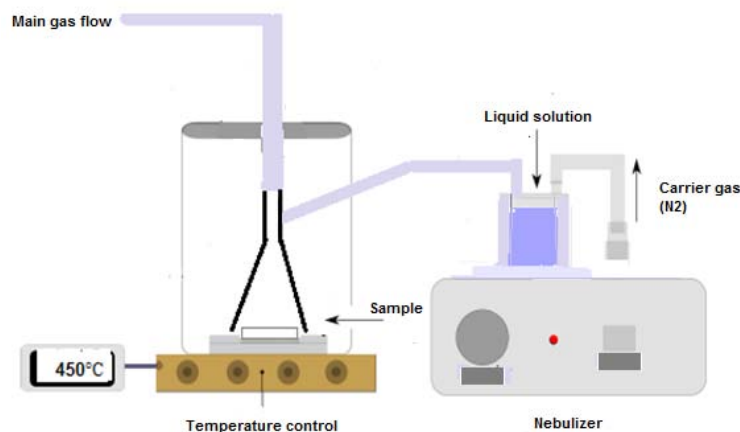


Figure (9) Schematic diagram of the ultrasonic method used to deposit TCC films.

2.2 Characterization techniques

2.2.1 Fourier Transform Infrared Spectroscopy (FTIR)

Fourier Transform Infrared spectroscopy (FTIR) is a powerful and widely applicable spectroscopy method implemented to identify chemical functional groups. An FTIR spectrometer is an analytical instrument used to study materials in the gas, liquid or solid phase. FTIR has broad application in many fields of science and engineering. Over the years, FTIR spectroscopy has become one of the most important tools for both qualitative and quantitative characterization of organic and inorganics materials, and in particular, polymers, and silicon compounds such as silicon nitrides and silicon oxides.

FTIR spectroscopy is based on the interaction of infrared light with molecules. The energy absorptivity of chemical bands creates their FTIR spectrum. Mid-infrared light is defined as light in the range of wavenumbers between 4000 and 400 cm^{-1} . All materials above absolute zero (-273.15 °C) emit infrared (IR) light. However, when molecules are radiated by infrared light, it can be absorbed and the absorbed energy causes vibration in the atomic bonds. Specific atomic groups tend to absorb infrared light at particular wavenumbers, regardless of the response of other chemical bonds in the rest of the molecule. The fact that different atomic groups absorb at different IR wavenumbers (cm^{-1}) can be used to identify the structure of molecules. The plot of measured infrared absorbance versus wavenumber is called the infrared spectrum. The intensity of the IR absorption band is proportional to the rate of change of the dipole moment in a molecule, with respect to the displacement of the atoms. However, molecules with inherent dipole moments demonstrate stronger responses than molecules with induced dipole moments. Therefore, groups such as -NH and -OH with strong dipole moments generally give strong absorption bands.

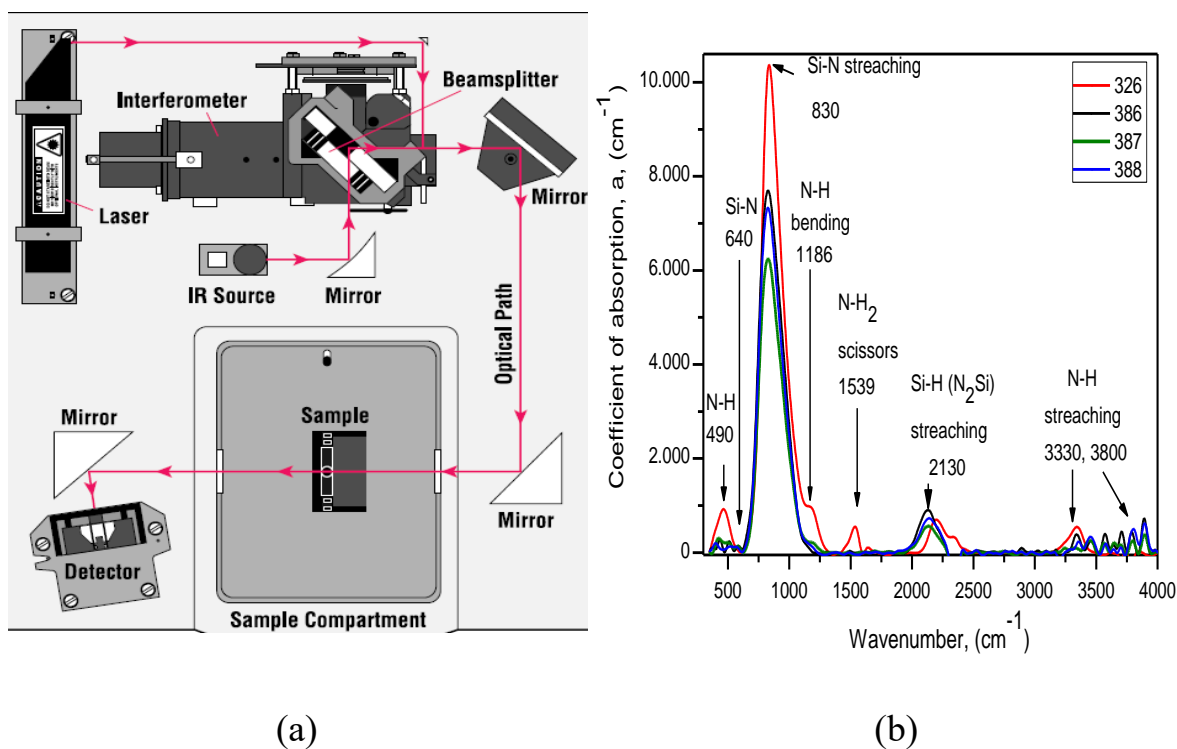


Figure 10 (a) Basic layout of a simple FTIR spectrometer, (b) IR spectra of different compositions of silicon nitride.

The FTIR spectrometer consists of an infrared light source and detector, a laser light source and detector, moving mirrors and several of fixed mirrors. A simple spectrometer layout is shown in figure (10a). The design of infrared spectrometers is based on the idea of the two-beam interferometer originally designed by Michelson in 1891. The Michelson interferometer is a device that can divide a beam of infrared light into two parts and then recombine them after they travel different paths. The difference between these paths is called the optical path difference. Therefore, the beam splitter is the centerpiece of the interferometer. The beam splitter is often made out of a thin germanium plate coated with potassium bromide (KBr). Potassium bromide does not split the IR light, but it is a substrate that protects the germanium layer from the environment. The germanium splitter reflects about 50% of the incident light and at the same time transmits the remaining 50%. One part of this split light travels to a moving interferometer mirror while the other part travels to the stationary interferometer mirror. The two mirrors reflect both beams back to the beam splitter where the light rays recombine. When the two light beams recombine at the beam splitter, an interference pattern is generated. As long as the path difference is equal to multiples of the wavelength, the beams are in phase, called zero path difference. When these beams add together, an intense wave will be produced. Recombining two beams that are out of phase will produce a weak wave. As the moving mirror travels back and forth, the beam brightness varies from intense to weak. The variation of light intensity versus optical path difference is called the interferogram. A Fourier transformation of the interferogram generates the FTIR spectrum (figure 10b). Every scan is the result of a complete back and forth movements of the moving mirror.

In this thesis a Nicolet 6700 equipment was used to get FTIR spectra in the energy range of 400cm^{-1} to 4000cm^{-1} with a resolution of 8cm^{-1} .

2.2.2 Ultraviolet-visible spectroscopy (Uv-vis)

When radiation interacts with matter, a number of processes can occur, including reflection, scattering, absorbance, fluorescence/phosphorescence (absorption and reemission), and photochemical reaction (absorbance and bond breaking).

Because light is a form of energy, absorption of light by matter causes the energy content of the molecules (or atoms) to increase. The total potential energy of a molecule generally is represented as the sum of its electronic, vibrational, and rotational energies: $E_T = E_{electr} + E_{vibrat} + E_{rotat}$.

The amount of energy a molecule possesses in each form is not a continuum but a series of discrete levels or states. The differences in energy among the different states are in the order: $E_{electr} > E_{vibrat} > E_{rotat}$.

In some molecules and atoms, photons of UV and visible light have enough energy to cause transitions between the different electronic energy levels. The wavelength of light absorbed is that having the energy required to move an electron from a lower energy level to a higher energy level. For molecules, vibrational and rotational energy levels are superimposed on the electronic energy levels. Because many transitions with different energies can occur, the bands are broadened. The broadening is even greater in solutions owing to solvent-solute interactions.

When light passes through or is reflected from a sample, the amount of light absorbed is the difference between the incident radiation (I_0) and the transmitted radiation (I). The amount of light absorbed is expressed as either transmittance or absorbance. Transmittance is usually given in terms of a fraction of 1 or as a percentage and is defined as follows:

$$\%T = \left(\frac{I}{I_0}\right) \times 100$$

Absorbance is defined as follow:

$$A = -\log T$$

Ultraviolet- visible (UV-vis) spectroscopy is a useful technique for determining optical gap of crystalline and amorphous semiconductors. An amorphous or non-crystalline solid lacks the long range order characteristic of a crystal. Because of this amorphous materials have localized sates between the valence band (VB) and conduction band (CB), the calculation of the gap is more complex.

For this work a spectrometer UV-vis Perking Elmer Lambda 35 in a range of 190-1100 nm was used to obtain absorbance and transmittance spectra of the samples.

2.2.3 Null ellipsometry

An optical method used principally for characterization of thin films and surfaces is ellipsometry. The technique is based on analysis of changes in polarization of light upon its reflection from the sample. Incident beam has an arbitrary elliptical polarization and can be, therefore, described as a

superposition of two plane-polarized waves differing, in general, in phase and amplitude. One of the waves is polarized in the plane of incidence defined by the incident and reflected beam (denoted p -plane) and the other wave in the plane perpendicular to the plane of incidence (denoted s -plane) and, thus, in a plane parallel to the reflecting surface of the sample. Reflection of the two waves from the sample is described by reflection coefficients R_p and R_s respectively. The reflection coefficients are complex numbers; their absolute values give the ratio of the amplitudes of the reflected waves to those of the incident waves; their phases give the phase shifts experienced by the waves upon their reflection. Since R_p and R_s are in general not equal, reflection results in a change of the ratio of amplitudes and mutual phase shift between the waves polarized in p - and s -plane; therefore, the polarization of the reflected beam differs from the polarization of the incident beam. The change in polarization of light upon reflection can be described by two angles Ψ and Δ , which are the output of an ellipsometric measurement and are related to the complex reflection coefficients by the next equation:

$$\rho = \frac{R_p}{R_s} = \tan(\Psi) \exp(i\Delta)$$

The ratio ρ of reflection coefficients is determined from the experimentally obtained values of Ψ and Δ and, using an appropriate model, optical parameters of the sample can be inferred from the complex value of ρ . In the simplest case, the sample is homogeneous, consisting of a material characterized by complex refractive index n_3 and surrounded by a medium of complex refractive index n_1 . Therefore, only reflection on the single interface between the sample and the medium is considered. Reflection and refraction of electromagnetic waves (polarized in p - and s plane respectively) on an interface between two media of complex refractive indices nI and nJ is described by Fresnel reflection ($rpIJ$, $rsIJ$) and transmission ($tpIJ$, $tsIJ$) coefficients [38].

In the simplest case of a single reflecting interface, the reflection coefficients R_p and R_s are equal to Fresnel coefficients $rp13$ and $rs13$. Refractive index n_3 of the sample can be, then, calculated from the measured values of Ψ and Δ provided the refractive index n_1 of the medium is known. That is usually the case; the medium is typically air, vacuum or an aqueous solution (transparent in the spectral region used in the ellipsometric experiment) and its refractive index is either known or easily determined by refractometry.

$$n_3 = n_1 \tan(\phi_1) \left[1 - \frac{4\rho \sin^2(\phi_1)}{(\rho + 1)^2} \right]^{\frac{1}{2}}$$

A typical sample investigated by ellipsometry consists of thin films deposited on a reflecting surface. In the basic case, when only a single layer covers the surface, a three-phase model is used. The sample is composed of a material with index of refraction n_3 and has a smooth surface on which a layer of thickness d_2 and index of refraction n_2 is deposited. The sample is surrounded by a medium characterized by index of refraction n_1 . The angle of incidence ϕ_1 is determined by the arrangement of the ellipsometer and the angle of refraction ϕ_2 can be calculated from Snell's law (figure 11).

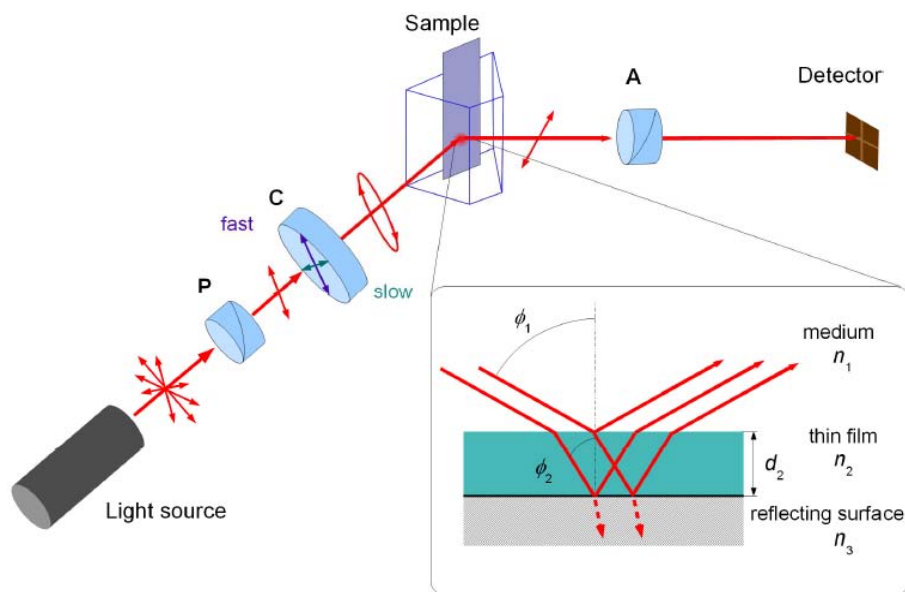


Figure (11) Three phase model of a sample consisting of a reflecting surface characterized by refractive index n_3 , a thin film of thickness d_2 and refractive index n_2 and a medium of refractive index n_1 [38].

Null ellipsometry, as its name suggests, searches for such values of adjustable parameters of the instrument, which minimize the intensity of light impinging on the detector, which would reach zero in the ideal case. The typical adjustable parameters in null ellipsometry are the azimuth angles P and A of the polarizer and the analyzer respectively and the azimuth angle C of the compensator fast axis. Adjustment of two parameters is sufficient for reaching the null intensity and one of the three azimuth angles is, therefore, usually fixed [39].

Ellipsometric measurements presented in this work were performed with a null ellipsometer Gaertner L117. A He-Ne laser ($\lambda = 632.8$ nm) was used as the incident light source. Data were analyzed through the software program AUTOST.

2.2.4 X-Ray Photoelectron Spectroscopy (XPS)

X-ray photoelectron spectroscopy (XPS) also called electron spectroscopy for chemical analysis (ESCA) falls in the category of analytical methods referred to as electron spectroscopies, so called because electrons are measured. Then, the surface to be analyzed is placed in a vacuum environment and then irradiated with photons. For ESCA, the photon source is in the X-ray energy range. The irradiated atoms emit electrons (photoelectrons) after direct transfer of energy from the photon to core-level electrons. Photoelectrons emitted from atoms near the surface can escape into the vacuum chamber and be separated according to energy and counted. The energy of the photoelectrons is related to the atomic and molecular environment from which they originated. The number of electrons emitted is related to the concentration of the emitting atom in the sample.

An understanding of the photoelectric effect and photoemission is essential to appreciate the surface analytical method, ESCA. When a photon impinges upon an atom, one of three events may occur: (1) the photon can pass through with no interaction, (2) the photon can be scattered by an atomic orbital electron leading to partial energy loss, and (3) the photon may interact with an atomic orbital electron with total transfer of the photon energy to the electron, leading to electron emission from the atom. In the first case, no interaction occurs and it is, therefore, not pertinent to this discussion. The second possibility is referred to as ‘Compton scattering’ and can be important in high-energy processes. The third process accurately describes the photoemission process that is the basis of ESCA. Total transfer of the photon energy to the electron is the essential element of photoemission (figure 12).

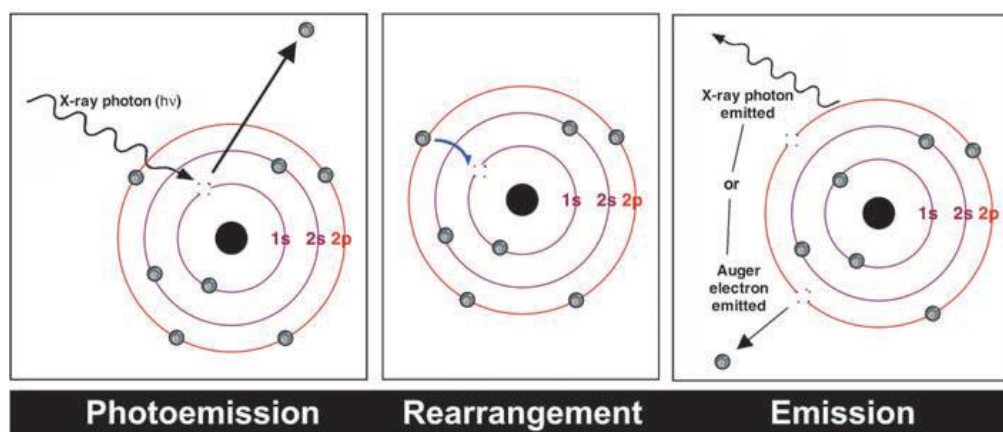


Figure (12) (a) The X-ray photon transfers its energy to a core-level electron leading to photoemission from the n -electron initial state. (b) The atom, now in an $(n - 1)$ -electron state, can reorganize by dropping an electron from a higher energy level to the vacant core hole. (c) Since the electron in (b) dropped to a lower energy state, the atom can rid itself of excess energy by ejecting an electron from a higher energy level. This ejected electron is referred to as an Auger electron. The atom can also shed energy by emitting an X-ray photon, a process called X-ray fluorescence [40]

The most basic ESCA analysis of a surface will provide qualitative and quantitative information on all the elements present (except H and He). More sophisticated application of the method yields a wealth of detailed information about the chemistry, electronic structure, organization, and morphology of a surface. Thus, ESCA can be considered one of the most powerful analytical tools available [40].

The XPS analysis of the samples in this thesis was carried out with a VG Microtech Multilab ESCA 2000 equipment. The samples were eroded with argon ions at energy of 3 kV and 1 μ A.

2.2.5 Atomic Force Microscopy (AFM)

Atomic force microscopy (AFM) uses a force-sensing probe to track sample topography by raster-scanning the probe over the sample surface, thereby producing a topographic map. The probe used is a very sharp tip mounted at the end of a cantilever, which can be fabricated with spring constants as low as ~ 0.01 nN/nm. The tip and the cantilever are usually made of Si, SiO₂ or Si₃N₄. As the interaction force between the cantilever tip and the surface varies, deflections are produced in the

cantilever. These deflections may be measured, and used to compile a topographic image of the surface. The process is illustrated schematically in Figure (13). Microscopes have been designed which can monitor interactions due to a range of forces, including electrostatic and magnetic forces. For example, the magnetic force microscope has a tip which possesses a magnetic moment and which therefore responds to the magnetic field of a magnetized sample, while the electrostatic force microscope senses surface charge; it is the electrostatic interaction between the charged tip and the sample which is measured. Scanning force microscopes (SFMs) generally measure forces in the range 10^{-9} – 10^{-6} N, although the measurement of forces as low as 3×10^{-13} N has been reported.

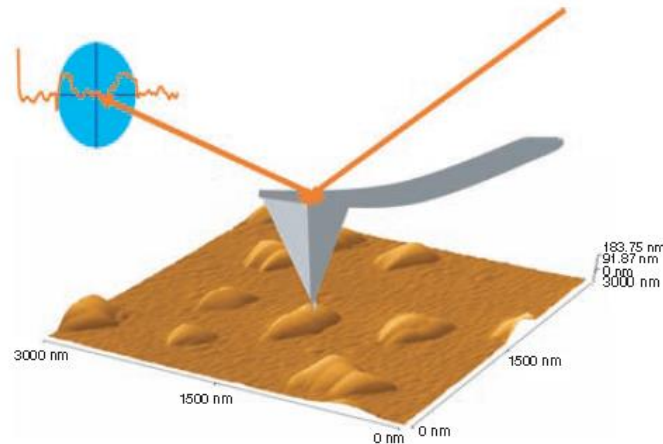


Figure (13) Schematic illustration of the operation of the AFM [40]

Clearly, because the AFM is based upon force measurement, there is no longer any need for the sample to be an electrical conductor. Effectively, it offers high resolution microscopy (with a resolution comparable to that of an electron microscope in many cases) for insulating samples under ambient and liquid conditions. This represents an enormous spread of new capability.

The measurement of forces between atoms and molecules can tell us much about their structures and the nature of their interactions. The forces between atoms may be described by the Lennard–Jones potential:

$$V(r) = 4E\left[\left(\frac{\sigma}{r}\right)^{12} - \left(\frac{\sigma}{r}\right)^6\right]$$

The energy of interaction has a minimum value E at an equilibrium separation r_0 , and the separation is σ at $V(r) = 0$. At separations greater than r_0 , the potential is dominated by long-range attractive interactions that decay as a function of $1/r^6$, while at shorter distances, the interaction becomes increasingly dominated by short-range repulsive interactions that vary with $1/r^{12}$. These are quantum-mechanical in nature and arise from the interpenetration of the electron shells of the interacting atoms at small separations [40].

AFM operation is usually described as one of three modes, according to the nature of the tip motion: contact mode, also called static mode (as opposed to the other two modes, which are called dynamic modes); tapping mode, also called intermittent contact, AC mode, or vibrating mode; non-contact mode, or after the detection mechanism, frequency modulation AFM.

In this thesis the morphological analysis of the samples was made with a JSPM-4210 scanning probe microscope in tapping mode.

2.2.6 High Resolution Transmission Electron Microscopy (HRTEM)

Transmission electron microscopy (TEM) offers both a direct image and a diffraction pattern of the specimen. High-energy electrons are used as probe and imaging of the transmitted electrons reveal information on the sample morphology and structure. Furthermore, through energy analysis of the transmitted electrons or the emitted characteristic X-rays, information on the chemical composition can be obtained. The main disadvantage of TEM is the destructive approach necessary when preparing a sample for microscopy, which may influence the microstructure of the sample to be analyzed.

A schematic diagram of a simple TEM is depicted in figure (14). At the top of the microscope column electrons are emitted from an electron gun and accelerated to an energy typically in the range 100–300 keV, corresponding to a de Broglie wavelength of $\lambda = 0.037\text{--}0.020 \text{ \AA}$, respectively. The electron beam passes through one or more condenser lenses that focus the beam onto the specimen, which is located inside the objective lens to minimize aberration effects. In order to have the electrons transmitted through the specimen, it has to be very thin to minimize energy absorption due to inelastic scattering events, i.e. specimen thicknesses are usually limited to be in the order of 100 nm. On their way through the specimen the electrons are diffracted, transmitted without diffraction or inelastically scattered. Due to the small de Broglie wavelength, the diffraction angles θ as deduced from $2d \sin \theta = \lambda$ are very small. Because of this, several diffracted rays will be almost parallel to the directly transmitted beam, causing the diffraction pattern formed in the back focal plane of the objective lens to contain more diffraction spots than typically obtained by X-ray diffraction techniques. An aperture placed in the back focal plane of the objective lens is used to select which parts of the diffraction pattern to be used to create an image of the specimen in the image plane of the objective lens. This image is magnified by the intermediate and projector lenses onto a fluorescent screen located at the bottom of the column. The final image shown on the viewing screen will be rotated with respect to the actual specimen orientation since the lenses are magnetic coils, the rotation depending on the magnification. In *Bright-Field imaging* (BF) only the central direct-transmitted beam is allowed to pass the aperture placed in the back focal plane of the objective lens. The resulting image of the specimen will contain bright regions where the electrons have not been diffracted and *vice versa* for dark regions. In *Dark-Field imaging* (DF) one or more diffracted beams are chosen by means of the objective aperture, which blocks the direct transmitted beam and the other diffracted beams. The resulting image shows bright regions from areas of the specimen giving rise to the chosen diffracted beams. DF imaging is especially useful when differentiating between two diffracting crystalline phases, both yielding similar contrast in BF mode. By selecting only the diffracted beam from one of the phases, this phase will show up as bright areas in the image whereby a phase map can be obtained. Grains with different compositions,

structures and crystallographic orientations diffract differently, exhibiting contrast in both BF and DF imaging mode [35].

In *diffraction mode*, the diffraction pattern formed in the back focal plane of the objective lens is projected onto the viewing screen. Since the diffraction pattern depends on the lattice parameters of the crystalline phases and the crystallographic orientation of the diffracting domains, this mode is very useful in phase identification and in exhibiting textural information [35].

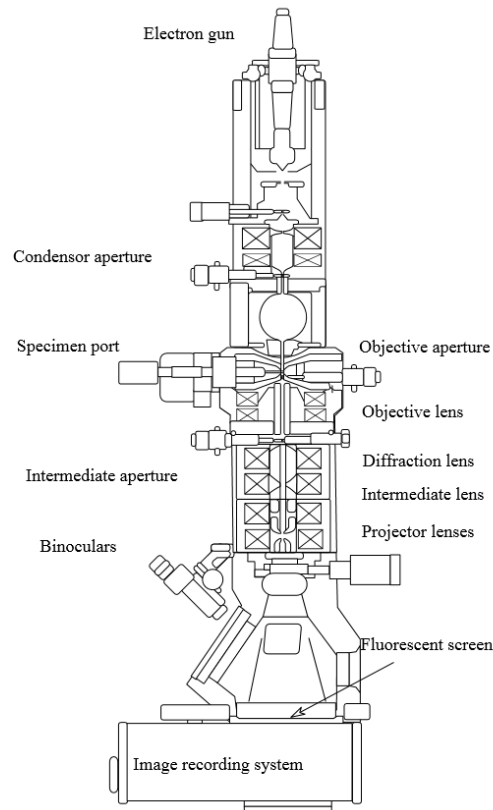


Figure (14) Layer scheme of a simple Transmission Electron Microscopy (TEM)

Depending on the information desired, the specimen for TEM can either be prepared as a plan-view or as a cross-section specimen. In plan-view TEM, the scattering vector lies approximately in the plane of the thin film thus yielding in-plane microstructural information. In cross-section TEM, the scattering vector is located in the plane of the cross section revealing microstructural information both in-plane and out-of-plane with respect to the film surface. This method is especially powerful when investigating for example the microstructure of multilayered samples.

The shape, size and distribution of the smallest gold particles studied in this thesis were observed by high resolution electron microscopy (HRTEM) and high angle annular dark field (HAADF) using a field emission gun (JEM-2010F) which operates at 200 kV, with a theoretical point to point resolution of 0.19 nm. The HRTEM images in planar view of the samples were recorded with a CCD camera and treated with a digital analysis program.

2.2.7 Scanning electron microscopy

A scanning electron microscope (SEM) uses electrons rather than light to generate images and the resolution of an SEM is therefore limited by the wavelength of electrons, which at the standard energy of 5keV is on the order of a few nanometers. Electrons from a thermionic cathode) or a field-emission are accelerated by a voltage of 1-50 kV between cathode and anode. The beam cross-section with a diameter of 10-50 μm for thermionic and 10-100 nm for field-emission guns is then demagnified by a two- or three-stage electron lens system so that an electron probe of about 1-10 nm carrying an electron probe current between 1-100 pA is formed at the specimen surface. A detection coil system in front of the last lens scans the electron beam in a raster fashion. The main parts of a simple SEM are electron gun, condenser lenses, apertures, scanning system and specimen chamber.

Signal detection begins when a beam electron, known as the primary electron enters a specimen. When the primary electron enters a specimen it will probably travel some a distance into the specimen before hitting another particle. After hitting an electron or a nucleus, etc., the primary electron will continue on in a new trajectory. This is known as scattering. It is the scattering events that are most interesting, because it is the components of the scattering events (not all events involve electrons) that can be detected. The result of the primary beam hitting the specimen is the formation of a teardrop shaped reaction vessel. The reaction vessel by definition is where all the scattering events are taking place. Small reaction vessels tend to give better resolution, while large reaction vessels tend to give more signal. The volume of a reaction vessel depends upon the atomic density, topography of the specimen and the acceleration potential of the primary electron beam. For example low density material and higher voltages will result in larger reaction vessels since the electron beam can penetrate deeper into the sample. Topography will also change the amount of emissions from a reaction vessel. An increase in the topography will increase the surface area of the reaction vessel resulting in more signal. Some of the more important events occurring in the reaction vessel include (figure (15)):

Backscattered electrons: A primary beam electron may be scattered in such a way that it escapes back from the specimen but does not go through the specimen. Backscattered electrons are the original beam electrons and thus, have a high energy level, near that of the gun voltage. Operating in the backscattered imaging mode is useful when relative atomic density information in conjunction with topographical information is to be displayed.

Secondary electrons: Perhaps the most commonly used reaction event is the secondary electron. Secondary electrons are generated when a primary electron dislodges a specimen electron from the specimen surface. Secondary electrons can also be generated by other secondary electrons. Secondary electrons have a low energy level of only a few electron volts, thus, they can only be detected when they are dislodged near the surface of the reaction vessel. Therefore, secondary electrons cannot escape from deep within the reaction vessel. Secondary electrons that are generated but do not escape from the sample are absorbed by the sample. Two of the foremost reasons for operating in the secondary electron imaging mode are to obtain topographical information and high resolution. An excellent feature about imaging in the secondary mode is that the contrast and soft shadows of the image closely resemble that of a specimen illuminated with light. Thus, image interpretation is easier because the images appear more familiar.

Atomic density information also can also be obtained because some materials are better secondary emitters than others. The use of secondary electrons to determine atomic number is not as reliable as with the backscatter mode.

X-rays: When electrons are dislodged from specific orbits of an atom in the specimen, X-rays are emitted. Elemental information can be obtained in the X-ray mode, because the X-ray generated has a wavelength and energy characteristic of the elemental atom from which it originated. Problems arise when the X-rays hit other particles, they lose energy, this changes the wavelength. As the number of hits increases, the x-rays will not have the appropriate energy to be classified as coming from the originating element and detection of these X-rays will be known as background. X-ray spectrometer detectors measure wavelength (wavelength Dispersive Spectrometer or WDS) or energy level (Energy Dispersive Spectrometer or EDS).

Transmitted electrons: If the specimen is thin enough, primary electrons may pass through the specimen. These electrons are known as transmitted electrons and they provide some atomic density information. The atomic density information is displayed as a shadow. The higher the atomic number the darker the shadow until no electrons pass through the specimen [41].

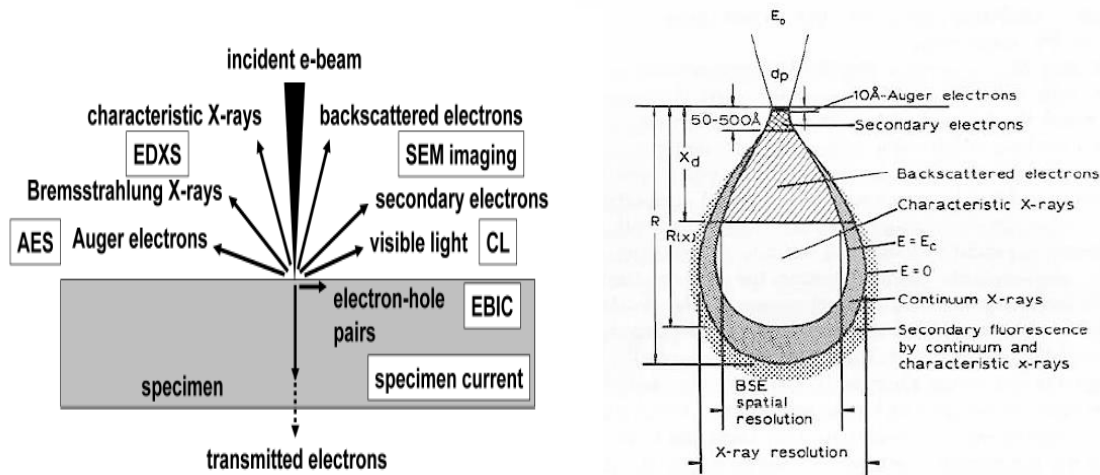


Figure (15) Schematic diagram of the analytical modes of a SEM

A Field Emission-Scanning Electron Microscope (JEOL7600F FE-SEM) was used to observe shape and distribution of the gold films of different thicknesses. Additionally, cross section of the fabricated devices also was observed.

2.2.8 Photoluminescence measurements

Photoluminescence of the samples was acquired using a spectrofluorometer (Fluoromax-Spex) sensitive in the range 200–850 nm and a quartz optical fiber. A laser beam of He-Cd at 325 nm with power of 10 mW was impinged 45° on the film while the optical fiber remained perpendicular to the sample for recording the signal toward the spectrofluorometer. The schematic diagram of the system used to obtain photoluminescence spectra is depicted in figure (16).

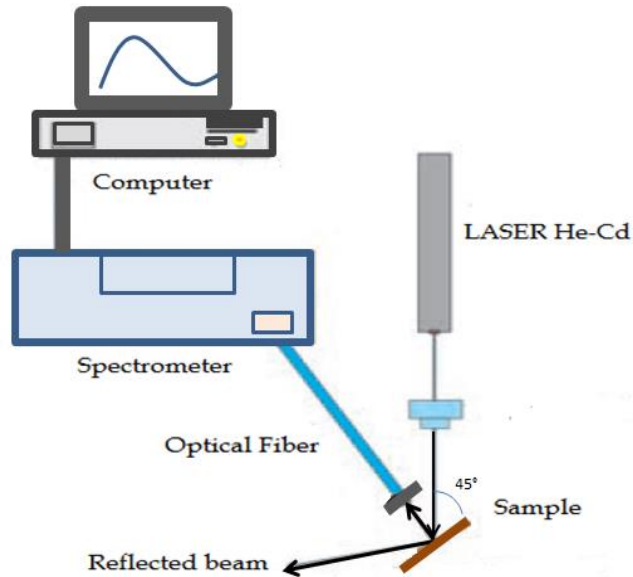


Figure (16) Schematic diagram of the system used to obtain photoluminescence spectra.

2.2.9 Electroluminescence measurements

Electrical characterization of the luminescent samples was carried out using a voltage source PL-Lab 1 connected in serie with a multimeter Keithley 2000. A quartz optical fiber terminal was placed 2 mm from the light emission side of the sample. The other terminal of the fiber was directed to a Spex-Fluoromax spectrometer sensitive in the range 200–850 nm. Schematic diagram to measure electroluminescence emission of the devices is depicted in figure (17).

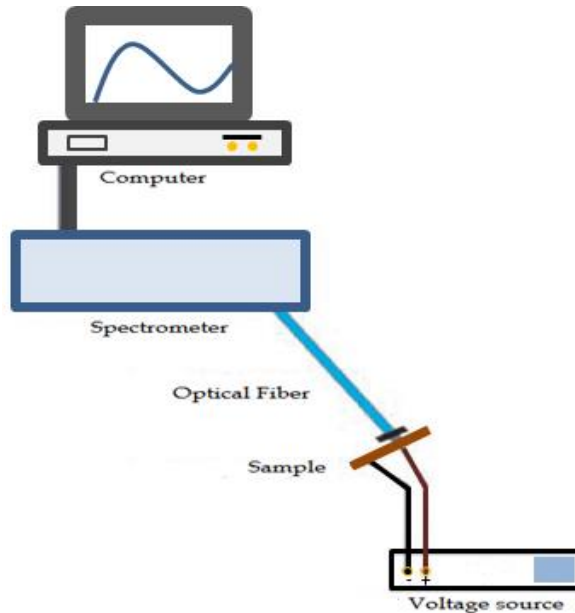


Figure (17) Measurement set up for light emission devices.

CHAPTER III. Photoluminescence of the silicon quantum dots active film

The absorption in a solid can be due primarily to the action of the following mechanism: 1) transition of electrons from the valence band to the conduction band, 2) transitions by means of excitonic states, 3) transitions of electrons or holes within the respective permitted bands, i.e., the transitions related to free charge carriers, 4) transitions through impurity states, 5) absorption for vibrations of the crystalline lattice or phonons, among others. It is just some of these mechanisms can produce radiative events; therefore, here lies the importance for understanding which of them could be responsible for the emission in SiQDs films.

In this section of the thesis are explained some of the main models used to account for the observed luminescence in silicon nanocrystals films; these include quantum confinement of excitons, surface passivation and defects states. In addition, the physical and chemical properties of the active films of SiQDs used in thesis under different thermal treatments were also studied in this chapter.

3.1 Quantum confined model

As mentioned previously, the interest in nanostructures of Si stems from the effects of confinement on carrier wave functions when the crystallite diameter is less than the size of the free exciton Bohr radius of 4.3 nm in bulk c-Si. In a semiconductor the most immediate consequence of the confinement effect is an increase in the band gap energy and an associated increased probability of radiative transfer. As the carrier are confined in real space, their associate wavefunctions spread out in momentum space. This increases the probability of radiative transitions as the electron-hole wave function overlap is greater [20]. In this model the statistical distribution of dark and bright dots determines the overall luminescence efficiency. Moreover, the fact that the Si dots are usually formed in a dielectric matrix having a lower refractive index than that of c-Si increases the extraction efficiency of the light generated in the active material itself.

The mechanism of quantum mechanical confinement is understood qualitatively by considering the particle in a box problem, which can be solve for the wave functions (eigenstates) and energies (eigenvalues) of an infinite potential well using Schrödinger's wave equation (figure 18). In order to satisfy boundary conditions the characteristic ground state energy scales inversely with the square of the width of the confining potential well [4].

According to P. F. Trwoga et al [42] there are three different categories of confinement considering the relative sizes of the Bohr radius and the potential well: strong, medium, and weak. The weak confinement regime is that in which R (potential well size) is greater than the bulk exciton Bohr radius $a_B = a_e + a_h$ (a_e and a_h are the electron and the hole Bohr radio). Moderate confinement regimes exist where the excitonic Bohr radius and the size of the cluster are roughly equal and, $a_h < R < a_e$. the strong confinement regime is that in which $R < a_B$ and $R < a_h, a_e$. For silicon clusters the values for the Bohr radius for each particle are $a_e = 3.19E-9$, $a_h = 2.11E-9$, and $a_B = 5.3E-9$ m.

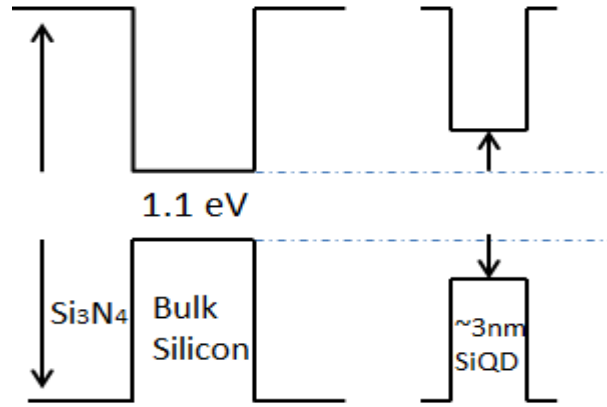


Figure (18) The effective bandgap of a silicon nanocrystal with a diameter that is smaller than the exciton Bohr radius (~ 5 nm) increases by the quantum confinement effect (in this picture the silicon quantum dot (SiQD) is surrounded by Si_3N_4 matrix).

In 1982 Efros et al. proposed a theoretical model for explaining quantum confined effect in spherical microcrystallites with infinite potential barriers at the crystallite boundary. This model was based on the effective mass approximation (EMA) with parabolic energy bands. Other models have been developed with various refinements since the original analysis of Efros et al., including those using experimentally obtained fitting parameters [42].

Brus and Kayanuma extended the Efros et al. model to include Coulomb and correlation energy terms which enables derivation of an expression that models energies and provides a reasonable guide to cluster size as a function of E_g :

$$E(R) = E_g + \frac{h^2\pi^2}{2R^2} \left(\frac{1}{m_e^*} + \frac{1}{m_h^*} \right) - \frac{1.786e^2}{\epsilon_r R} + 0.284E_R$$

where E_R is the Rydberg energy for the bulk semiconductor:

$$E_R = \left(\frac{13.606m_0}{\epsilon_r^2 \left(\frac{1}{m_e^*} + \frac{1}{m_h^*} \right)} \right) eV$$

The Coulomb term is $1.786e^2/\epsilon_r R$, and $0.284E_R$ gives the spatial correlation energy and is a minor correlation [42].

3.2 Surface passivation

Nanoparticles exhibit enormous surface area-to-volume ratios; according to one estimate, a 2 nm diameter icosahedral silicon particle possesses approximately 280 Si atoms with 120 (43%) residing at the surface of the particle. Then, tailoring the surface of such particles offers the attractive possibility of controlling their interactions with their surroundings.

The superficial reconstruction of a silicon nanodot is related to a process where dangling bonds on its surface are attached to a convenient atom or molecule. This process gives rise to an important distortion in atoms of superficial bonds than those atoms at the center of the nanodot. Then, states related to this change are introduced into the optical gap of the nanodot [43].

The surface modification has employed the more robust polar covalent bonding of silicon–carbon, silicon–nitrogen and silicon–oxygen linkages for example; although still, questions and challenges regarding the effectiveness of Si-nc surface passivation and the associated particle stability remain (figure 19). The bond strengths of various species present at particle surfaces are shown in table 1.

Bond	Bond energy (kJ mol ⁻¹)
Si-H	323
Si-N	469
Si-C	369
Si-Cl	391
Si-O	368
Si-Si (bulk)	210-250
Si-Si (disilane)	310-340
Si-Si (disilene)	105-126

Table 1. Selected bond energies of Si-X bonds.

Some of the methods for controlling silicon nanocrystals surfaces are in situ surface chemistry tailoring related. Holmes et al. prepared sterically stabilized Si-ncs by thermally decomposing diphenyl silane in supercritical octanol. The resulting particles ranged in diameter from 1.5 to 4.0 nm, and the FTIR analysis confirmed that a surface organic layer was indeed bonded through an alkoxide linkage (Si-O-C). These alcohol-soluble nanoparticles were highly photoluminescent. Moreover, SiQDs are readily prepared in nonthermal plasmas and further modified in situ to yield organic surface-stabilized materials. Liao et al. were the first to apply gas-phase reactions of this type to the surface modification of SiQDs [25]. Particles were prepared from silane in a nonthermal reactor and extracted into a reactor chamber containing organic reagents of choice (e.g., amines, alkenes, and alkynes). Heating of the gas-phase mixture led to surface modification that was spectroscopically confirmed.

Additionally, SiQDs surfaces bearing halogens may be directly obtained from the synthetic reaction, as is the case when particles are prepared from Zintl salt precursors, or it may be realized after postsynthetic modification upon reaction of Si-H-terminated particles with Cl₂. The Si-Cl

reactive surface opens the surface to modification using a wide variety of solution reagents. Clearly, the Si-Cl surface offers significant chemical breadth as evident by its electrophilic reactivity and the demonstration that it may be readily converted to Si-H and Si-Br with exposure to lithium aluminum hydride and bromine, respectively. In the light of the vast chemistry of Si-Cl bonds, this mode of surface modification holds significant untapped potential in controlling SiQDs chemistry.

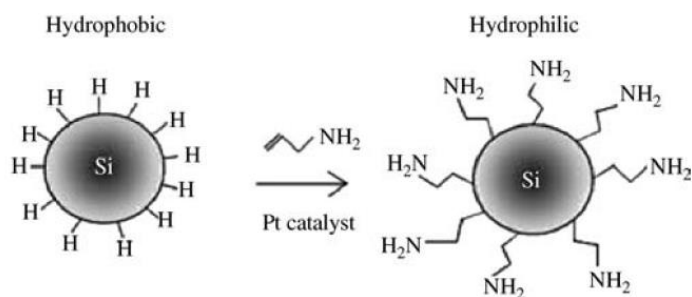


Figure (19) Surface termination of SiQDs to yield amine surface functionality [25].

By using halogen precursors Si-nc deposited by PECVD can be embedded in chlorinated silicon nitride thin films. These films have shown to have efficient photoluminescence in the red (1.8 eV) to blue-violet (3.1 eV) region and this even improves with thermal annealing. Although in this case the Si-nc can be passivated with H, N, or Cl atoms, it has been previously speculated that their good photoluminescent properties are due to the passivation with N and/or Cl [44, 45]. Most of the theoretical studies used to explain the experimental results on the photoluminescent properties of silicon nanoclusters embedded in thin films or in porous silicon are based on the calculation of the electronic structure and optical properties of silicon nanoclusters in vacuum and with atomic hydrogen as the main surface passivant. These theoretical works have shown that when the surface of Si-nc is completely passivated with hydrogen, the HOMO (Highest Occupied Molecular Orbital)-LUMO (Lowest Unoccupied Molecular Orbital) gap increases in conformity with the quantum confinement effect, and consequently, their photoluminescence can be tuned from near infrared to ultraviolet by decreasing the size of the nanoclusters.

Some calculations made for small (~ 1 nm), fully hydrogenated SiQDs, such as $\text{Si}_{35}\text{H}_{36}$, have indicated that the HOMO-LUMO gap decreases significantly when the H atoms of the SiQDs surface are partially replaced with double bonded O to form $\text{Si}_{35}\text{H}_{34}\text{O}_{20-22}$ or totally replaced with OH groups to form $\text{Si}_{35}(\text{OH})_{36}$. These results were used to explain why hydrogen-passivated SiQDs luminesce in the blue, whereas oxide-passivated SiQDs luminesce in the red. Some of these studies have also found that single-bonded surface passivators such as Cl, F, or OH produce a small variation, of 0.1 to 0.2 eV, in the HOMO-LUMO band gap of these small SiQDs [46].

3.3 Defect related luminescence

Si nanocrystals completely embedded in amorphous SiO₂ is desired to realize a high potential barrier and hence good confinement. Incomplete crystallization causes a remaining amorphous shell, and the reduced potential barrier leads to problems with the quantum confinement. Such a remaining shell will have imperfections in the atomic bonds resulting in defects and disordered or broken bonds. The remaining incomplete SiO_x shell has been proven by using photon-in photon-out soft X-ray spectroscopy, the electronic structure of silicon nanoclusters embedded in an electrically insulating SiO₂ host matrix was investigated as a function of nanocluster size. It was found the nanoclusters to be of a core-shell structure with a crystalline Si core and an ultrathin transition layer of a suboxide.

Electron spin resonance (ESR) is a technique sensing the whole volume of a sample with the ability to distinguish between different materials by using paramagnetic defects as a probe. ESR can identify these paramagnetic defects and infer their location within the sample structure. Various ESR studies have been performed on nano-Si entities in SiO₂ and generally five types of point defects are observed, that is, D (Si dangling bonds (DB) in disordered Si), P_{b(0)}, P_{b1}, E'γ, and EX. All works report a generally featureless isotropic line commonly referred to as the Si DB signal with zero crossing g value (g_c) in the range of 2.005–2.006. A first series of ESR measurements investigated Si nanoparticles embedded in SiO₂ and phosphosilicate glass fabricated by Si⁺ ion implantation. A rather broad signal was observed at g_c~2.006 with a peak to peak width of DB_{pp}=7.0–7.9 G, which was suggested to originate from P_b centers. The P_b centers are prototype interface defects that are characteristic of the Si/SiO₂ interface. Figure (20a–c) shows the DB, P_{b(0)}, and P_{b1} defects. The presence of P_b-type defects would be important, as these are deep nonradiative recombination centers, known to quench the PL from Si nanocrystals in the 1.4–2.2 eV range, irrespective of whether the source of the PL is quantum confinement or interface states. Thus, the analysis of whether such defects are observed in ESR for Si nanocrystals embedded in SiO₂ is quite an important question. To make sure that the signal really is related to the interface of the nanocrystals and not to the interface of the substrate, it is necessary to take into account the angle dependence of the signal. The absence of any angle dependence in the P_b ESR signal indicates that the defects stem from the interface between Si nanocrystals and surrounding SiO₂ and not from the Si substrate [25].

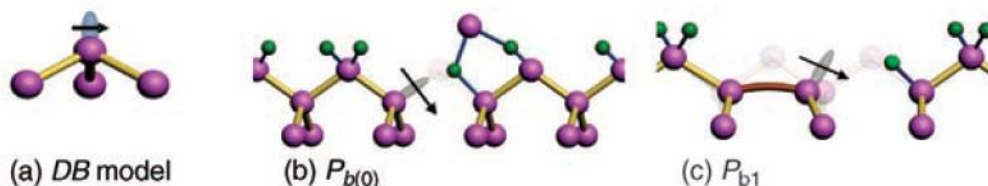


Figure (20) (a) DB model, (b) P_{b(0)} and (c) P_{b1} [25]

The presence of EX centers, has been related to the quality of the SiO₂ matrix, which may be linked to the kind of deposition or phase separation annealing procedures applied. The E'γ center was

identified as an unpaired electron at a threefold coordinated Si (generic entity $O_3\equiv Si^\cdot$). It may be taken as a measure for the presence of oxygen vacancies, or at least, oxygen deficiencies of the SiO_2 matrix, establishing a quality label in that sense. The upper limit of the activation for the E'_γ centers is reached after VUV irradiation, that is, related to substantial increase in $h\nu$, not the exposure time.

J. Robertson et al. [47] studied the local electronic structure of the principal defects in silicon nitride deposited by chemical vapor deposition (CVD) and plasma deposition (PD) calculated by the tight-binding recursion method. They constructed a gap state energy distribution for CVD and PD nitrides based in the calculated energy levels of the principal defects, namely, the Si and N dangling bonds ($\equiv Si$ and $\equiv N$), $\equiv SiH$, $\equiv NH$, and the $\equiv Si-Si\equiv$ unit. According to them, the $\equiv Si$ centers produce a density of states peak near midgap. As $\equiv Si$ centers outnumber $\equiv N$ centers, the latter are doubly occupied and negatively charged and the Fermi level lies within the $\equiv Si$ states. The Si-Si centers and $\equiv N^\cdot$ centers generate a valence band tail of about 1.5 eV. The schemes of these gap state spectra are depicted in figure (21).

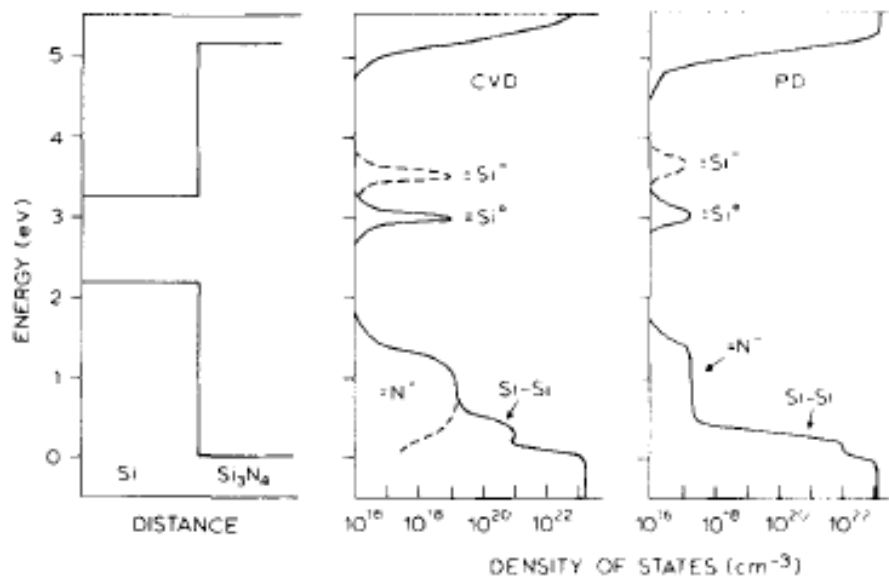


Figure (21) Density of gap states for a CVD and PV silicon nitride [47].

3.4 SiQDs embedded in a chlorinated silicon nitride matrix (SiN_x:Cl)

The silicon nanocrystal research group has been largely convinced by experimental and theoretical evidence about oxygen bond trap states that blue emission from quantum confined excitons is unlikely to be accomplished from nanocrystals embedded in silicon oxide environments. For this reason, the attention has been shifted more recently to silicon nanocrystals into silicon nitride materials.

Stoichiometric silicon nitride (Si₃N₄) has a density of 3.1 g/cm³, optical gap of 5 eV and refractive index of 2.05 at 632.8 nm. From an electric point of view this is an insulating material with resistivity of 10¹⁴ Ωcm. In the bond structure of Si₃N₄ each silicon atom is located in the center of a tetrahedron connected to four nitrogen atoms, and at the same time each nitrogen atom is found in the center of an equilateral triangle connected to three atoms of silicon.

Silane gas (SiH₄) is commonly the source of silicon used to produce silicon nitride and silicon nanocrystals films. However, there is not good stability of the physical and chemical properties of the samples because of the incorporated hydrogen in the matrix. In order to overcome these problems some halogenated gas sources have been studied such as SiCl and SiH₂Cl₂. Chlorine atoms play a role in the promotion of the chemical reactivities of SiCl and SiHCl complexes with the aid of atomic hydrogen from diluted H₂. The disorder-induced stress and the enhanced chemical reactivity of SiCl and SiH₂Cl₂ complexes created by the impinging atomic hydrogen are in combination some possible causes of the preferential phase transition from amorphous state to nanocrystalline silicon, i.e nucleation at low temperature [48, 49].

3.5 Deposition of SiQDs thin films and thermal treatments

At the present time, different processes in the production of microelectronics devices require to use high temperatures. Consequently, it is necessary to know the physical and chemical properties of the active films under different thermal treatments after being deposited. In this chapter it is presented the study of SiQDs films deposited by RPECVD undergoing different post-deposition thermal treatments in N₂ ambient with the aim of understanding the above mentioned properties. The parameters used for deposition of the SiQDs films embedded in a silicon nitride matrix were:

<i>NH₃</i> <i>Flow</i> <i>rate</i> <i>(sccm)</i>	<i>SiH₂Cl₂</i> <i>Flow rate</i> <i>(sccm)</i>	<i>H₂ Flow</i> <i>rate</i> <i>(sccm)</i>	<i>Ar Flow</i> <i>rate</i> <i>(sccm)</i>	<i>Substrate</i> <i>temperature</i> <i>(°C)</i>	<i>Plasma</i> <i>power</i> <i>(Watts)</i>	<i>Chamber</i> <i>pressure</i> <i>(mTorr)</i>
200	5	20	75	300	150	300

By using these flow rates it was achieved a well distribution of particles throughout the film. From previous works handling these parameters, it was found that the density of particles per unit area was 6.04E12 particles/cm², and their average size 3.1 nm [23].

3.5.1 Fabrication process steps

The SiQDs films were deposited on type n crystalline silicon of low resistivity (0.1-2 Ωcm) and quartz. A thickness of $\sim 2000\text{\AA}$ was determined by F. Reizman's color table [50] for these set of samples during deposition. The surface preparation of the substrates prior to the deposition of the active films was:

1. Dive in trichloroethylene (TCE) for 10 min using ultrasonic bath.
2. Dive in acetone for 10 min using ultrasonic bath.
3. Dive in P solution for 5 min to etch native oxide.
4. Rinse in DI water and blow in high purity nitrogen.

The quartz samples were cleaned using steps one and two.

As soon as SiQDs were deposited on silicon and quartz substrates, different thermal treatments were carried out under 400°C, 500°C, 600°C, 800°C and 1000°C in a conventional furnace in N₂ (99.999% purity) atmosphere for one hour each.

3.5.2 Chemical and optical characterization

Fourier Transform Infrared Spectroscopy (FTIR) spectra of the thermally treated films are depicted in figure (22). Attached numbers to the as-grown sample correspond to the band positions and their chemical bonds are defined in table (2). It can be observed that the band due to Si-N asymmetric stretching bond (840cm^{-1}) is more intense and broader as the cured temperatures are higher than 400°C. The latter is probably due to progressive oxidation of the samples when treatment temperatures were raised and therefore, a major number of Si-O-Si stretching vibration bonds (1072cm^{-1}).

On the other hand, the intensity of the N-H ($1180, 3350\text{cm}^{-1}$) and Si-H (2180cm^{-1}) bonds decreased for temperatures greater than 500°C, due to the exo diffusion of hydrogen from N-H and Si-H broken bonds [51, 52]. The exo diffusion process could also explain the increase of the Si-N asymmetric stretching bands at these annealing temperatures as broken bonds of Si and N were able to join together. Moreover, B. S. Sahu et al. [52] explain breaking of Si-H and N-H bonds favors enrichment of N₂ atoms in the silicon nitride phase approximating it to stoichiometry.

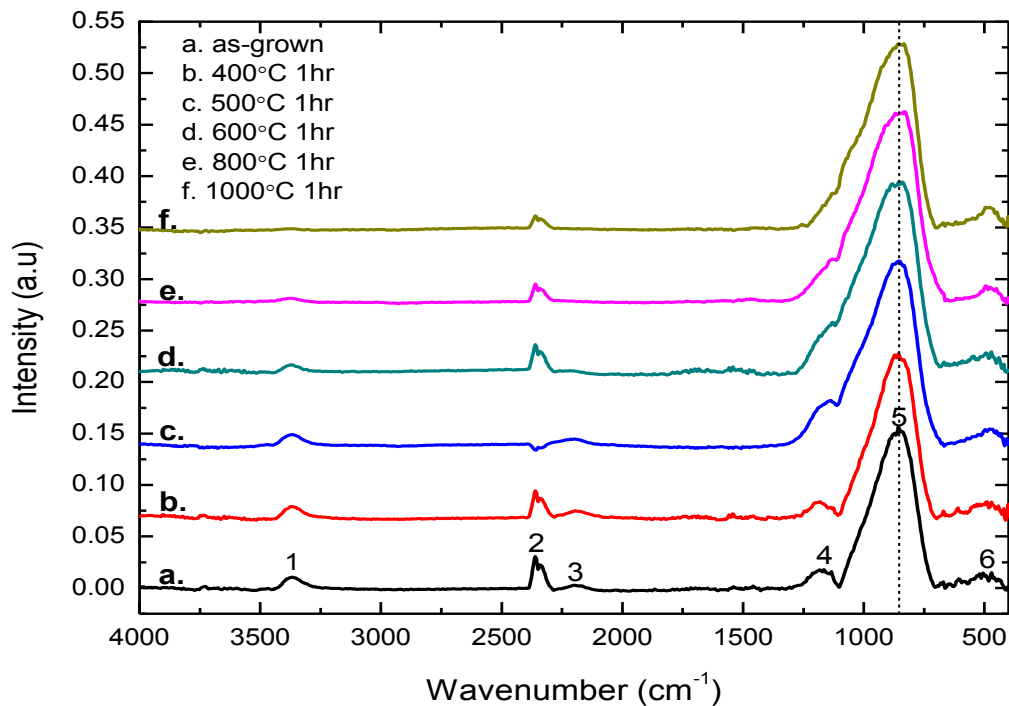


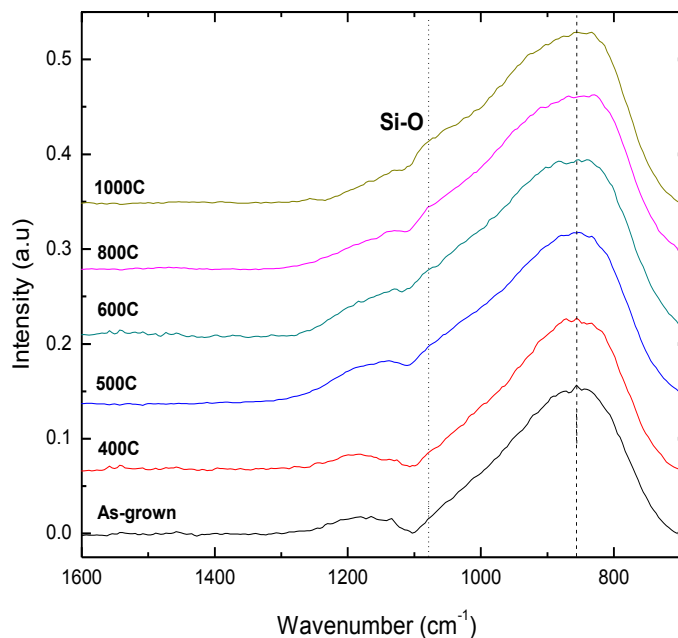
Figure (22) FTIR of the SiQDs films annealed in N₂ atmosphere.

Peak	1	2	3	4	5	6
Wavenumber (cm ⁻¹)	3350	2346	2180	1180	840	470
Functional group	N-H Stretching	CO ₂ Dioxide carbide	Si-H Stretching	N-H Bending	Si-N Asymmetric stretching	Si-N Symmetric stretching

Table (2) Chemical bonds related to the observed absorption peaks.

Figure (23) is a close view of the asymmetric stretching Si-N band of the as-grown and all the cured samples. From this figure it can be observed the N-H bending bond (1180 cm⁻¹) clearly reduced from 600°C and above, at the same time Si-O stretching bonds widened the Si-N band. A little elbow belonging to the SiO₂ functional group is seen at 1000°C (~1070 cm⁻¹).

Figure (23) Close view of FTIR spectra in the range of 500 to 1600 cm^{-1} . A little elbow at $\sim 1070 \text{ cm}^{-1}$ is better observed at 1000°C cured temperature.



The superficial chemical composition was analyzed by X Ray Photoelectron Spectroscopy (XPS). The atomic percent of the main elements found in the films is described in table (3). The percentage of the as-grown sample can be considered as the reference value. The percentage of nitrogen and chlorine diminished more consistently from 500°C. At this temperature the loss of nitrogen and chlorine atomic percentage could be related to broken N-H and H-Cl bonds expelled outside the main chamber. The silicon content decreased from 400°C when dehydrogenation generally starts due to broken Si-H bonds. The higher content of silicon percent in sample cured at 1000°C with regard to sample annealed at 800°C could be due to the rate of chemical reactions taking place at higher temperature, which could promote fast bonding of the Si dangling bonds. Since chlorine bonds are stronger, the atomic percent of this element diminished slowly up to 800°C.

Curing temperatures (°C)	%Si	%N	%Cl	%O	N/Si ratio
As-grown	47.8	39.4	4.6	8.2	0.82
400	46.7	40.5	4.6	8.2	0.87
500	46.7	37.9	4.3	11.2	0.81
600	46	35.7	3.8	14.4	0.77
800	43.2	34.9	1.7	20.2	0.8
1000	44.1	29.1	1	25.7	0.65

Table (3) Percentage of the surface chemical composition of each annealed sample.

With regard to the important change of the silicon atomic content at 800°C and 1000°C, L. Jiang et al. [51] proposed that when annealing temperature increases, and Si-H and N-H bonds decrease in

the films more silicon dangling bonds are formed acting as nucleation sites. Additionally, oxygen is the only element constantly growing from 500°C to 1000°C, which is consistent with the results obtained by FTIR showing progressive oxidation of the silicon nitride matrix. However, it is important to observe that samples suffered some grade of oxidation when they were exposed to atmosphere out of the chamber because the as-grown sample showed the same oxygen content that sample cured at 400°C. These types of bonds (Si-O, N-O) were not clearly observed in as-grown samples by FTIR spectra due to the prevailing Si-N (840cm^{-1}) band. Moreover, the most important change observed in the chlorine and oxygen concentrations was at 800°C.

PL intensity spectra of the cured samples are shown in figure (24). PL peak intensity of the sample annealed at 400°C increased 19% compared with that of as-grown sample. On the other hand, at 500°C the PL intensity is reduced without peak shift. The latter could be related to the diminished XPS atomic content obtained for nitrogen and silicon, which is probably due to the first Si-H and N-H broken bonds. Since 600°C to 1000°C the PL intensity peak decreased and also a blue-shifted was observed. Santana et al. [53] observed a similar behavior using the same precursors when the oxygen content in the surrounding host of nanocrystals increased. This fact is consistent with the increment of oxygen shown by FTIR spectra and XPS percentages at these temperatures. According to L. Jiang et al. [51] SiQDs could grow up during annealing, however, this growth is limited by low silicon diffusion at low temperatures. Thus, the silicon diffusion can be also related to the decreased Si percent observed by XPS at cured temperatures of 800°C and 1000°C as more silicon dangling bonds are formed which can act as nucleation sites or being bonded to oxygen atoms.

Therefore, the decrease of PL intensity at 500°C should be related to the rupture of the hydrogen-content bonds in the films. This process let not well passivated bonds and some of these are viable as non-radiative recombination centers [54]. Moreover, at higher temperatures oxidation of the matrix has an essential role in the formation of defects, which as was mentioned at the beginning of this chapter are known to quench the PL from Si nanocrystals.

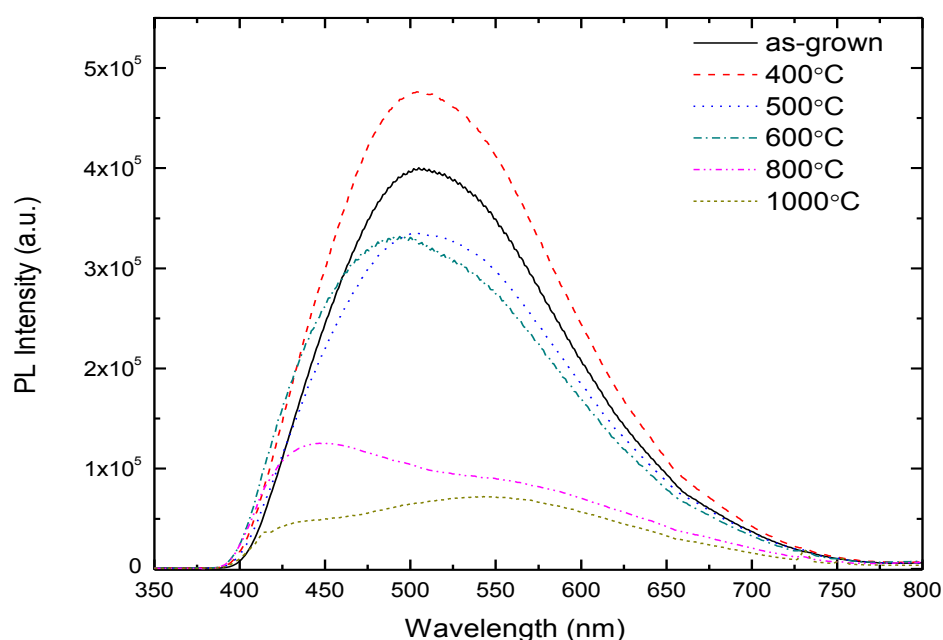


Figure (24) Photoluminescence spectra of the cured samples at as-grown, 400°C, 500°C, 600°C, 800°C and 1000°C.

The Tauc plots of as-grown sample and those cured at 400°C, 600°C, 800°C and 1000°C are depicted in figure (25). The optical band gap of these films was obtained from the absorbance data as a function of photon energy, according to the Tauc's model for amorphous semiconductors:

$$(\alpha h\nu)^{1/2} = B(h\nu - E_g)$$

where α is the absorption coefficient, B is a constant, $h\nu$ is the photon energy and E_g is the optical band gap [55]. All the samples showed two small absorption bands with peaks at 2 and 3.2 eV. Additionally, two absorption edges named E_{edge1} and E_{edge2} were observed in each sample and whose energy was obtained through a linear fitting (table 4). According to the Tauc analysis of as-grown SiQDs films by A. Rodríguez et al. [23], the E_{edge1} can be associated to absorption of photons which produce transitions of electrons from the valence band energy tail to the conduction band energy tail of the SiNx:Cl matrix due to localized states. Furthermore the energy E_{edge2} is related to the band gap energy of the silicon nitride (SiNx:Cl) matrix (E_g of stoichiometric silicon nitride is $\sim 5\text{eV}$). It can be seen from table (4) that energies of the absorption edge values E_{edge1} and E_{edge2} increased their first decimal number up to 800°C. This change can be associated to the structural modification of the matrix when oxygen atoms are incorporated into it due to desorption of hydrogen, or by the formation of new Si-N bonds at these temperatures which give rise to more dense films.

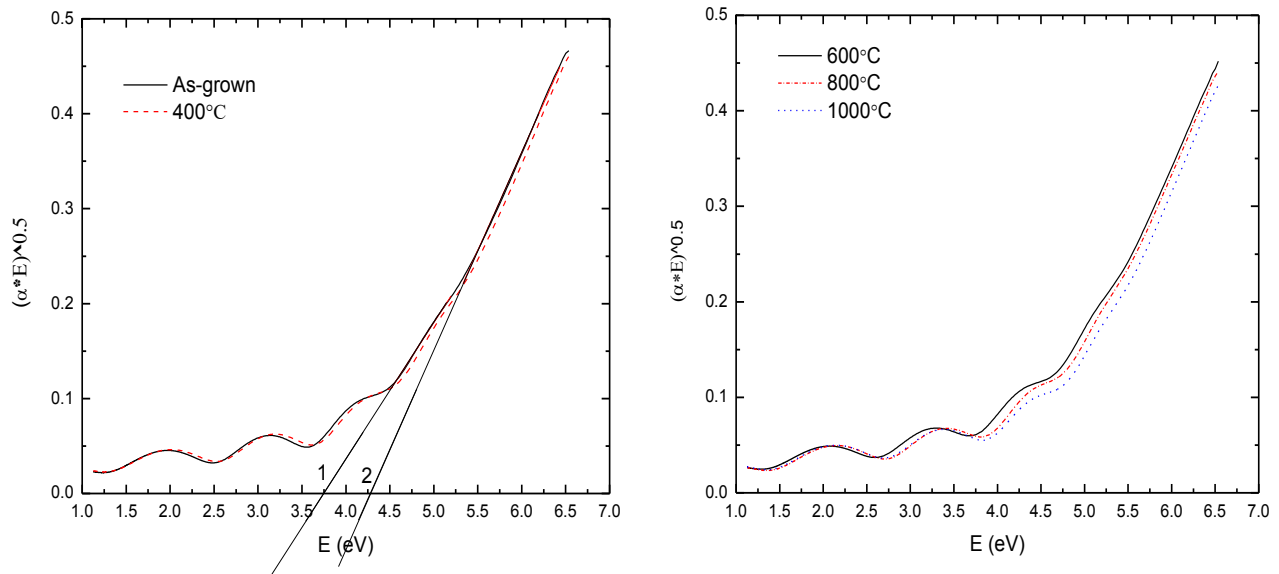


Figure (25) Tauc plots of the samples as-grown, and cured at 400°C, 600°C, 800°C and 1000°C. The energies E_{edge1} and E_{edge2} were obtained extrapolating the fitted straight lines 1 and 2.

Thermal treatment	PL peak position (nm)	PL energy (eV)	E_{edge1} (eV)	E_{edge2} (eV)
As-grown	505	2.45	3.4	4.04
400°C	504	2.46	3.44	4.08
600°C	494	2.51	3.48	4.08
800°C	449	2.76	3.6	4.15
1000°C	550	2.25	3.66	4.25

Table (4) Energy values found from Tauc plots of the as-grown and cured samples.

3.6 Conclusions

On the basis of the research work performed it can be concluded that:

It was observed increased photoluminescence of the sample cured at 400°C may be due to a rearrangement of the hydrogen atoms which could passivate radiative sites like dangling bonds or interfacial states which generally exist in non-stoichiometric silicon nitride layers obtained by CVD process. However, when the temperature increased to 500°C and above the energy was enough to break Si-H (2180cm^{-1}) and N-H (1180cm^{-1}) bonds as could be observed in FTIR spectra. The shift of the luminescent peak from 600°C to 1000°C may suggest a structural change of bonds in the host matrix of silicon nanocrystals and its interface added to a possible diffusion of silicon. The former could influence the size distribution of SiQDs in the films and therefore the location of the luminescent peak.

It is difficult to define without TEM images how the crystalline structure and morphology of silicon nanoclusters could change; however, a reduction of their size under high temperatures is possible.

CHAPTER IV. Light emission of silicon quantum dots devices

To manufacture a LED in the visible range a number of basic material properties must be understood, and technical challenges must be overcome. Critical material properties include electron and hole transport, recombination mechanisms, and the role of defects in these structures.

Unlike photoluminescence, electroluminescence presents an additional challenge: efficient injection of the charge carriers into silicon quantum dots. Electron-hole pairs are usually generated either by bipolar injection from both electrodes of the diode or by impact excitation. In the latter case, only electrons flow through the device and holes are generated by impact processes. The main problem of these structures is their difficulty for carrier injection since the host matrix is usually an insulator.

Structures type metal-insulator-metal and metal-insulator-semiconductor are commonly used to measure electrical properties like capacitance, resistivity, dielectric breakdown and charge transfer mechanisms. The considered issue in MIM capacitors is the possible asymmetry of the electrical properties when the top and bottom electrodes are made of different metals. Different metals generally lead to different work functions, and therefore result in different metal-dielectric interface barriers. The MIS structure is inherently asymmetric [56]. Moreover, recently it has been possible to obtain electroluminescent emission from silicon-based dielectric films using these structures.

In this section of the thesis were fabricated the first electroluminescent devices of silicon nanocrystals embedded in a chlorinated silicon nitride matrix by using the basic structure metal/insulator/metal (MIM). The optical and electrical properties of these samples with different thicknesses of the active film were obtained.

4.1 Current transport processes in metal-semiconductor contacts

The current transport in metal-semiconductor contacts is due mainly to five basic transport processes (figure 26): (1) emission of electrons from the semiconductor over the potential barrier ($q\Phi_B$) into the metal (the dominant process for Schottky diodes with moderately doped semiconductors operated at moderate temperatures (e.g., 300 K), (2) quantum mechanical tunneling of electrons through the barrier (important for heavily doped semiconductors and responsible for most ohmic contacts), (3) recombination in the space-charge region, (4) diffusion of electrons in the depletion region, and (5) holes injected from the metal that diffuse into the semiconductor (equivalent to recombination in the neutral region). In addition, it is possible to have edge leakage current due to a high electric field at the metal-contact periphery or interface current due to traps at the metal-semiconductor interface. Several methods have been used to improve the interface quality, and many device structures have been proposed to reduce or eliminate the edge leakage current [57].

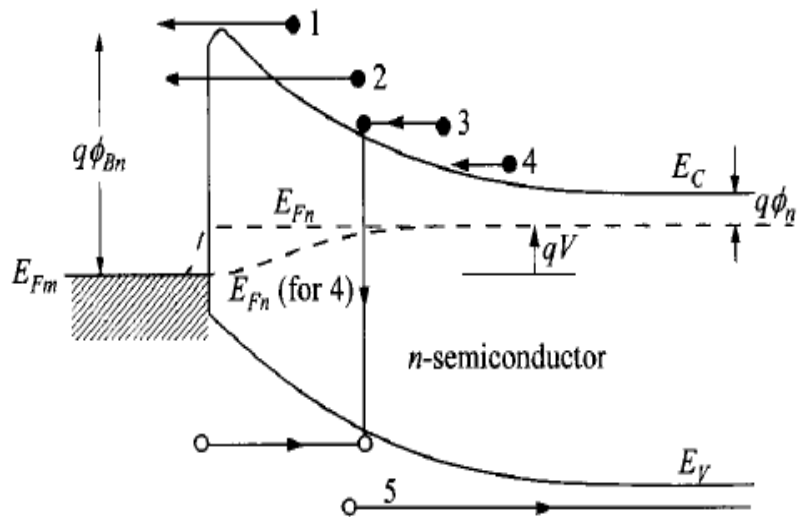


Figure (26) Basic transport processes under forward bias. (1) Thermionic emission. (2) Tunneling. (3) Recombination. (4) Diffusion of electrons. (5) Diffusion of holes [57].

4.2 Basic conduction process in insulators

The main function of a non-crystalline insulating material of a metal-insulating-metal (MIM) device is to avoid current flow between the two electrodes. However, different carrier transport mechanisms through an insulator are possible and determined fundamentally by the properties of the dielectric, the quality of the interfaces and electrodes. The charge transport in non-crystalline insulating materials is determined basically for the following:

- Low mobility of charges because carrier dispersion.
- Localized states during the transport process.

Likewise, in a real MIM or MIS capacitor the insulating film show some degree of carrier conduction when the electric field or temperature is sufficiently high. Some conduction mechanisms depend on the electrical properties at the electrode-dielectric contact. These conduction mechanisms are called electrode-limited conduction mechanisms or injection-limited conduction mechanisms. Also, other conduction mechanisms depend only on the properties of the dielectric itself. These conduction mechanisms are called bulk-limited conduction mechanisms or transport-limited conduction mechanisms. There are a number of essential methods to distinguish these conduction mechanisms, moreover, some of them may all contribute to the conduction current through the dielectric film at the same time [56]. A scheme of the main conduction mechanisms in dielectrics films is shown in figure (27).

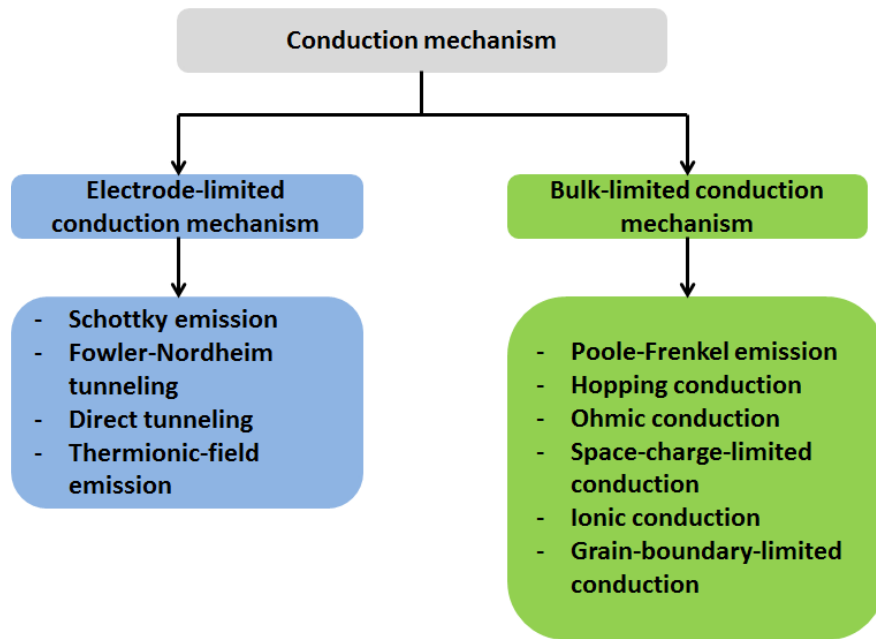


Figure (27) Classification of conduction mechanisms in dielectric films [56].

The equations modeling the conduction processes in insulators are summarized in table 1A (Appendix A). These equations also emphasize the voltage and temperature dependence of each process that is used often to identify the exact conduction mechanism experimentally.

At low voltages and room temperature, the principal conduction mechanism in silicon nitride films is that where current is carried by thermally excited electrons hopping from one isolated state to the next. This mechanism yields an ohmic characteristic exponentially dependent on temperature [57]. The space-charge-limited current gives rise carriers injected into a lightly doped semiconductor or a dielectric, where no compensating charge is present. The current for the unipolar trap-free case is proportional to the square of the applied voltage. The mobility regime is relevant here since mobility is typically very low in insulators. Tunneling increases for ultra-thin insulators such that the conduction approaches that of the metal-semiconductor contact where the barrier is measured at the semiconductor surface instead of the insulator and the thermionic-emission current is multiplied by a tunneling factor.

Under high fields, tunneling is the most-common conduction mechanism through insulators. The tunnel emission has strong dependence on the applied voltage but is essentially independent of the temperature. This mechanism can be divided into direct tunneling and Fowler-Nordheim tunneling where carriers tunnel through only a partial width of the barrier. In the Schottky emission process thermionic emission over the metal-insulator barrier or the insulator-semiconductor barrier is responsible for carrier transport. In table (1A), the term subtracting from Φ_B is due to image-force lowering.

The Poole-Frenkel mechanism models the emission of trapped electrons into the conduction band. The supply of electrons from the traps is through thermal excitation, where the barrier height is the depth of the trap potential well. For trap states with Coulomb potentials, the expression is similar to that of the Schottky emission. The barrier reduction is larger than in the case of Schottky emission by a factor of 2, since the barrier lowering is twice as large due to the immobility of the positive charge.

With regard to ionic conduction, this is similar to a diffusion process. Generally, the dc ionic conductivity decreases during the time the electric field is applied because ions cannot be promptly injected into or extracted from the insulator. Positive and negative space charges will build up near the metal-insulator and the semiconductor-insulator interfaces after an initial current flow, causing a distortion of the potential distribution. Large internal fields remain when the applied field is removed which cause some, but not all, ions to flow back toward their equilibrium position. Because of this, hysteresis results in I - V traces.

Each conduction process may dominate in certain temperature and voltage range for a particular insulator. The processes are also not exactly independent of one another and should be carefully examined [57].

4.3 SiQDs-based electroluminescent devices on glass

From the results about thermal treatments obtained in chapter III, an important change on optical and chemical properties of active films as-grown and annealed at 400°C was not observed. On the other hand, the PL of films cured at temperatures $\geq 500^\circ\text{C}$ diminished as non-radiative processes became more important. Thus, post-deposition thermal treatments at relatively low temperatures in a conventional furnace demonstrated no advantages of the active film properties and it was decided to use the as-grown films for fabricating light emission diodes based in silicon nanocrystals.

4.3.1 Fabrication process steps

The first electroluminescent structures were fabricated on glass as substrates to allow radiative emission in a capacitor configuration. This type of structure was chosen because of its easy manufacturing process. As transparent conductive contact (TCC) aluminum doped zinc oxide (ZnO:Al) was used and whose properties have been mentioned before. After deposition of the TCC, two depositions of SiQDs were made in order to take out the sample after the first deposition and clean it with nitrogen gas before the second. This procedure demonstrated to avoid pin holes in the samples and improve electrical performance of the device. Finally, it was deposited aluminum as a contact electrode on the top of the structure by vacuum evaporation. The scheme of the fabricated devices can be seen in the figure (28).

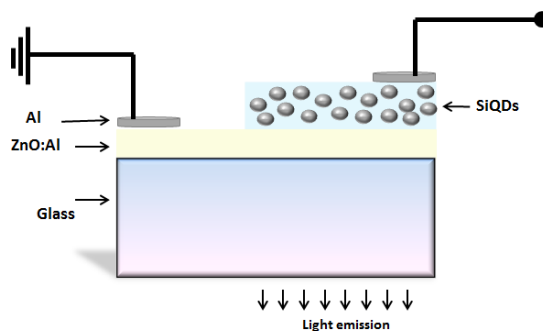


Figure (28) Scheme of light emission devices on glass for positive bias.

The thickness of the SiQDs films deposited on n type low resistivity silicon ($0.1-2 \Omega\text{cm}$) was measured by null ellipsometry and color table. Transparent conductive contact was deposited on glass and quartz. Fabrication process consisted of the following stages:

Cleaning of glass and quartz substrates for deposition of the transparent conductive contact (ZnO:Al):

- Dive in trichloroethylene (TCE) for 10 min using ultrasonic bath.
- Dive in acetone for 10 min using ultrasonic bath.
- Dive in methanol for 10 min using ultrasonic bath.
- Blow with high purity nitrogen.
- Deposition of ZnO:Al by ultrasonic spray pyrolysis (see section 2.1.3) as the TCC.
Thickness (Th): $1\pm 0.2 \mu\text{m}$

Steps for deposition of the active film and metallization:

- The cleaning of the silicon substrates was the same used in chapter three.
- Deposition of SiQDs embedded in $\text{SiN}_x\text{:Cl}$ on TCC and silicon substrates by RPECVD system. The gas flow rates and parameters of deposition were those employed in chapter three.

NH_3 Flow rate (sccm)	SiH_2Cl_2 Flow rate (sccm)	H_2 Flow rate (sccm)	Ar Flow rate (sccm)	Substrate temperature ($^\circ\text{C}$)	Power of plasma(Watts)	Chamber pressure (mTorr)
200	5	20	75	300	150	300

- Metallic layer deposition. Aluminum metal was deposited by thermal evaporation. This equipment employed mechanical and diffusion pumps to get pressures of the order of 10^{-6} Torr. High purity aluminum is placed on a crucible which by Joule effect is evaporated and

deposited on the active film through a mask used to define circular patterns of 1mm diameter. The thickness of these aluminum layers was ~100 nm.

4.4 Thickness effect of the active film on the EL properties

Since the thickness of the films could be estimated through deposition time and the photoluminescence of the samples is related to the number of SiQDs in the volume [23], different thicknesses of SiQDs films were deposited in order to understand the behavior of the injected current in these films and its relation with the luminescence emitted. Four light emission devices were built with active layers from 44 nm to ~200 nm thickness. As can be observed from table (5), the refractive index of the four samples at 632 nm differed just for hundredth parts as the films were thinner which indicates repetitive deposition and homogeneity of the active layers. These values were consistent with those observed for silicon rich nitride, and very close to the stoichiometric silicon nitride value ($n=2$).

Device	Thickness (nm)	Characterization method	Refractive index (n)
M4	≈200	Color table	----
M3	132.5	Null ellipsometry	1.847
M2	91.6	Null ellipsometry	1.839
M1	44.1	Null ellipsometry	1.823

Table (5) Thickness and refractive index of the active films of the fabricated LEDs.

4.4.1 Optical and electrical characterization

In order to know the flux of light through the deposited layers the transmittance percent of ZnO:Al ($1\pm 0.2\mu\text{m}$) on glass and the layered structure SiQDs($\sim 90\text{nm}$)/ZnO:Al($\sim 1\mu\text{m}$) on quartz was measured (figure 29). ZnO:Al had a transmittance of 70-80% in a range of $\sim 400\text{-}1100\text{ nm}$. Transmittance of the layered sample decreased between $\sim 349\text{-}700\text{ nm}$ ($3.55\text{-}1.77\text{ eV}$) due to absorbance of the SiQDs film (this absorbance was found at the same range of the SiQDs as-grown sample in chapter III). The difference in the percentage of transmittance in this range was $\sim 10\%$ with regard to only ZnO:Al on glass.

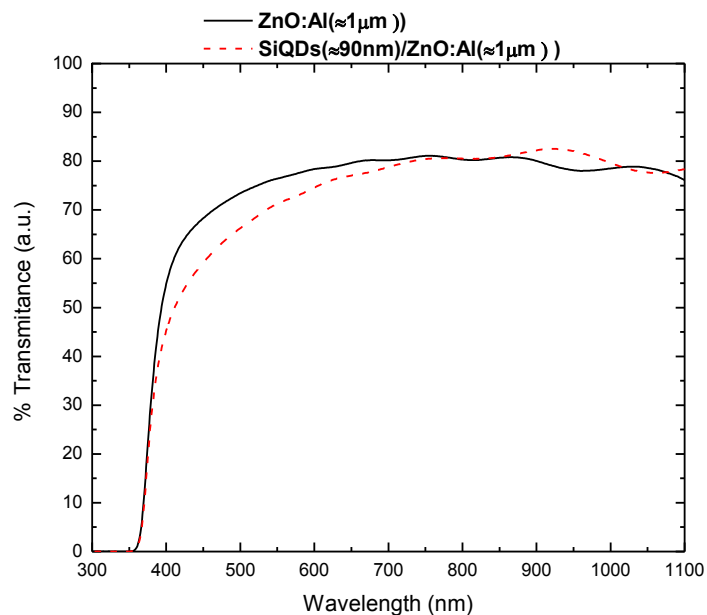


Figure (29) Transmittance spectra of ZnO:Al($\approx 1\mu\text{m}$) and SiQDs($\approx 90\text{nm}$)/ZnO:Al($\approx 1\mu\text{m}$).

Photoluminescence spectra of the four samples are presented in figure (30). As can be seen in table (6) PL peak position did not change in samples M2, M3 and M4. However, the peak of the sample M1 was blue-shifted. The sample M4 is ~ 4.5 times thicker than sample M1.

Device	Thickness (nm)	PL peak (nm)	Integrated PL (counts/sec)
M4	≈ 200	493	25.96E7
M3	132.5	494	14.58E7
M2	91.6	494	5.38E7
M1	44.1	472	1.36E7

Table (6) PL peak and integrated PL intensity of the SiQDs films.

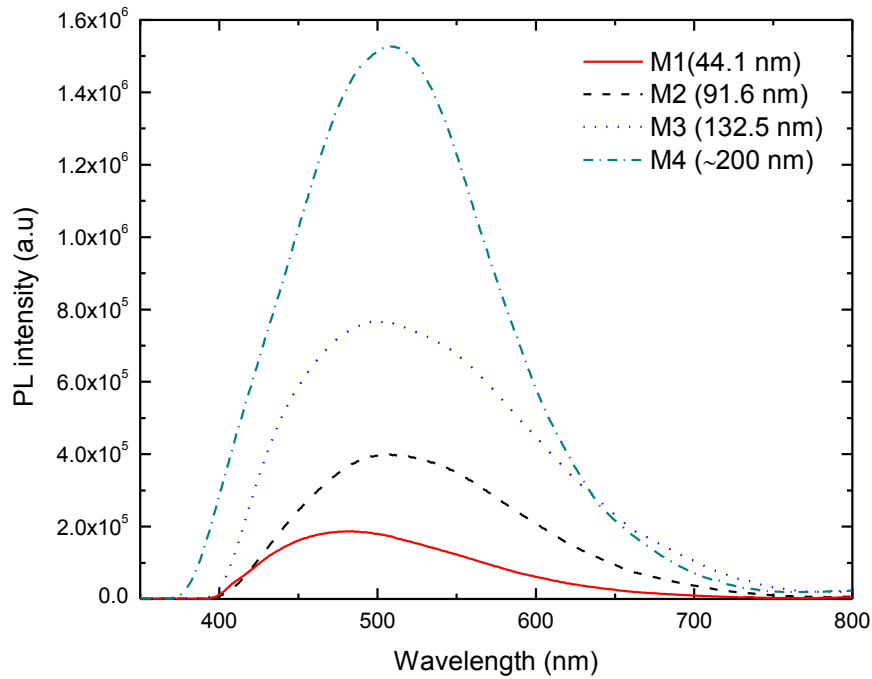


Figure (30) PL intensity of the samples M1, M2, M3 and M4 as-grown.

A complete scheme of the experimental set-up for measuring the fabricated electroluminescent structures is depicted in figure (18) in chapter II. The transparent conductive contact (ZnO:Al) is a n-type semiconductor. Therefore, the junction ZnO:Al/SiQDs(SiNx:Cl) can be considered as a Schottky junction [58]. The forward bias is that shown in figure (28) with positive terminal on the active film. All the samples were placed at the same distance from the optical fiber; meanwhile the voltage was applied by time-defined short steps. These short voltage steps in forward and reverse bias (known as “electrical burning”) were realized in order to stabilize electrically the structure.

Electroluminescent (EL) spectra of the four samples (figure 31) were obtained in positive and negative bias which indicated negligible resistance regardless of the polarity of the applied voltage in all the devices. However, in most cases higher EL intensities were observed in forward bias than in reverse bias despite the fact that the same electric field was applied. The EL turn on voltages (determined when light emission is detected by the measurement setup in a dark room) increased when thicker SiQDs films were deposited because of the lower electric fields (V/cm) through these samples. Voltage steps of 1 Volt were required to obtain increased EL intensity in M1, M2 and M3 samples, meanwhile, for M4 sample (~200 nm thickness) a slightly change of EL intensity was observed at voltage steps of 2 Volts. EL intensity increased as more current density was injected on each sample indicating a direct relation between injected carriers and activated luminescent centers. The shape of the EL spectra and peak location did not change after a determined applied voltage for all the samples.

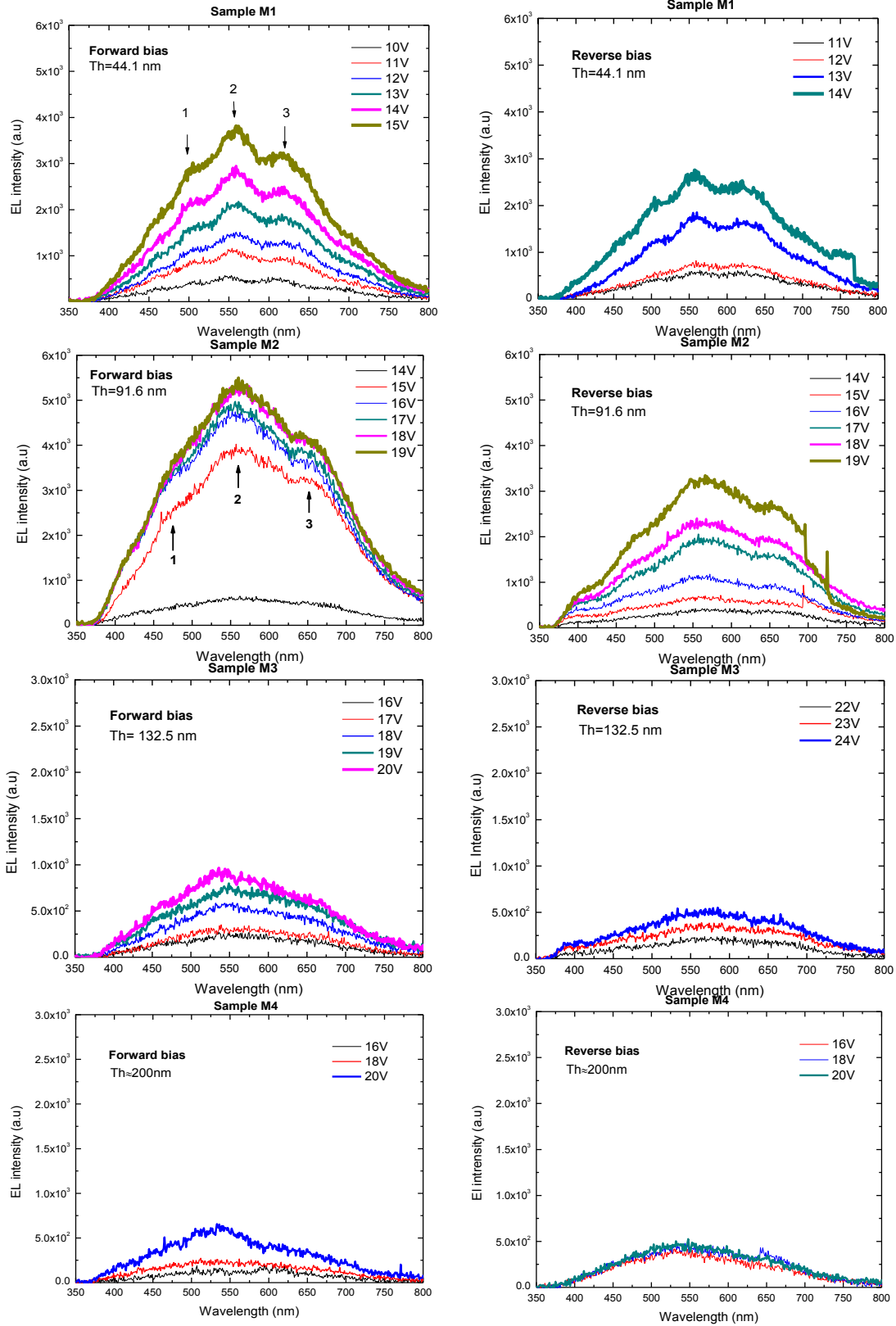


Figure (31) Electroluminescence spectra of samples M1, M2, M3 and M4 in forward and reverse bias.

The carrier injection induced electrically is more difficult than the one induced optically since electrically injected carriers have to travel through the dielectric matrix by preferential conductive paths to arrive at silicon quantum dots which may promote connection of the top and bottom electrodes [59]. Thus, it is understandable the much lower EL light emission achieved compared with PL emission (~40 times lower).

The relation between electric field and the integrated electroluminescence intensity in forward bias is depicted in figure (32). The electric field (E) was higher as the thickness of the samples decreased since $E=Volts/thickness$. Samples M3 and M4 presented lower electric fields and lower integrated EL intensities probably due to inefficient current injected on thicker active films. Moreover, it is worth to highlight that applied voltages greater than 20V led to breakdown of these structures even though a major film thickness probably by tunneling of hot electrons. Higher electric fields are shown in samples M1 and M2 and also considerably higher integrated EL intensities. However, in spite of the active film of sample M1 is thinner than M2 and had the highest electric field on it, sample M2 showed the highest integrated EL intensities.

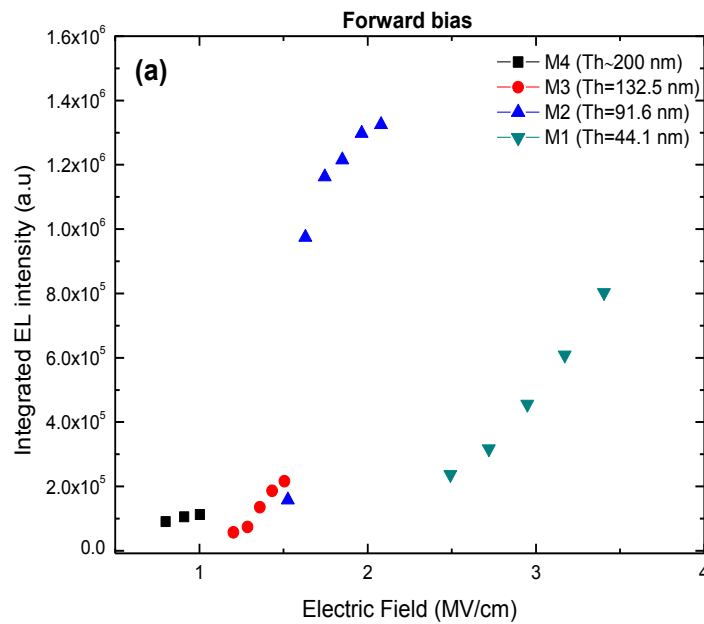


Figure (32) Integrated EL intensity against electric field of the light emission devices.

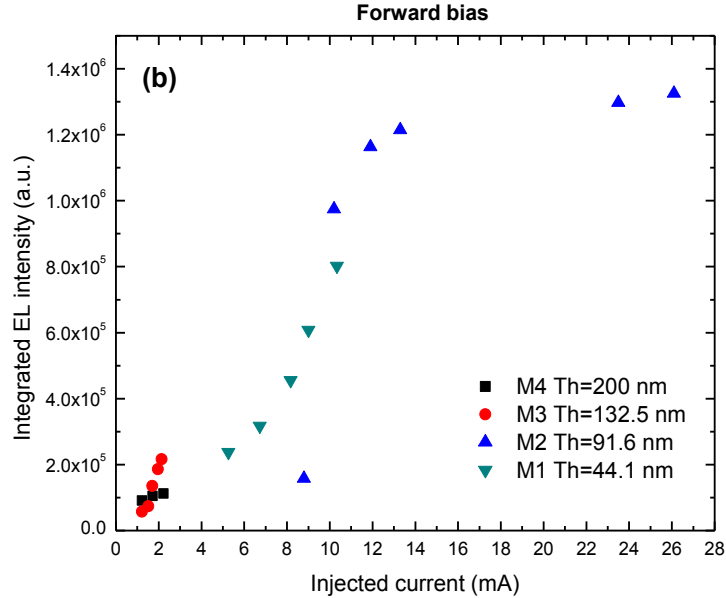


Figure (33) Integrated EL intensity against injected current of the light emission devices.

The latter can be explained by means of the injected current vs EL intensity plot in forward bias (figure 33). From this plot is observed that the raise of EL intensity was related to the increment of leakage current through each device which indicates that EL intensity depends on increment of carriers injected. Almost constant EL intensity was observed in sample M4 revealing inefficient conducting paths in the bulk of the dielectric and therefore very low excited emission centers. Even tough in sample M2 lower electric fields were seen compared to sample M1, its current injection diverged from a straight line from 16 Volts (~12 mA) which gave rise to higher EL intensities. As the EL emission spectra of this sample grew up abruptly under applied voltages it is probable that a higher quantity of interfacial defects in the ZnO:Al/SiQDs interface introduced during fabrication could help to promote carrier injection and consequently conductive paths. Moreover, it has been studied that the roughness at the bottom interface of MIM capacitors promotes higher electric fields and higher currents [60].

As mentioned previously, some of the mechanisms used to explain optical emission in non-stoichiometric amorphous silicon nitride films are: a) the radiative recombination through a quasidirect energy level in silicon quantum dots by quantum confinement effect and, b) defect states in the host matrix or defects in the SiQDs band gap by interface states.

With regard to the optical emission of the devices on glass, the EL spectra in forward bias of samples M1 and M2 showed three well defined peaks, of which only the second one was observed in samples M3 and M4 (Table 7). The latter may be an effect of lower electric fields through these samples and as a result, lower amount of carriers injected to the luminescent centers. It could be possible that in thicker active layers there are less conductive paths than in thinner layers and therefore, less radiative and non-radiative processes take place. Very close EL peaks have been seen before by Pei et al. [61] from highly silicon-rich a-SiN_x:H based light emitting structures in 2.48,

2.21, 2.1 and 1.90 eV. This work correlated these peaks to those energies of defects found theoretically by J. Robertson et al. [47] in amorphous silicon nitride. Pei et al. [61] proposed that emissions between 2.4-2.5, 2.2-2.3 and 1.9-2 eV were originated from different transitions between the E_c (conduction band), $\equiv\text{Si}^-$, $\equiv\text{Si}^0$ and $=\text{N}^-$ defect states in the gap of the matrix which acted as luminescent centers in the hydrogenated a-SiNx.

Sample	Peak 1	Peak 2	Peak 3
M1 (44.1 nm)/15V	~505 nm/ 2.46 eV	~559 nm/2.22 eV	~617 nm/2 eV
M2 (91.6 nm)/15V	~482 nm/2.57 eV	~560 nm/2.21 eV	~655 nm/1.89 eV
M3 (132.5 nm)/20V		~546 nm/2.27 eV	---
M4 (~200 nm)/20V	---	~544 nm/2.28 eV	---

Table (7) Electroluminescence peaks found in the samples M1, M2, M3 and M4 in forward bias.

Moreover, R. Huang et al. [62] observed two components of EL at 1.75 and 2.25 eV in silicon nanodots embedded in silicon nitride. They found that the emission peaks of the PL bands at different excitation wavelengths were very close to those EL peaks, and explained light emission of these luminescent layers through two mechanisms: a) radiative recombination at silicon dangling bonds in the a-SiNx host matrix (2.25 eV) and b) band to band radiative recombination in the silicon nanodots (1.75 eV). They considered that the dangling bond (K0) center was related to the excitation process and thus, a possible PL mechanism proposed was photogeneration of carriers taking place in these centers, meanwhile radiative recombination occurred in the quantum confined Si nanodots.

Figure (34) depicts the normalized PL and EL spectra of the sample M2 at 15V in which was found the maximum EL emission. From previous works, A. Rodriguez et al. [23] proved that the chemical composition of the films, the morphology, average size and size distribution of the silicon quantum dots did not change in a thickness range of ~30 nm to 4500 nm. They accounted the major contribution of the photoluminescence of these chlorinated Si rich silicon nitride films to the radiative recombination of electron hole-pairs in the silicon nanoparticles, according to the quantum confined model. However, in order to explain the excitation-emission mechanisms in these films it was needed to introduce the concept of band tails by localized states below the conduction band and above the valence band of the silicon nitride matrix (as mentioned in chapter 3). Thus, the energies of absorption E_{g1} and E_{g2} were related to the energy absorption in band tails and in the silicon nitride matrix, respectively. Additionally, a small absorption band with peak at ~2.5 eV was related to interband optical transitions in the SiQDs which was the origin of PL emission. Moreover, considering that the density of Si nanoparticles in the films is relatively high (about $6E12$ particles/cm²) and the average size of the particles is ~3.1 nm [23], it could be reasonable to think about a critical influence on the carrier transport and also electroluminescence from interface states related bonds created between the SiQDs and the host matrix and/or from states originated in the host matrix.

As could be seen in chapter III from the Tauc plot of as-grown SiQDs film (~200 nm), E_{g1} and E_{g2} were 3.4 and 4.04, respectively. Likewise, two absorption peaks were found at 2 and 3.2 eV, respectively. However, distortions in the spectra due to interference effects by the presence of nanodots and not to intrinsic changes are present when the thicknesses of the films are a few hundred nanometers [63]. Therefore, it is more exact to take the peak value of this little absorption

band from that obtained in [23] at 2.5 eV (from 2 to 3 eV). Considering the latter, the observed EL peaks 1 and 2 (~ 2.57 eV and ~ 2.21 eV for sample M2) at higher energies may be due to radiative recombination in SiQDs, meanwhile the peak 3 at lower energy (1.89 eV) may be originated by defect states in the silicon nitride matrix.

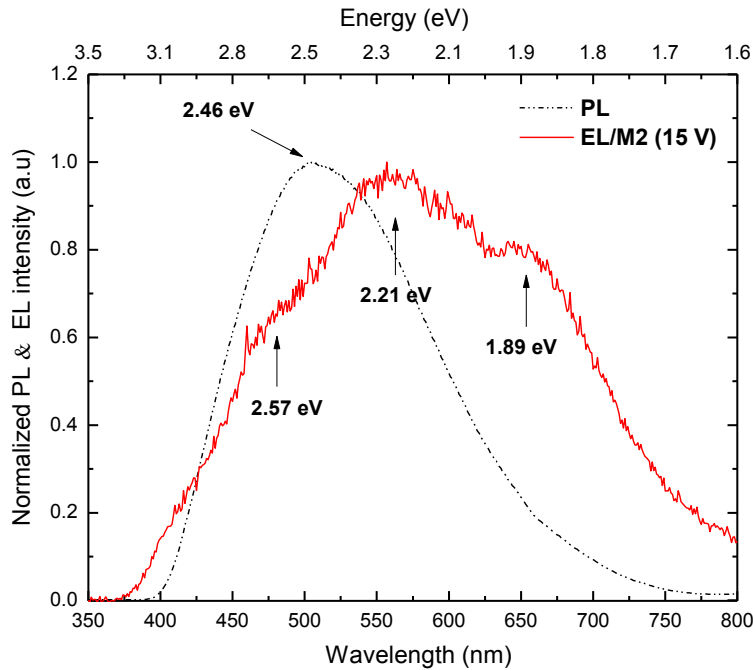


Figure (34) Normalized PL and EL spectra of the sample M2.

The current-voltage curves of the four samples are shown in figure (35). By using these data it is possible to understand the possible conduction mechanisms in the samples, although it is expected a complex behavior of the SiQDs film embedded in a chlorinated matrix due to the presence of silicon nanodots. From the figure, it can be observed samples M3 and M4 presented low current in forward and reverse bias as well as similar trend. Samples M2, M3 and M4 showed slightly higher current in forward bias probably due lower tunneling barrier height. Conversely, the sample M1 showed asymmetry behavior breaking at ~ -12 V. This may be due to previous “electric burning” in forward bias and therefore more important damage in the thinnest insulating film by leakage current. Furthermore, it is worth mentioning that the current of all samples in forward and reverse bias were stable just after a few minutes the voltage was applied.

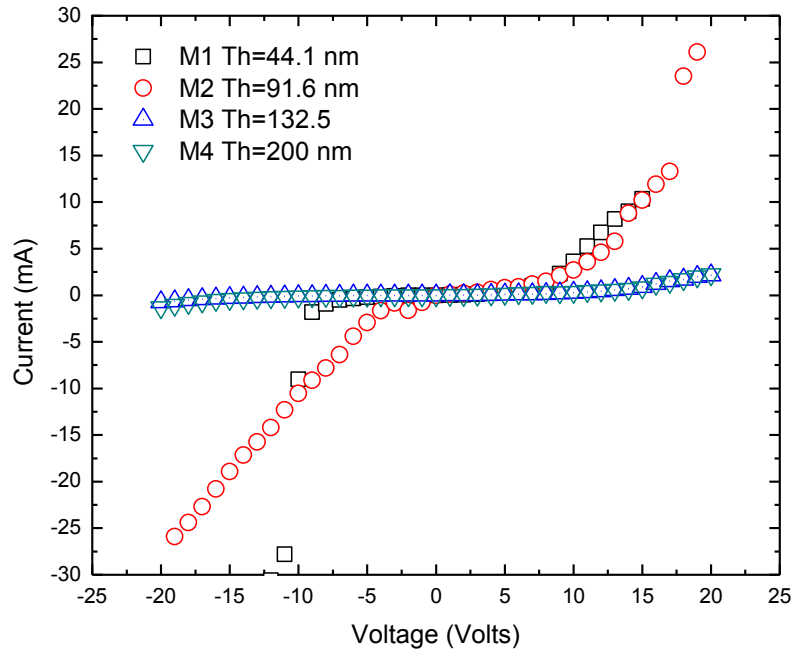


Figure (35) Current-Voltage plot of the electroluminescent devices in forward and reverse bias.

With the aim to discriminate different behavior regions in these curves, the current density-electric field plots in logarithmic scale of the samples with highest luminescence (M1 and M2) in forward bias are depicted in figure (36). Both samples presented two main slopes defining the regions I and II (the red vertical line is the crossing point of both slopes). These regions exhibit different behaviors that can be considered as follows:

1. Low electric field:
 For sample 1 $0.45 < E < 1.58$ MV/cm
 For sample 2 $0.11 < E < 0.65$ MV/cm

2. High electric field:
 For sample 1 $1.81 < E < 2.94$ MV/cm
 For sample 2 $0.87 < E < 1.85$ MV/cm

As mentioned previously, at low electric fields and at room temperature an Ohmic mechanism dominates. In this mechanism the current density is related to the electric field by the equation:

$$J = \sigma E = \frac{qn\mu}{d} V = const V^\gamma$$

where:

σ =conductivity
 μ =mobility
 n = carrier concentration
 q =electric charge

d =thickness of the insulating film
 V =Voltage

If $\gamma=1$ the conduction is limited by ohmic behavior, if $1 < \gamma < 2$ a conduction limited by spatial charge dominates.

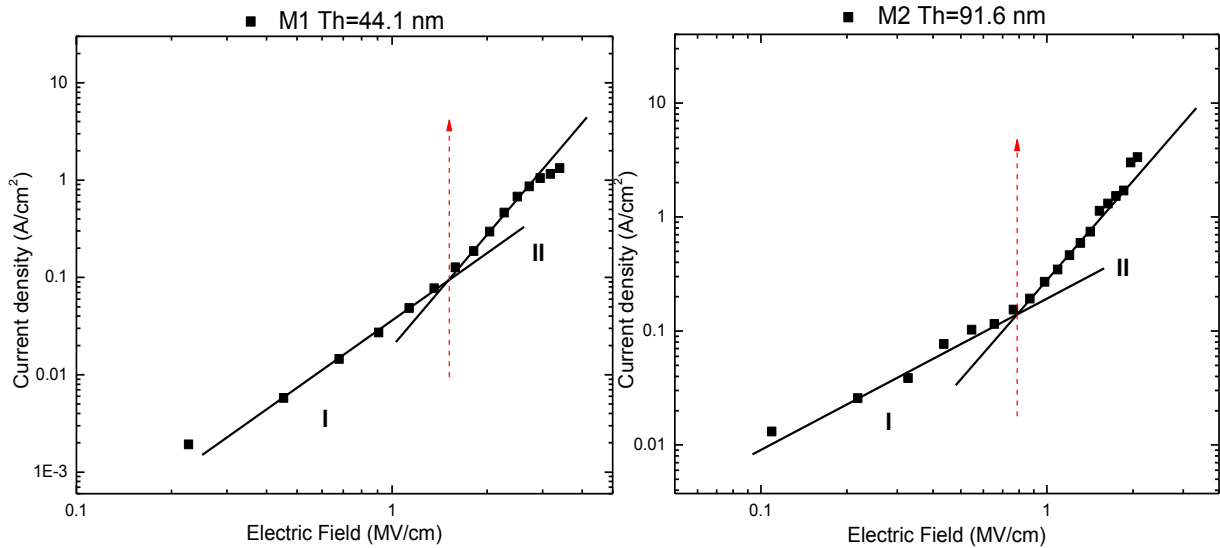


Figure (36) Current density vs electric field of the samples M1 and M2.

The fitting of the region I (low field) for samples M1 and M2 is depicted in figure (37). The slope value γ for sample M1 (Th=44.1 nm) was 2.43 which indicated a transport mechanism more complex possibly involving traps states. Moreover, the sample M2 (Th=91.6 nm) had a value of $\gamma=1.28$ corresponding to a conduction mechanism limited by spatial charge whose effect limits the injection of carriers to the conduction band of the insulating.

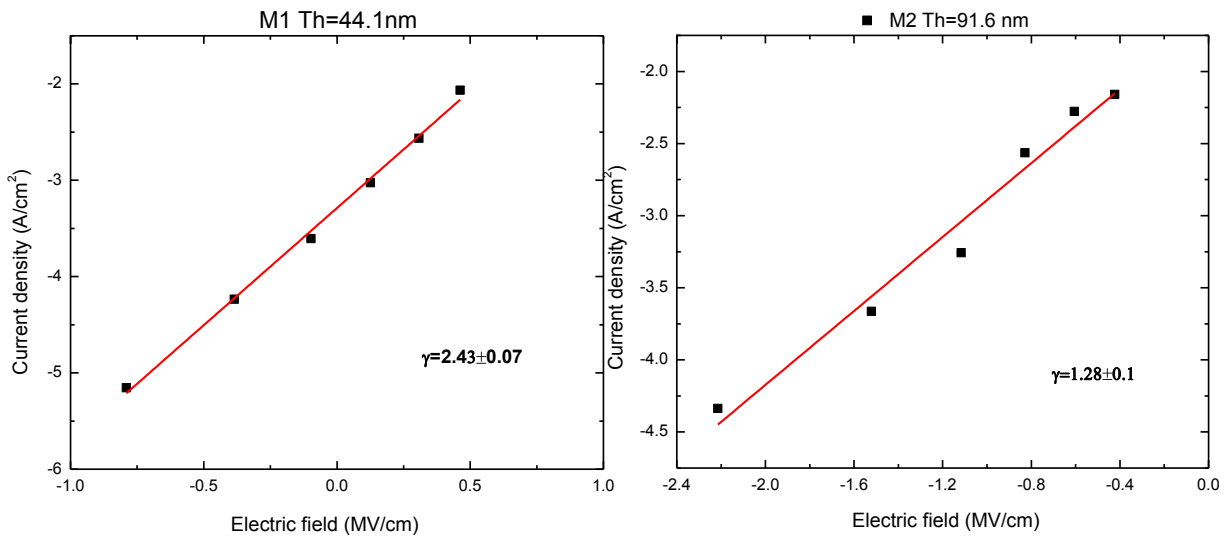


Figure (37) Low field fitting of the transport mechanisms for samples M1 and M2.

Likewise, the Fowler-Nordheim (F-N) Tunneling and Poole-Frenkel (P-F) emission models have been widely used to explain charge transport in silicon quantum dots embedded in an insulating matrix at high fields [14, 62, 64, 65]. F-N tunneling occurs when the applied electric field is large enough so that the electron wave function may penetrate through the triangular potential barrier into the conduction band of the dielectric [56]. Thus, the expression for this mechanism is:

$$J = \frac{AE^2}{\Phi_B} \exp\left[-B \frac{\Phi_B^{\frac{3}{2}}}{E}\right]$$

where:

$$A = q^3/8\pi hq$$

$$B = 8\pi(2qm_T^*)^{1/2}/3h$$

Φ_B = barrier high

q = electronic charge

k = Boltzmann's constant

h = Planck's constant

m_T^* = tunneling effective mass in dielectric

E = electric field

Moreover, the Poole-Frenkel emission implicates a mechanism which is very similar to Schottky emission; that is, the thermal excitation of electrons may emit from traps into the conduction band of the dielectric [56]. For a Coulombic attraction potential between electrons and traps, the current density due to the P-F emission is:

$$J = q\mu N_C E \exp\left[-\frac{q(\Phi_T - \sqrt{(qE/\pi\epsilon_i\epsilon_0)})}{kT}\right]$$

where:

N_C = density of states in the conduction band

$q\Phi_T (= \Phi_T)$ = trap energy level

ϵ_0 = permittivity in vacuum

ϵ_i = dynamic dielectric constant

T = absolute temperature

Additionally, the trap-assisted tunneling (TAT) transport process was also explored. This mechanism is ascribed to defect states into the films which arise in silicon nitride when deposited by RPECVD. The equation for the TAT model is [66]:

$$J = \exp\left[\frac{8\pi\sqrt{2qm^*}}{3hE} \Phi_T^{\frac{3}{2}}\right]$$

where:

m^* = effective mass in dielectric

Φ_T = trap energy below the conduction band

The results of the fitting of these models to the current density-electric field data of samples M1 and M2 are summarized in table (8). Considering the standard error like a factor of selection, for the sample M1 the trap assisted tunneling mechanism (TAT) fitted better a straight line, followed for P-F and F-N models. In the case of the sample M2, the Fowler-Nordheim (F-N) mechanism was the best fitting followed for the P-F and TAT models.

The prevalence of the TAT mechanism observed in sample M1 (Th=44 nm) can be explained as carriers in localized states traps in the band gap of the silicon nitride are more easily excited out of these traps to the anode or other traps into the dielectric under an electric field. Additionally, interface states in the ZnO:Al/SiQDs junction at the bottom of the MIM structure due to higher roughness of the ZnO:Al film when deposited on glass are an important factor for leakage current. Likewise, the F-N tunneling could be a principal carrier transport process in the sample M2 since higher thicknesses promotes the tunneling of hot carriers which was confirmed by highest current seen through this device. The plots of the F-N, P-F and TAT fittings of each sample are shown in figure (38).

Sample M1	Fitting range (MV/cm)	Slope	Sample M2	Fitting range (MV/cm)	Slope
<i>Pool-Frenkel</i>	1.81-2.94	3.44±0.28	<i>F-N</i>	0.87-1.85	-1.2±0.134
<i>TAT</i>	1.81-2.94	-8.35±0.19	<i>TAT</i>	0.87-1.85	-3.76±0.2
<i>F-N</i>	1.81-2.94	-3.78±.28	<i>Pool-Frenkel</i>	0.87-1.85	3.55±0.15

Table (8) Data of the fitting mechanisms of the devices M1 and M2.

An image illustrating the connection between silicon nanodots through wide band regions (silicon nitride) is shown in figure (39a). An electric field will be strong in the silicon nitride regions of the microscopic structure because of their higher resistivity and lower dielectric constant [67]. Compared with silicon dioxide, silicon nitride has a lower band gap (~5 eV) and then, higher probability of carriers tunneling from silicon nanodots. Since the electroluminescence from the fabricated samples was observable at relatively high voltages (≥ 10 Volts), it is expected a large bending of the conduction and valence bands of the silicon nanodots and the insulating.

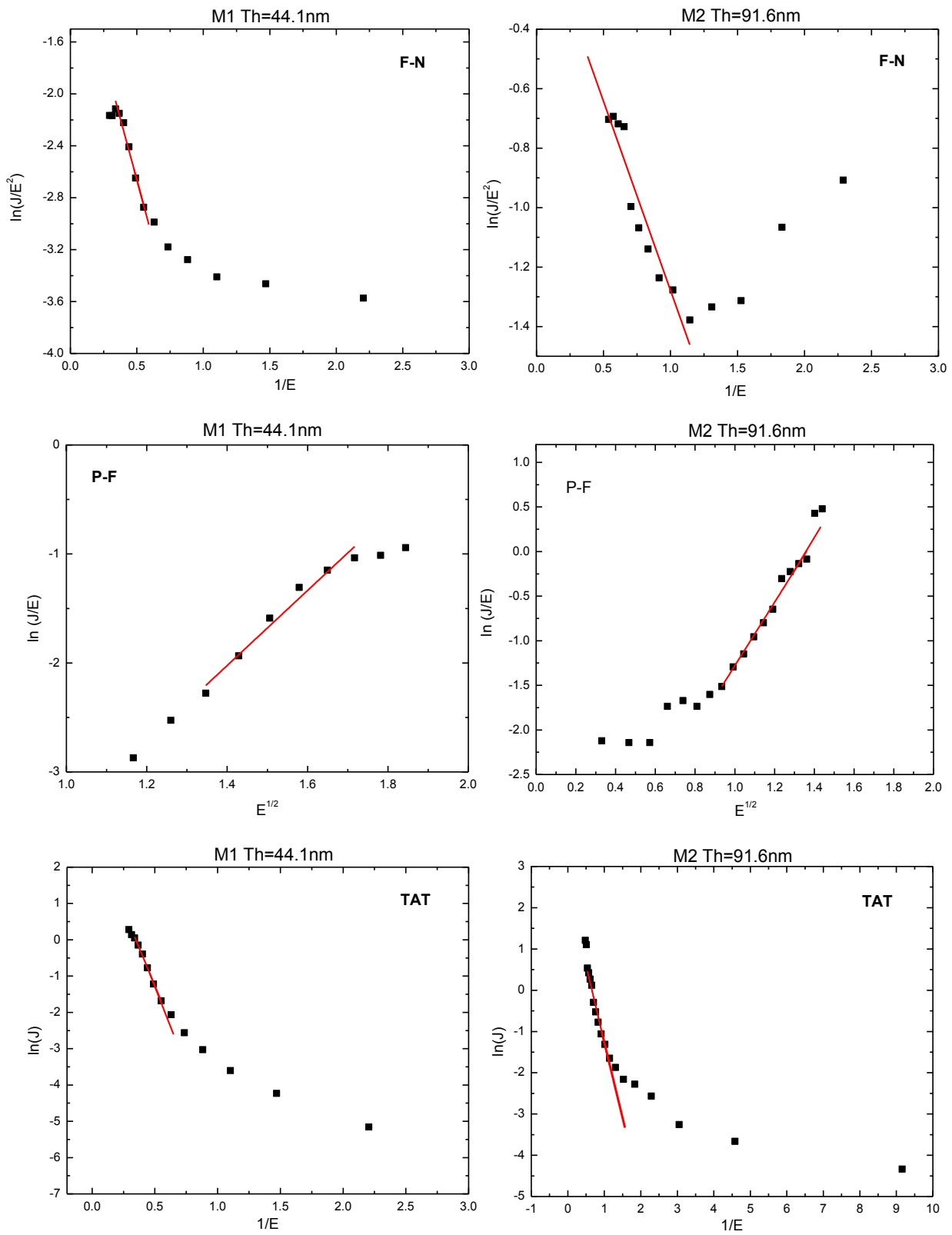


Figure (38) F-N, P-F and TAT fitting mechanisms of samples M1 and M2.

A band diagram of the MIM structure under high electric field in forward bias is depicted in figure (39b). ϕ_M is the work function of the metal, ϕ_{B1} is the barrier height formed at the interface ZnO:Al/SiQDs and ϕ_{B2} is the barrier height of the interface Al/SiQDs.

From the last figure, carriers are injected in forward bias from the cathode to the anode. As mentioned earlier at the beginning of this chapter, the carrier transport in insulating films can be due to thermal excitation of electrons above the barrier (1), tunneling of carriers from the cathode to the conduction band through the barrier (2), tunneling of carriers from localized states to the conduction band of the dielectric (3), tunneling from the valence band of the dielectric to the anode (4) or tunneling between localized states (5) among others.

In the transport processes of the SiQDs-based devices must be considered that the silicon nanodots are uniformly distributed in the volume inside the insulator which allows direct tunneling between them. Thus, at higher electric fields energetic electrons from the cathode may tunneling to the conduction band of a nanodot, where they are accelerated to the conduction band of the neighboring one creating an electron-hole pair by impact ionization; likewise, the incoming hot electrons may originate holes in the valence band of the silicon nanodots by the same process. Additionally, an energetic electron from the valence band of the silicon nanodot may tunnel to the conduction band of the neighboring one giving rise to electrons-holes pairs which are able to recombine radiatively [67]. Additionally, localized states could act as luminescent centers since a peak emission attributed to them was observed previously in the EL spectrum of samples M1 and M2. From moderate to high electric fields, electrons in traps can be excited to the conduction band of the dielectric where thermalizes and then becomes re-trapped at another localized state until eventually it can be captured by a radiative or non-radiative center. Also, it is possible that an electron in a trap state in the insulator recombines with a hole in the dielectric valence band.

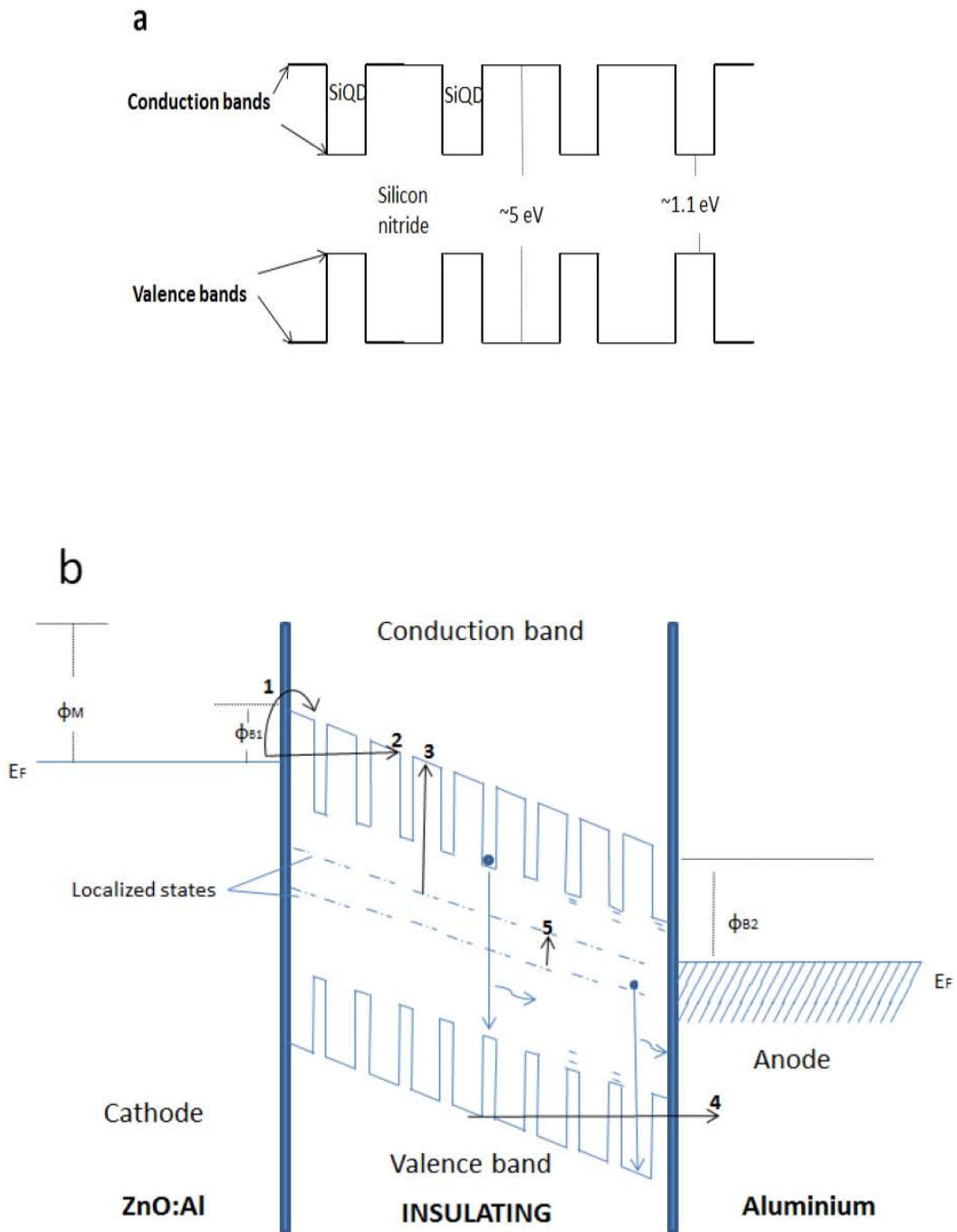


Figure (39a) Scheme of silicon nanocrystals attach to a wide-gap dielectric and (39b) Band diagram of the MIM structure of the fabricated devices.

4.5 Conclusions

Four samples based on SiQDs were fabricated using different thicknesses. As expected, electric field increased when the thickness of the active film decreased finding higher radiative intensities in samples M1 and M2. However, it was observed that electroluminescent emission intensity did not depend completely on thickness since EL intensity was higher in sample M2 than M1. Highest current injection was found in sample M2 probably due to interface states generated during fabrication in the ZnO:Al/SiQDs interface since the integrated EL intensity vs. Current injected plot was not lineal. Likewise, samples M1 and M2 presented three peaks which were very close to those found for some authors in silicon nitride matrixes. These authors related these peaks to different transitions between the conduction band and defect states like $\equiv\text{Si}^-$, $\equiv\text{Si}^0$ and $\equiv\text{N}^-$ in the gap of the matrix. The latter can be possible since it is well known that silicon nitride deposited by PECVD system incorporates a great amount of defects in the matrix. Nevertheless, the origin of peaks 1 and 2 was attributed to emission in silicon nanodots. Therefore, quantum confinement and interface states in the silicon nitride matrix should be considered to explain radiative processes. The samples M1 and M2 showed the highest current densities and integrated EL intensity, as well as the lowest EL turn-on voltage. The trap assisted tunneling (TAT) conduction mechanism fitted well the sample M1. This might be due to higher electric fields through this device activating more easily the traps into the thin dielectric. Moreover, the Fowler-Nordheim tunneling fitted better sample M2. It was found that the thickness of this sample ($T_h=91.6$ nm) had the better electrical properties at low and high electric fields to be implemented in subsequent processes.

CHAPTER V. Photoluminescence enhancement

Materials engineering is now being actively applied to Si in an attempt to overcome the low efficient emission from silicon based structures. Some explored alternatives include doping of impurity centers (for example rare earth impurities, carbon complexes and sulfur-oxygen complexes) to induce recombination at them, to use hybrid methods for integrating direct gap materials with silicon, multilayers structures and more recently to employ the coupling of metal nanostructures in the vicinity of SiQDs films to enhance light emission. In this chapter the optical properties of gold nanostructures deposited by sputtering in the vicinity of SiQDs are studied for the purpose of improving radiative emission from the active film.

5.1 Luminescent films in the vicinity of nanostructured noble metals

Biteen et al. [16] showed the first evidence of PL enhancement from SiQDs coupled to gold nanostructures and reported on a separation distance resolved study of radiative decay rate. Moreover, the enhancement or quenching of PL of silicon nanocrystals in the vicinity of silver nanoparticles (NP) has been reported [68]. These groups are characterized by using expensive sample preparation methods like ion implantation to form SiQDs. Additionally, electroluminescent enhancement has also been proved in light emission diodes by coupling of the silicon nanoparticles to silver nanostructures [17, 18, 69].

One possible cause proposed to explain the increased luminescence is that small metal particles ($\leq 20\text{nm}$) or even metal nanostructures strongly concentrate electric fields, so an enhanced local field is presented about the metal through a kind of plasmonic effect. Thus, a silicon nanocrystal in this enhanced field will have an altered optical density of states which will enhance the decay rate of the SiQDs emission [16]. Also, the roughness effect on the surface of metal nanostructures has been considered a factor that helps its coupling with active films of silicon nanocrystals [16, 70, 71]. However, a plasmonic effect in systems like these has been challenged because of the required metal nanoparticle size and the required distance to them to obtain the enhanced fields.

Considering the foregoing it was proposed to build multilayered structures by coupling silicon nanocrystals to gold nanostructures. For its fabrication, Remote Plasma Enhanced Chemical Vapor Deposition (RPECVD) and Sputtering techniques were combined into a method which had a very strong rapport with those used in the microelectronics industry, i.e. dry, low temperature, economical and fast depositions.

5.2 Gold nanostructures fabricated by sputtering

In order to get coupling between Au nanostructures and silicon nanocrystals embedded in a silicon nitride matrix, three different deposition conditions for gold were studied. Gold monolayers were deposited by DC sputtering technique in Argon ambient on glass. The dimensions of the nanostructures were well controlled through the reader display screen of the equipment instead of time. The repeatability of the depositions was verified throughout different optical absorption spectra of the samples using the same conditions and SEM images. Silicon, glass and quartz substrates were cleaned following the cleaning steps of section 3.4.2 (big change on the morphology of these structures deposited on silicon or glass was not found). The gold thicknesses studied were:

Sample	Thickness (nm)
Au-A	1
Au-B	5
Au-C	10

Table (9) Thicknesses of the very thin films of gold deposited by sputtering.

It is worth mentioning that the thickness value was considered just a control parameter since the real morphology of these gold layers was unknown at this point.

Because silicon nanodots are deposited by the RPECVD technique at 300°C, it was necessary to study the morphological and optical properties of the metal structures undergoing this thermal treatment. In order to do this, the samples were cured in a conventional furnace for one hour in N₂ ambient.

5.2.1 Morphological and optical characterization

SEM images of the Au-B and Au-C samples deposited on glass, both as-grown and cured are shown in figures 40c, d and 40e, f respectively. Additionally, the figures 40a,b show the HRTEM and SEM images of the Au-A sample both deposited on silicon as-grown and after thermal treatment, respectively.

The samples with thickness of 5 nm and 10 nm (Au-B, Au-C) presented a high coalescence after thermal treatment. The 5 nm sample gave rise to particles of circular and ellipsoidal shapes surrounded by other smaller ones of the same shape. Moreover, the 10 nm gold deposition produced long worm-like shapes with increased distance between them (~15-70 nm) compared with the as-grown sample. HRTEM micrograph of the 1 nm thickness sample (Au-A) depicts particles of well-defined semispherical shapes and well distributed. It can be observed from the SEM image of this sample (figure 40b), that the size and distribution of these nanoparticles did not change considerably after thermal annealing.

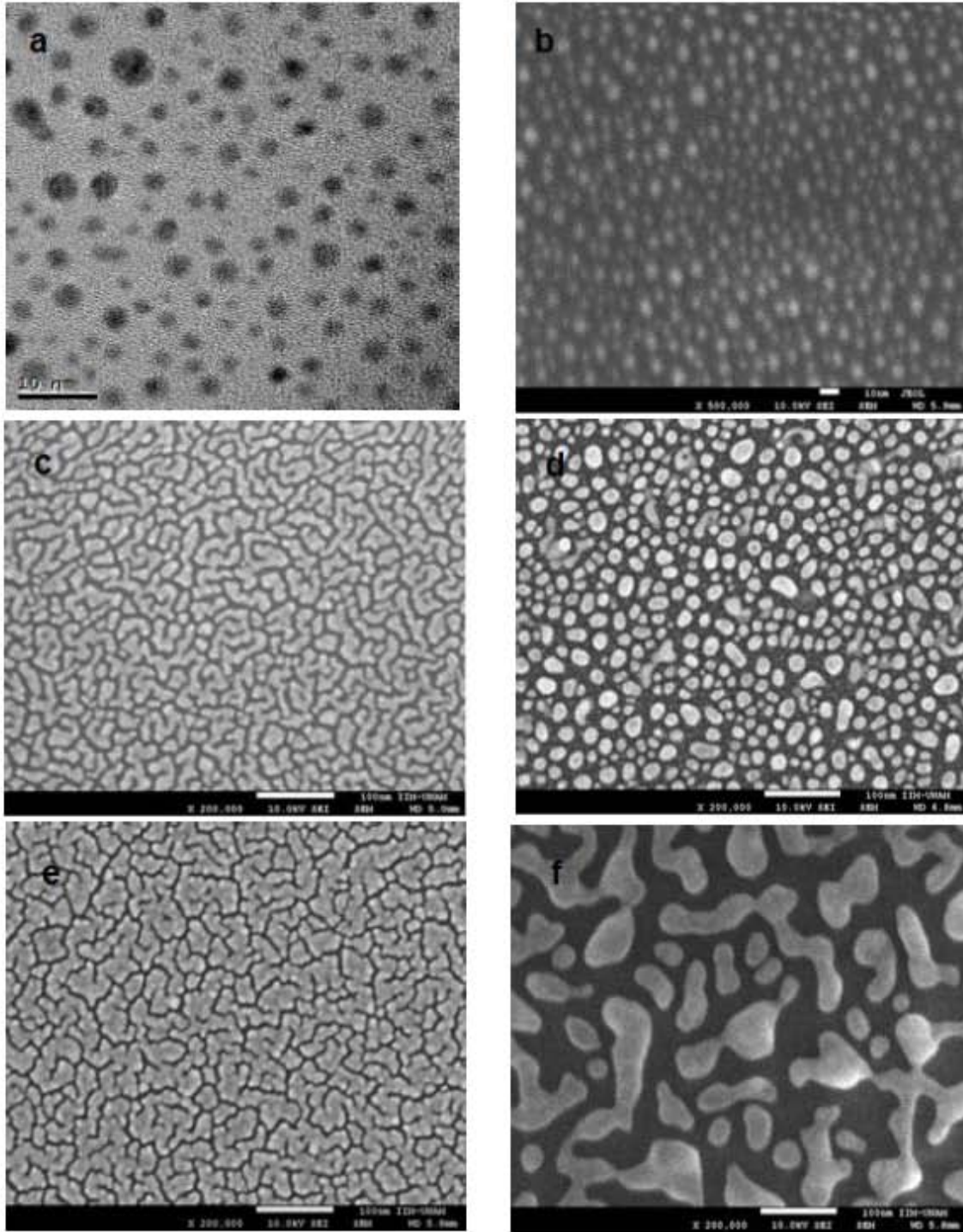


Figure (40) As-grown sample- Au-A deposited on silicon (40a) and SEM image of this sample after thermal treatment (40b). SEM images of the samples Au-B and Au-C deposited on glass both as-grown and cured are 40(c, d) and 40(e, f), respectively.

AFM images in topographic mode of the Au-B (left) and Au-C (right) samples after thermal treatments are shown in figure (41). The image of the Au-B sample (5 nm thickness) confirmed the coalescence of gold after thermal annealing to form particles. In addition, the morphology of the Au-C sample (10 nm thickness) showed long and broad islands. The average roughness of these

samples was 1.62 nm and 8.73 nm, respectively. Particles of the Au-A sample (1 nm thickness) could not be detected by this technique.

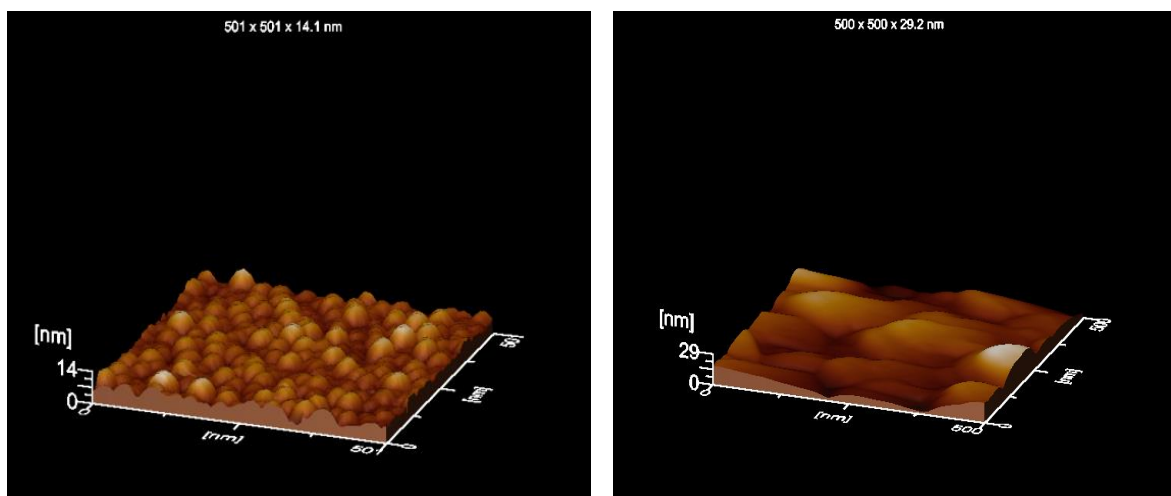


Figure (41) AFM images in topographic mode of the samples Au-B (left) and Au-C (right) after thermal treatment at 300°C in N₂ atmosphere.

Electrons in metals are quasi-free in the ground state. They can freely move through the crystalline structure of the metal since are not bound to a single atom. High conductivity and high optical reflectivity are two of the main properties of metals. When an electromagnetic wave with electric field $E(\mathbf{r}, \omega)$ interact with a metal, a dynamical polarization $P(\mathbf{r}, \omega)$ is created because of the electron cloud oscillates. $P(\mathbf{r}, \omega)$ expresses how far the electric field succeeds in displacing the electrons relative to the core atoms. Qualitatively, the electron cloud of the particle is entirely probed by the electric field if metal nanoparticles have sizes much smaller than the wavelength of light and the penetration depth of the field (i. e. particle size around 20 nm or less). Polarization of the whole assembly of electrons creates surface charges that accumulate alternately on opposite ends of the particle like a dipole. An electric field opposed to the excitation field is created by oscillating polarization of the particles and gives rise in a restoring force. Then, oscillation is partially damped. The damping occurs through two channels: creation of heat and light scattering. The whole system can be explained as a dipolar oscillator characterized by a resonance frequency ω_{plasmon} called Localized Surface Plasmon Resonance (LSPR). The plasmon resonance appears in the visible or near-infrared range for gold or silver nanoparticles. If a light beam travels through an assembly of homogeneous nanoparticles, this can be partially absorbed at the plasmon resonance frequency. The emerging beam will display a spectrum with a sharp absorption at ω_{plasmon} , and at the same time the nanoparticles exhibit light scattering with a cross section much larger than conventional dye. Moreover, LSPR strongly depends on the environment surrounded the particle surface [72]. The physical properties of metallic small nanoparticles and nanostructures are relevant to this work since some groups have studied the influence of LSPR in PL and EL enhancement [16-18, 73, 74].

In order to know the wavelength of optical absorption of the samples Au-A, Au-B and Au-C, their UV-vis spectra after cured at 300°C in air were obtained (figure 42). Surface plasmon resonance of Au-A sample was located at 525 nm. The Au-B sample showed red-shift absorption as well as a

more intense and broader peak at 551 nm. Finally, a wide absorption band was observed for the Au-C sample with a peak at 594 nm.

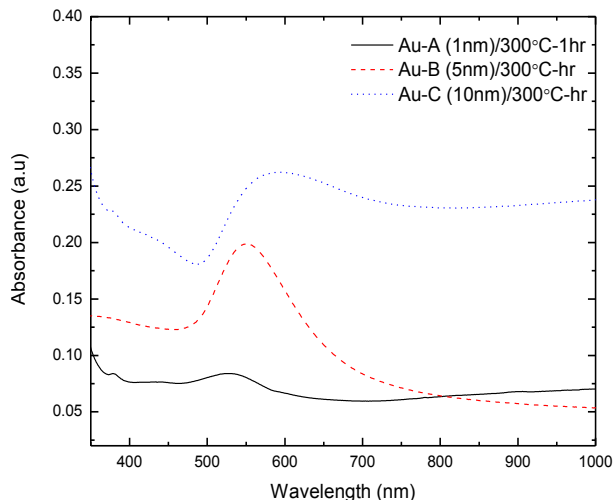


Figure (42) Absorbance spectra of samples Au-A, Au-B and Au-C cured at 300°C surrounded by air.

The statistical analysis of gold nanoparticles of sample Au-A was carried out through the counting of more than 1000 particles from HRTEM micrographs. The results obtained for this sample were: density (ρ) = 2.52E12 particles/cm² and diameter (d) = 2.9 nm (figure 43).

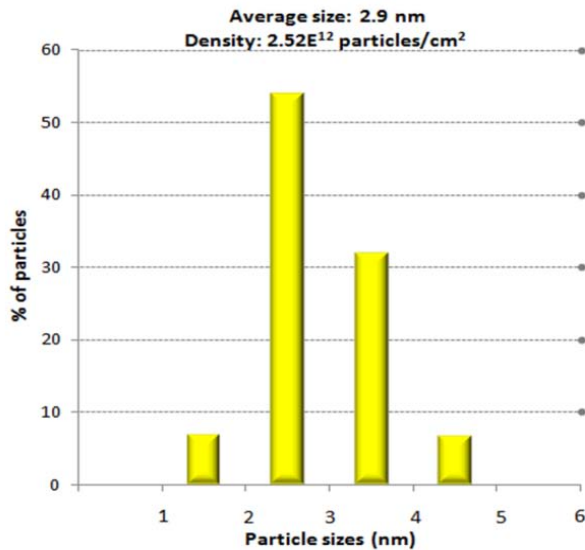


Figure (43) Histogram of the size distribution of nanoparticles in the sample Au-A.

The measurement of the particles of the Au-B sample was done from a SEM imagen. For the particles of semispherical shape the average diameter was $d = 12.63$ nm, and for the particles of elongated shape the average major axis was $l=21.12$ nm and the average minor axis was $s=13.28$ nm.

Moreover, the covered surface of gold nanoparticles was 18.12% for Au-A sample. For Au-B sample were considered circular and ellipsoidal areas resulting in a covered surface of ~65%

5.3 Coupling of SiQDs and Au nanostructures fields

Although at moment it is not well understood the kind of optical interaction that gives rise light enhancement from structures fabricated with silicon quantum dots in the vicinity of metal nanostructures, it has been observed that the distance achieved between these materials plays an essential role in the interaction of their electric fields and consequently in light emission. Taking this into account, it was proposed to use a non-radiative silicon nitride film (SiN_x) between the metal nanostructures and silicon quantum dots in order to get a well-defined and variable separation between them. In order to do this, the same RPECVD system could be used with different parameters to get chemically different thin films sequentially. The physical and chemical characteristics of these non-radiative layers have been studied in previous works [75], where it was proved that high ammonia flow rates (≥ 300 sccm) decrease the size and density of SiQDs in the films and consequently the integrated PL intensity. The parameters used to get this non-emissive silicon nitride film (SiN_x) by RPECVD system were:

NH ₃ Flow rate (sccm)	SiH ₂ Cl ₂ Flow rate (sccm)	H ₂ Flow rate (sccm)	Ar Flow rate (sccm)	Substrate temperature (° C)	Power of plasma (Watts)	Chamber pressure (mTorr)
600	5	20	75	300	150	300

To compare the optical characteristics of the layers grown with these parameters with those of SiQDs, two films of similar thickness were deposited using ammonia flow rates of 600 and 200 sccm. Silicon substrates underwent the conventional cleaning mentioned before. From Tauc plots the band gap of these samples were obtained. The SiN_x layer showed a gap close to the stoichiometric value of Si₃N₄ of 5. As expected, the band gap of the SiQDs layer was lower than that of SiN_x as it contains a higher content of silicon. Moreover, it has been studied that lower N/Si ratio result in increased number of silicon dangling bonds while high N/Si ratio will make the film more insulating [76] which is consistent with the band gap values obtained for these films. Also, because of refractive index of silicon is ~ 4 , the SiQDs film presented slightly higher refractive index than that of the SiN_x layer.

NH ₃ Flow	Sample	Thickness (nm)	Refractive index	Band gap (eV)
200 sccm	SiQDs (silicon rich)	97.9	1.84	4.04
600 sccm	SiN _x (nitride rich)	96.5	1.78	4.68

Table (10) Thickness, refractive index and optical band gap of the samples with 200 and 600 sccm NH₃ flow rate.

Fourier transform infrared spectra of these films are depicted in figure (44). The SiQDs film showed the typical Si-N (840cm^{-1}), N-H (1180 cm^{-1}), N-H (3350 cm^{-1}) and Si-H (2193 cm^{-1}) peaks. However, the Si-H bond was not observed in the SiN_x sample. This bond found in SiQDs layers can be ascribed to higher silicon concentration, then, additional silicon atoms can combine with hydrogen atoms to form Si-H bonds in the films. In this way two different types of silicon nitride layers could be deposited by RPECVD system: one silicon rich and another one nitride rich.

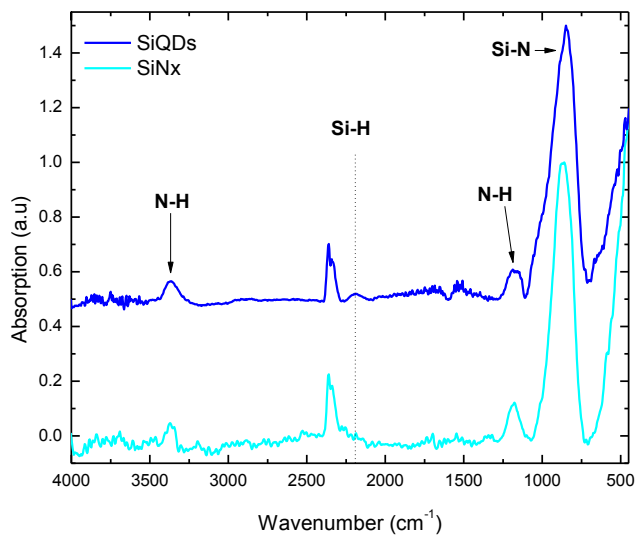


Figure (44) FTIR spectra of the SiQDs and SiNx films.

Photoluminescence spectra of these two chemically different films are shown in figure (45). The integrated PL intensity of the SiQDs film is 22 times higher than that of SiNx dielectric layer due to high density of silicon nanodots. Therefore, it could be proved that a flow rate of 600 sccm of ammonia gas as precursor produced non-radiative silicon nitride films.

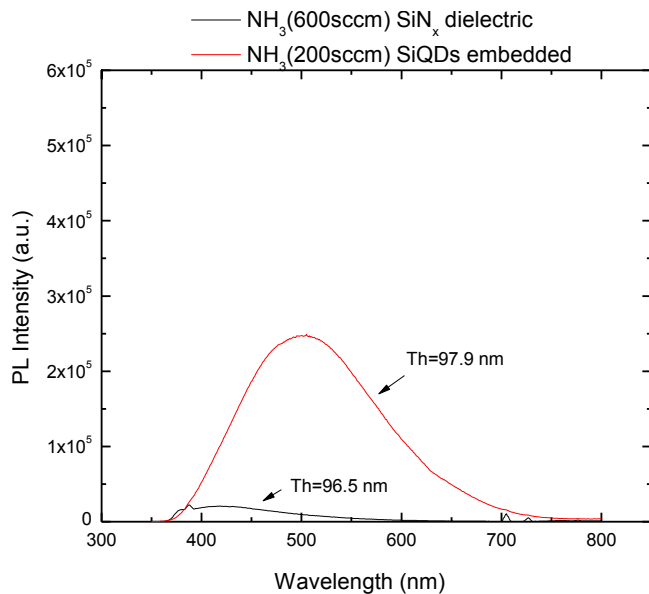


Figure (45) Comparison between emission spectra of SiQDs film (200 sccm of NH_3) and non-radiative film (600 sccm NH_3). Both films are about the same thickness.

According to [30, 31] a surface plasmon (SP) coupling should be within the exponentially decayed SP evanescent field. Since the SP is an evanescent wave that exponentially decays with distance from the metal surface, only electron-hole pairs located within the near-field of the surface can couple to the SP mode.

The penetration depth (ζ) of the SP NPs field into the insulating can be defined as:

$$\zeta = \frac{\lambda}{2\pi} \left[\frac{(\epsilon'_d - \epsilon'_m)}{(\epsilon'_d)^2} \right]$$

where ϵ'_d and ϵ'_m are the real parts of the dielectric and metal, respectively and λ is the wavelength of light [30]. Obtaining the real part of the dielectric constant of SiQDs film from its refractive index ($n=\sqrt{\epsilon_R}$) $\epsilon_R=3.38$, and considering the real part of the dielectric constant of gold as -7.6; by using the emission wavelength of SiQDs film at 505 nm, the penetration depth is 78.8 nm.

However, metallic behavior becomes size dependent and very thin layers fragment into clusters which have different optical properties than the bulk. Gold with effective thickness below 10 nm is usually not a continuous medium but has the topology of heterogeneous clusters with a connectivity that goes through a percolation transition [77]

Furthermore, Biteen et al. [16] obtained maximum PL enhancement from coupling of nanoporous gold and silicon nanocrystals implanted in a SiO₂ matrix when the interdistance between these materials varied. The distance between gold nanostructures and silicon nanoparticles for achieving maximum PL enhancement was ~10 nm.

Becoming acquainted with the aforementioned, SiN_x films of varying thickness sandwiched between Au nanostructures and SiQDs were deposited systematically. Deposits of 1 nm and 5 nm thickness of Au were chosen because of semispherical and bean like-shapes obtained.

5.3.1 Fabrication process steps

For each deposition condition was prepared a sample with gold and another one without it as a reference. Thickness of the chemically different silicon nitride films were controlled by time and supported by color table when possible. The cleaning procedure for silicon and quartz substrates was the same employed in section 3.4.2.

The processing steps used to fabricate the structures were:

1. Gold deposition by sputtering technique on one of the samples.
Thickness (Th): 1 or 5 nm
2. Deposition of the SiN_x film by RPECVD system.
Deposition time: 0, 30, 60, 90, 120 or 150 seconds.
3. Deposition of the silicon quantum dots embedded in a SiN_x:Cl matrix by RPECVD system.
Deposition time: 8 min 30 sec. Th: 90±5 nm

Sketches of the layered structures fabricated to investigate enhancement or quenching of photoluminescence are shown in figure (46).

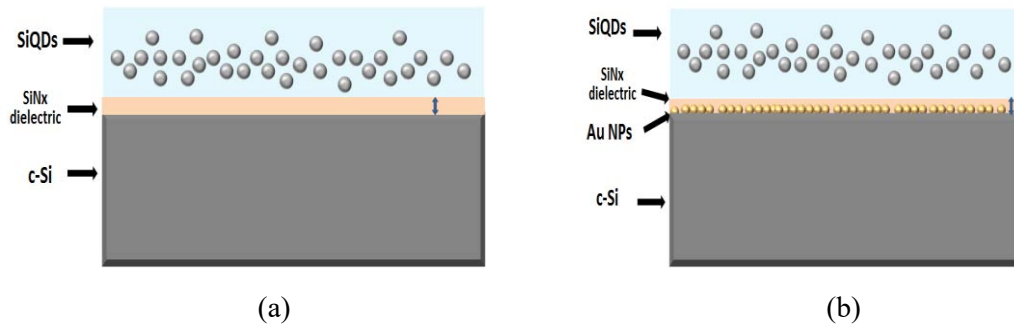


Figure (46) Layered structures (a) c-Si/SiNx/SiQDs and (b) c-Si/Au/SiNx/SiQDs.

A summary defining each sample and the corresponding deposition time for the different layers is presented in table (11).

Sample	Au thickness (nm)	Deposition time of SiNx layer	Deposition time of embedded SiQDs layer
D0		0	8 min 30seg
D0Au	1	0	8 min 30seg
D30		30	8 min 30seg
D30Au	1	30	8 min 30seg
D60		60	8 min 30seg
D60Au	1	60	8 min 30seg
D90		90	8 min 30seg
D90Au	1	90	8 min 30seg
D120		120	8 min 30seg
D120Au	1	120	8 min 30seg
D150		150	8 min 30seg
D150Au	1	150	8 min 30seg
E0		0	8 min 30seg
E0Au	5	0	8 min 30seg
E30		30	8 min 30seg
E30Au	5	30	8 min 30seg
E60		60	8 min 30seg
E60Au	5	60	8 min 30seg
E90		90	8 min 30seg
E90Au	5	90	8 min 30seg
E120		120	8 min 30seg
E120Au	5	120	8 min 30seg

Table (11) The samples prepared at different conditions.

5.3.2 Optical characterization

Absorbance spectra of the SiNx dielectric layer on quartz, AuNPs(1nm)/SiQDs and AuNPs(5nm)/SiQDs layered structures on glass are shown in figure (47). The SiNx dielectric is transparent for all SiQDs emission spectrum. Surface plasmon resonance of the layered structures with 1 nm and 5 nm thickness of AuNPs were red-shifted to 547 nm and 594 nm, respectively. The latter is in accordance with the fact that the surrounded medium plays a role in the plasmon resonance through its optical index n linked to the dielectric permittivity (the higher the optical index, the higher the plasmon resonance).

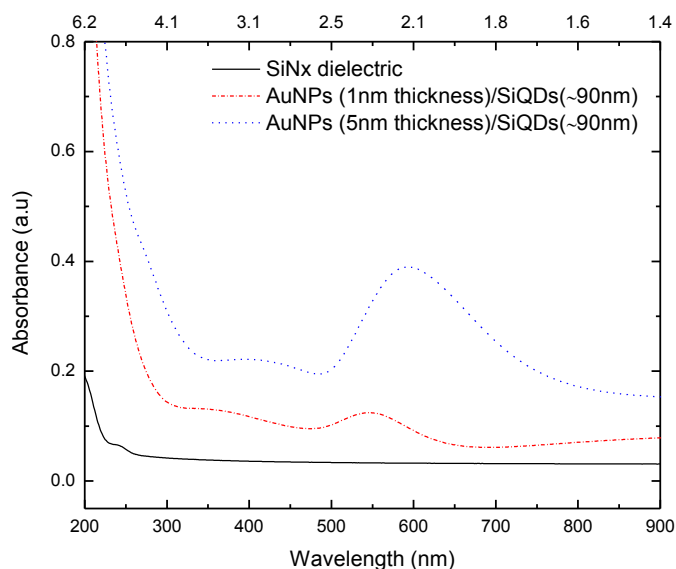


Figure (47) Absorbance spectra of the SiNx dielectric layer, AuNPs(1nm)/SiQDs and AuNPs(5nm)/SiQDs layered structures.

Photoluminescence measurements were obtained with a He-Cd laser of 325 nm at room temperature. PL spectra of samples with 1 nm thickness of gold nanoparticles and SiNx dielectric layer using deposition times of 0, 30, 60 and 90 sec before deposition of the active film are shown in figure (48). As can be observed from the figure, at 0 sec of the SiNx layer, the sample with AuNPs and its reference did not show any change in PL intensity and peak shift. The sample D30Au (deposition time of 30 sec for the SiNx layer between AuNPs and SiQDs) showed slightly PL enhancement and red shift with regard to its reference. When the SiNx layer was grown 60 sec (corresponding to a thickness of ~10 nm) it was found an almost 2-fold PL intensity enhancement from the coupled structure with respect to its reference one and also slight red shift. Samples with 90 sec of the SiNx layer (figure 48d) showed very close PL intensity and no red shift was observed from the sample with AuNPs. Finally, the samples D120Au and D150Au had similar behavior as they did not present significant enhancement, quenching or peak shift with regard to their references.

As it was mentioned before, other research groups have studied luminescence of metal-SiQDs structures as their separation distance get closer. They showed a Gaussian type PL enhancement

ratio relative to their reference. This latter is not just an effect of bringing closer different material nanoparticles, but probably an effect of different particle density distribution through determined distances. Consequently, it was difficult to define a maximum PL enhancement for a defined density concentration and separation distance among metal nanoparticles and silicon nanocrystals. In our experiment the homogeneous distribution achieved of the metallic monolayer and SiQDs radiative film let us to identify clearly that there is a well specific separation distance between the AuNPs/SiQDs to attain maximum light enhancement from the system. It is worth mentioning that methodical reproduction of the experiment confirmed 10 ± 2 nm of SiNx thickness in our structures in order to achieve maximum light enhancement.

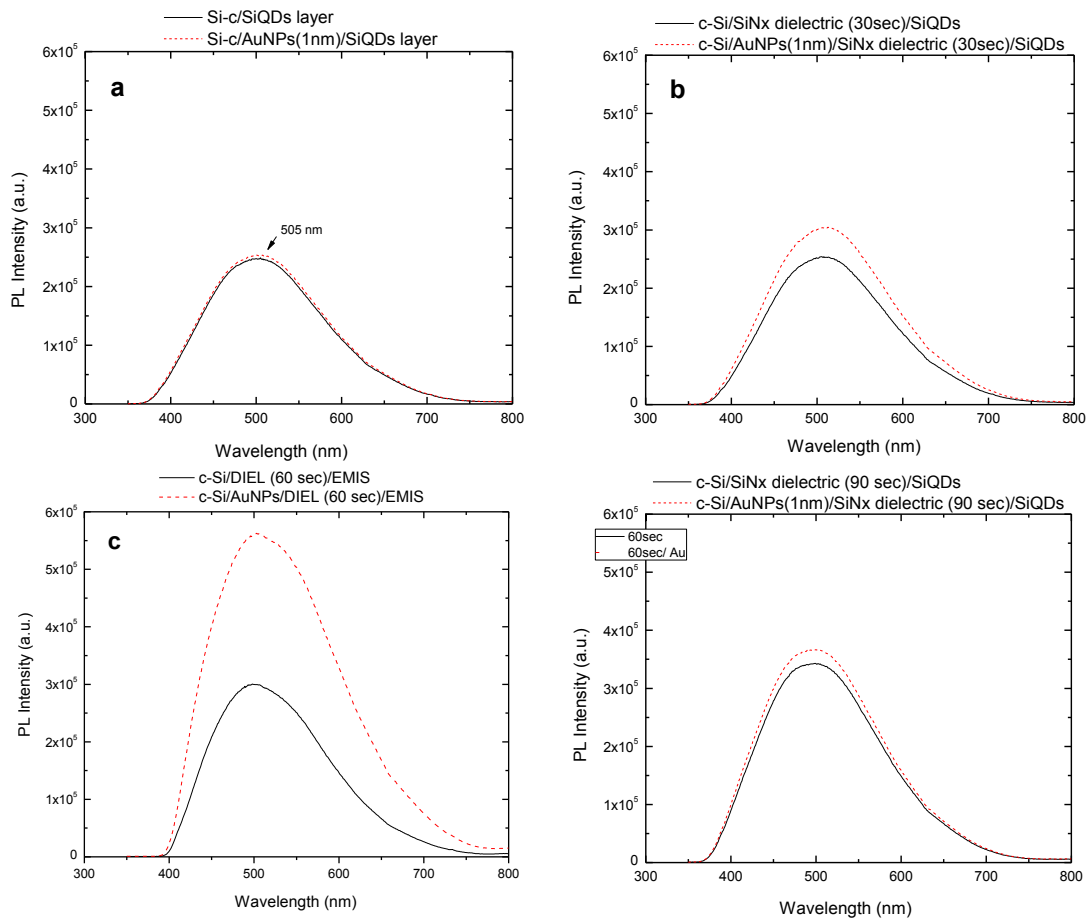


Figure (48) Four different configurations of the proposed structures using SiNx layers of 0, 30, 60 and 90 seconds. Deposition time was adjusted to obtain thickness of the SiQDs films of ~ 90 nm. For each configuration there was one sample used as reference without AuNPs deposited on the silicon substrate for comparative purposes.

Furthermore, the same structure was proved with AuNPs of 5 nm thickness using deposition times of 0, 30, 60, 90 and 120 sec for growing the SiNx film before the SiQDs layer. No enhancement or quenching of PL intensity was observed for each deposition time of the SiNx dielectric layer from the samples with AuNPs with respect to their references, although in all cases was found slight red shift. The PL spectra of four of these structures are shown in figure (49).

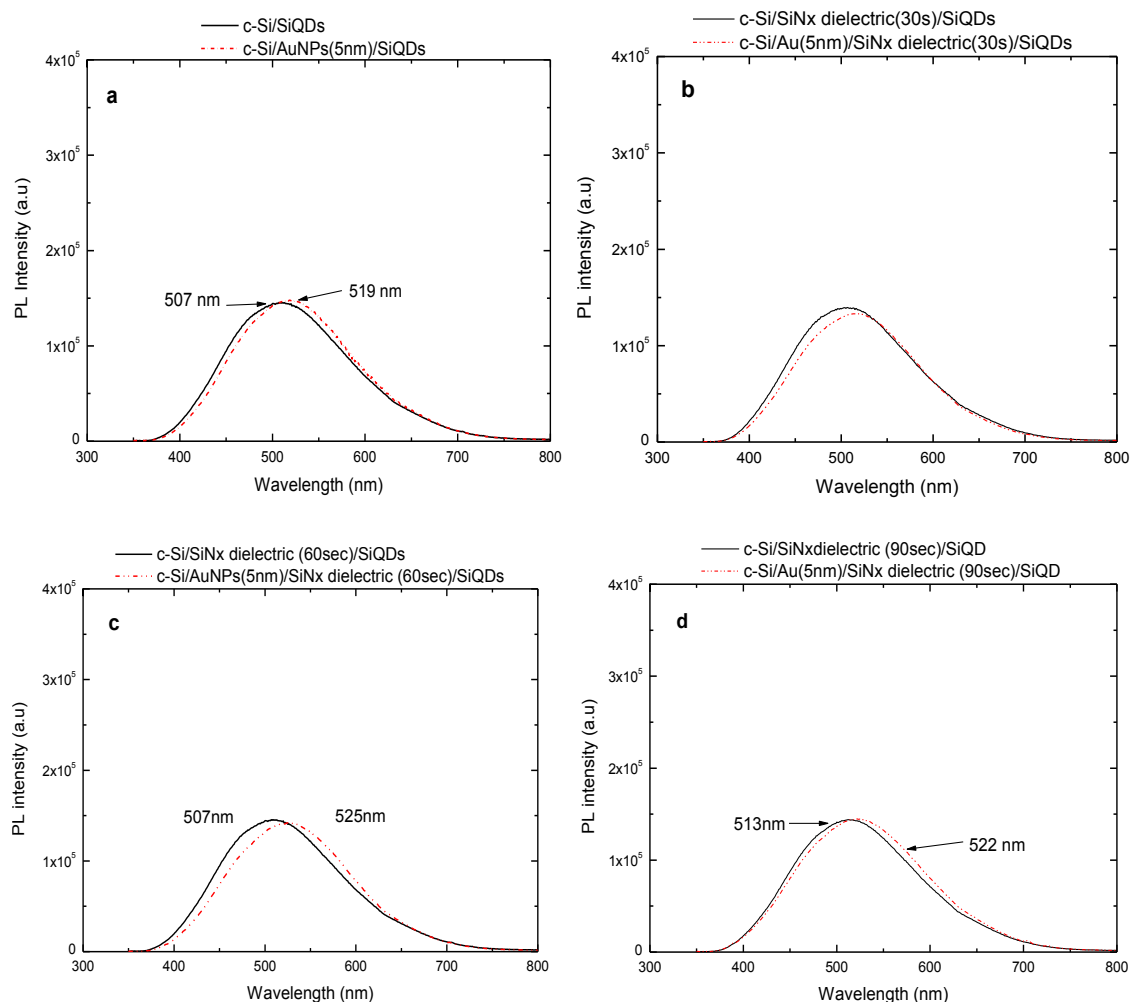


Figure (49) Comparative spectra of samples prepared for 0, 30, 60, 90 and 120 sec of SiNx dielectric layer sandwiched between the AuNPs of 5 nm thickness and SiQDs.

Integrated PL intensity ratio of the samples with 1 and 5 nm gold thicknesses with respect to their references is depicted in figure (50). As can be seen, for 60 sec of the SiNx layer (10 ± 2 nm) between AuNPs of 1 nm thickness (2.9 nm diameter) and the SiQDs film was found the highest integrated PL intensity ratio of 2.1. On the other hand, integrated PL intensity ratio of the samples with AuNPs of 5 nm thickness was practically constant for any deposition time of the SiNx dielectric layer.

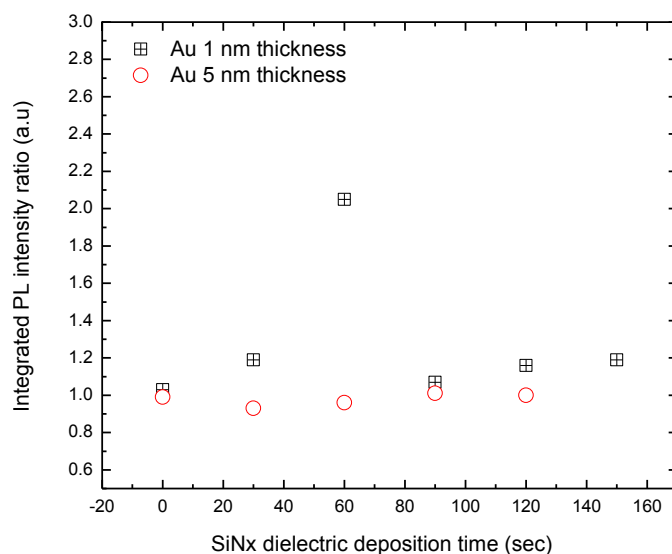


Figure (50) Integrated PL intensity ratio of the samples with 1 and 5 nm gold thicknesses with respect to their references.

5.4 Conclusions

In this chapter the dependence of the emission efficiency was studied systematically in multilayered structures as a function of the size of gold AuNPs and the distance between gold nanostructures and silicon quantum dots.

Maximum enhancement of photoluminescence was observed in the structure with gold nanoparticles of average size of 2.9 nm (1 nm thickness) separated from the active film about 10 nm. These particles could not be detected with a high resolution cantilever by AFM. The efficiency found could be originated by a change of the scattering mechanisms of the primary light or the emission from luminescent centers by the presence of gold nanoparticles. Another possible explanation of this enhancement is by coupling of the emission from SiQDs and the absorption of small metal nanoparticles (localized surface plasmon resonance). The latter reason may be possible as emission of SiQDs (505 nm) was found close to the absorption peak of gold nanoparticles of 2.9 nm size (547 nm).

Moreover, it was not observed any enhancement or quenching in the layered structures with 5 nm thickness AuNPs using different interdistances of the SiNx film but slight red-shift.

CHAPTER VI. Metal-insulator-semiconductor devices

Until now, the power efficiency of SiQDs light emitting diodes (LEDs) is very low and therefore it is difficult for them to fulfil the demands of optical interconnections. In order to overcome this deficiency some groups have studied increased radiative recombination rate by coupling excitons to localized surface plasmons in metal nanostructures. Other groups have sought to improve the EL extraction efficiency increasing the flow of light emitted from the active layer by the modification of the surface morphology.

Considering the above, it was proposed to manufacture light emission devices using some of these configurations. Thus, in this section the electrical and optical properties of metal-insulating-semiconductor (MIS) based devices were studied to investigate the behavior of the most efficient multilayered structures previously fabricated in chapter V when they were electrically excited.

6.1 Metal-insulator-semiconductor capacitors

For the study of semiconductor surfaces the metal-insulator-semiconductor (MIS) capacitor is the most useful device since most practical problems in the reliability and stability of all semiconductor devices are deeply related to their surface conditions. Likewise, metal-oxide-semiconductor (MOS) capacitor case is directly related to most silicon planar devices and integrated circuits. The MOS capacitor (fig. 51) is made of a semiconductor body or substrate, an insulator film, and a metal electrode entitled a gate. The silicon dioxide as insulator can be as thin as 1.5 nm. The metal-oxide-structure is part of the MOS transistor which is the most widely used semiconductor device. An MOS capacitor with two PN junctions flanking the capacitor is the MOS transistor.

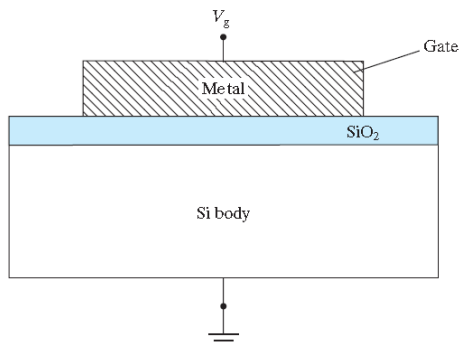


Figure (51) Scheme of a MOS capacitor.

In an apparently simple MOS structure the surface effects that arise are actually quite complicated. Those effects which control typical MOS transistor operation are accumulation, depletion and inversion depending on the gate voltage applied to the device (see Appendix A).

Additionally, the equilibrium MOS structure is affected by charges in the insulator and at the semiconductor-oxide interface. Alkali metal ions (particularly Na⁺) can be incorporated inadvertently in the oxide during growth or subsequent processing steps. Sodium ions introduce

positive charges (Q_m) in the oxide, which in turn induce negative charges in the semiconductor. The number of ions involved and their distance from the semiconductor surface determine the effect of such positive ionic charges in the oxide. As expected, the negative charge induced in the semiconductor is greater if the Na^+ ions are near the interface than if they are farther away. In the case of SiO_2 , trapped charges (Q_0) also exist due to imperfections. In addition to oxide charges, a set of positive charges arises from *interface states* at the Si-SiO₂ interface. These charges called Q_{it} result from the sudden termination of the semiconductor crystal lattice at the oxide interface. There is a transition layer (SiO_x) containing fixed charges (Q_f) near the interface. This charge depends on issues as oxidation rate, subsequent heat treatment, and also on crystal orientation. These type of charges can affect some important parameters in a device as current injection, threshold and breakdown voltage. Then, in order to build an efficient MOS device it is desirable to keep as low as possible the number of these charges [78].

6.2 First stage of fabrication of metal-insulator-semiconductor devices based on SiQDs

The fabrication of metal insulating semiconductor devices (MIS) in this chapter had the aim of studying the electroluminescence of the most important configurations engineered in the previous section. Two main issues were worth noting to try to understand:

- a) The effect on injected current and electroluminescence of a very thin film of silicon nitride (SiN_x) dielectric layer (10 nm thickness) grown by using 600 sccm flow rate of ammonia.
- b) The effect on injected current and electroluminescence of AuNPs (2.9 nm diameter) compared with reference samples without gold, with the aim to observe enhancement or quenching of light emission.

In order to accomplish this task, two different processes named P1 and P2 were carried out. Each process used a reference sample to compare the electrical properties. The layered structures are summarized as follows:

Process 1:

PR1) c-Si/SiQDs/ZnO:Al

P1) c-Si/AuNPs(1nm thickness)/SiQDs/ZnO:Al

Process 2:

PR2) c-Si/ SiN_x dielectric(10nm)/SiQDs/ZnO:Al

P2) c-Si/AuNPs(1nm thickness)/ SiN_x dielectric(10nm)/SiQDs/ZnO:Al

6.2.1 Fabrication process steps

Quartz and p-type crystalline silicon of $1 \times 1 \text{ cm}^2$ were used as substrates. Some authors have reported the use of p-type silicon substrates since the Si/SiN_x valence band offset (1.9 eV) is smaller than the conduction band offset (2.1 eV) [66]. Then, the hole conduction is regarded as the main conducting mechanism in silicon nitride. For these devices, the ZnO:Al metal oxide was used as the top transparent conductive contact deposited using the same parameters of section 2.1.3. Therefore, the fabrication process steps were:

- Standard silicon wafer cleaning (Solvent clean, RCA I and RCA II). Cleaning of quartz was the same employed in section 3.4.2.
- Gold deposition by sputtering technique.
 - Thickness (Th): 1 nm
- Deposition of the silicon nitride (SiN_x) dielectric film by RPECVD system.
 - Deposition time: 60 sec. Thickness: 10 ± 2 nm
- Deposition of SiQDs embedded in a SiN_x:Cl matrix by RPECVD system.
 - Thickness (Th): 80 ± 5 nm
- Deposition of ZnO:Al by ultrasonic spray pyrolysis as the TCC.
 - Thickness (Th): 1 ± 0.2 μm
- Deposition of aluminum on the back of the sample by thermal evaporation.
 - Thickness: 100 ± 10 nm

After the process was completed, the samples were cleaved into pieces of 2×2 mm by means of a pattern. It is worth mentioning that just $\sim 30\%$ of the devices in each sample had a diode like behavior. The rest of the devices presented high leakage current, which were those probably located on the edge of the samples where higher amount of defects are found. Despite the above it can be said that the reproducibility of the functional structures was proved as the electrical and optical properties of some of the samples fabricated afterwards were very similar. The schemes of the four layered structures are depicted in figure (52). Additionally, the SEM images of the cross section of the PR2 and P2 samples are shown in figure (53); a line separating the SiN_x and SiQDs layers was not observed by this technique.

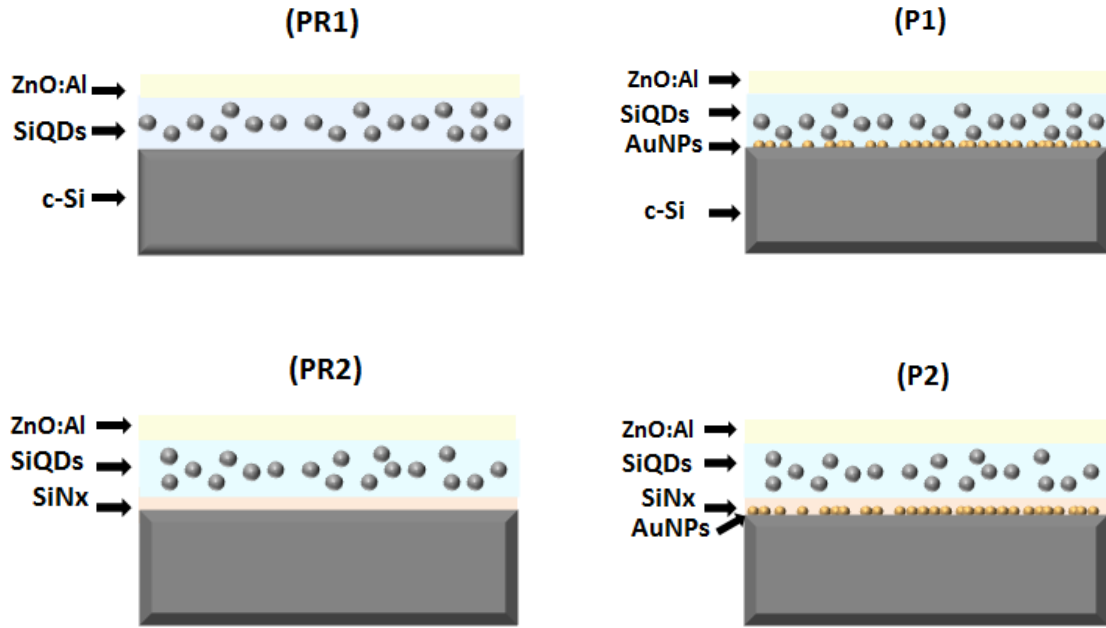


Figure (52) Electroluminescent structures used to prove the effect of AuNPs (2.9 nm) and the 10 nm thickness SiNx dielectric layer (images are not in scale).

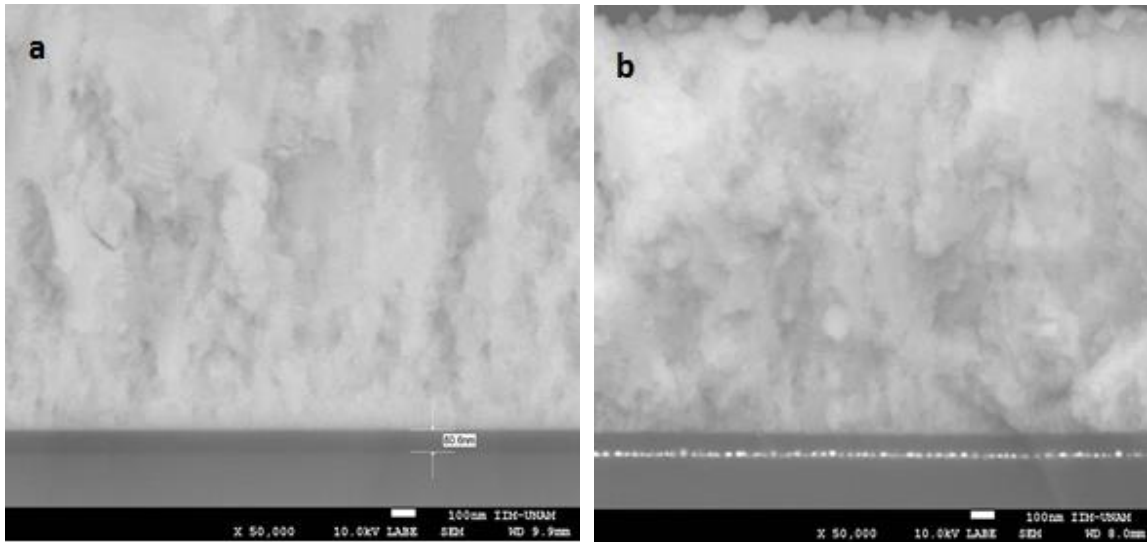


Figure (53) SEM images of the PR2 (a) and P2 (b) samples. The thin SiNx layer in these samples was not detected by this technique.

6.2.2 Optical and electrical characterization

The optical and electrical measurements of the light emission devices were carried out using the measurement set up of section 2.2.9. Forward bias was considered when the cathode electrode was on the ZnO:Al (Fig. 54). These structures also undergo an electrical annealing in forward and reverse bias in order to create conductive paths through the dielectric.

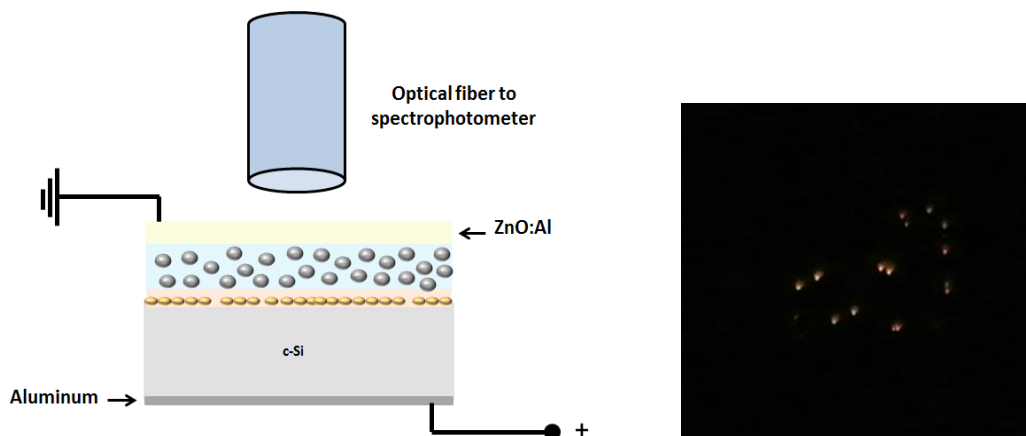


Figure (54) Forward bias connection of the MIS structures and EL emission imagen of the P2 sample.

From each sample (PR1, P1, PR2, and P2) the three devices with best performance were chosen, i.e. those possessing the highest intensity during the bias voltage ramping. Afterwards, another selection was made in order to get only one device from each sample. The electroluminescence spectra measured in a dark room at room temperature of the four chosen devices at different voltages are shown in the figure (55).

All the samples showed broad electroluminescent emission only in forward bias at room temperature with the maximum intensity peak centered at around 600 nm. The peak position for samples PR1, PR2 and P2 remained at the same wavelength when different voltages were applied; on the other hand the peak position of the sample P1 had a slight red-shift. As can be seen for samples PR1 and P1 without the SiN_x layer, the EL turn on voltages were 18V and 14V, respectively, lower for the sample with AuNPs. In these samples voltage steps of 2V were required to observe increased intensity in the emission curves. For the samples PR2 and P2 with the thin SiN_x layer, the EL turn on voltages were 14V and 11V, respectively. The EL spectra of the PR2 sample were obtained using voltage steps of 2V, whereas for the P2 sample (also with gold nanoparticles) a well-defined growth in intensity was observed when applied 1V steps. Therefore, the samples P1 and P2 with gold nanoparticles showed lower EL turn on voltages with regard to their references as well as higher emission increments under applied voltages.

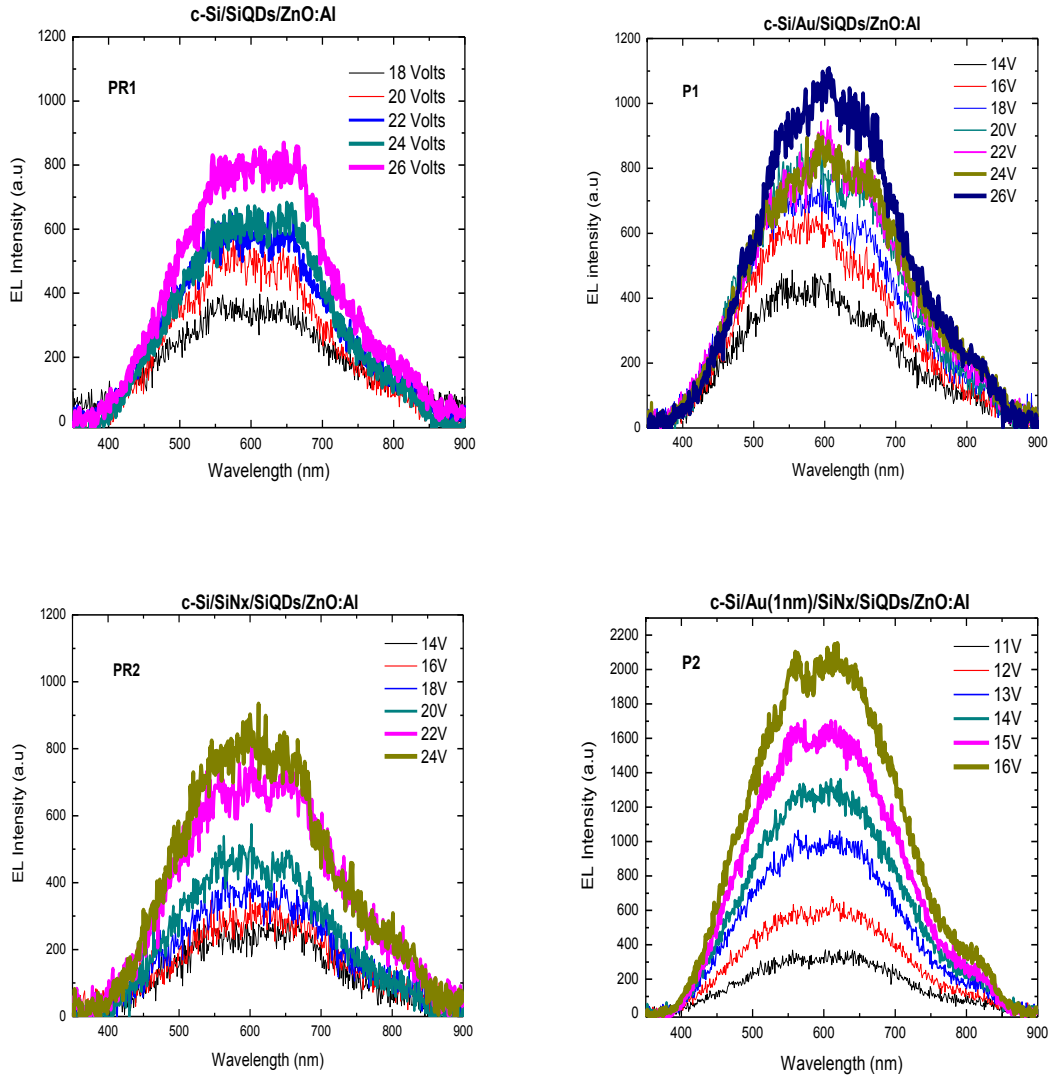


Figure (55) Electroluminescence spectra of samples P1, P2, PR1, and PR2 in forward bias.

In order to investigate the origin of the observed EL spectra and EL turn on voltages, a plot of the integrated electroluminescence intensity against injected current of each sample is shown in figure (56). At first glance the PR1 and P1 samples without the SiNx layer showed very similar trend for the integrated EL intensity. However, it can be observed that the plotted points of the P1 sample with AuNPs corresponding to applied voltages from 14V to 26V indicated higher current injection as well as higher integrated EL intensity compared with the corresponding points from 18V to 26V of the PR1 sample. Gold nanoparticles could enhance luminescence intensity in the P1 sample due to increased injection of electrons and holes to the conduction and valence bands in the silicon nitride matrix, respectively. Even though the morphology of gold nanoparticles deposited on silicon was not distinguished by AFM and the roughness of this monolayer was very low (see appendix B), the electric field could increase at AuNPs location and influence a conduction mechanism of carriers as tunneling [60, 69].

Likewise, for the PR2 and P2 samples also with the very thin SiNx layer the behavior of the integrated electroluminescence vs. current injected was linear being the slope of the P2 sample (with AuNPs) higher than that of PR2. Although the current was about the same in both samples at 14V, the integrated EL intensity in sample P2 was 4.6 times higher than in sample PR2 which denoted improved carrier injection to the luminescent centers. From this applied voltage, the growth of EL intensity as well as current injected in the P2 sample was greater.

The EL enhancement observed for these devices with and without gold nanoparticles as a function of the electric field is plotted in figure (57). The EL enhancement is defined as the ratio of integrated EL intensities of samples with AuNPs (P1 and P2) and reference samples (PR1 and PR2) when the same electric field is applied. A maximum EL enhancement of 1.79 was found at 2.25 MV/cm for samples PR1 and P1, and decreased as higher electric fields were applied. The EL enhancement of samples PR2 and P2, with only two comparative points, raised when increasing the electric field and had a maximum ratio of 5.94 at 2MV/cm.

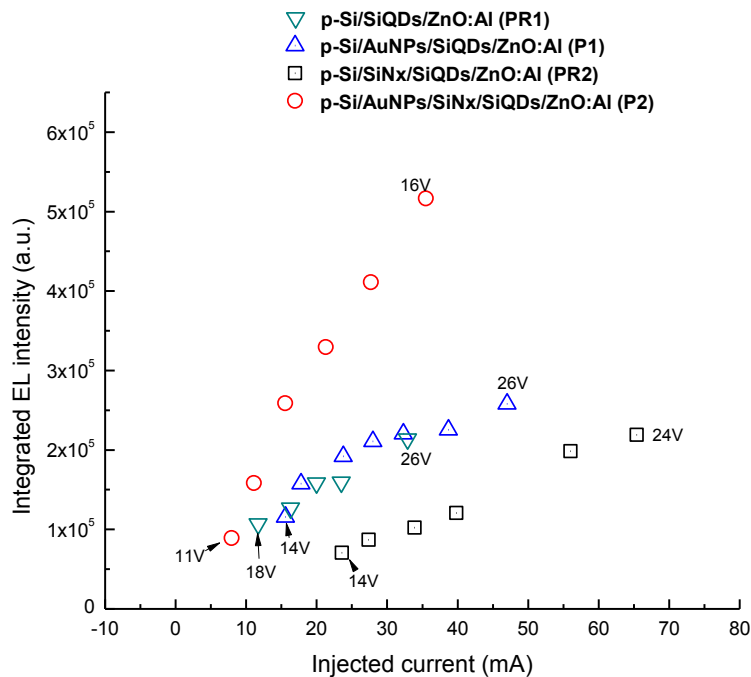


Figure (56) Integrated electroluminescence intensity vs injected current of the P1, P2, PR1 and PR2 samples.

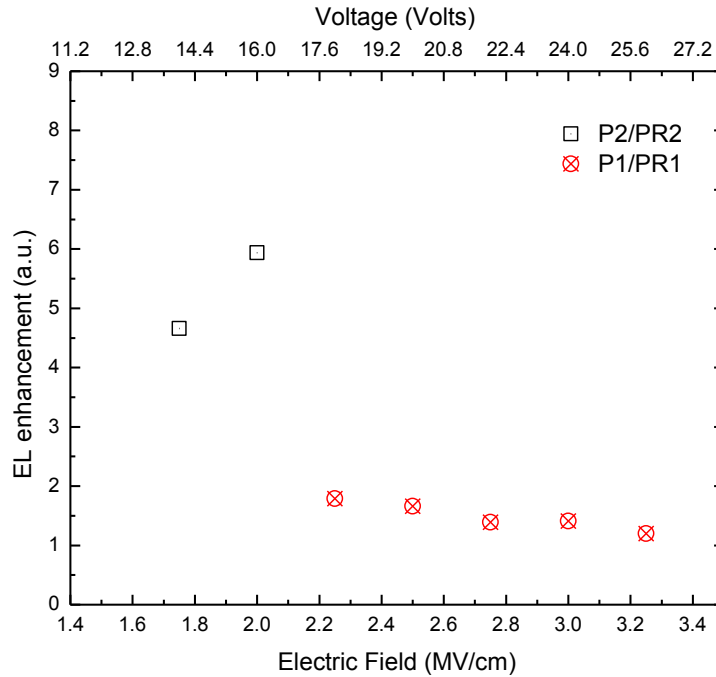


Figure (57) EL enhancement of the fabricated LEDs.

The current density vs. electric field of samples PR1, P1, PR2, and P2 are plotted in figures (58a) and (58b). Lower threshold voltage and higher current density injection was observed in the P1 sample with AuNPs than in the sample PR1 in forward bias. On the other hand, the P2 sample showed higher threshold voltage and higher current density from 2MV/cm than the reference sample PR2 in forward bias. However, the PR2 sample presented slightly higher current density at low electric fields (~ 0 -2MV) than P2 sample. Additionally, the current density in reverse bias was very low up to ~ 3 MV/cm for samples with gold nanoparticles (P1 and P2), meanwhile it did not show any increment for the PR1 sample in all the measured range. The sample PR2, with the thin SiNx layer, presented increased current density in reverse bias from 0.5MV/cm; however, it was not detected radiative emission from this sample probably due to reduced carrier transport and inefficient radiative recombination when compared with forward bias. Therefore, the increase in carrier injection in the P1 and P2 samples (when positive polarization is applied) with respect to their references could be attributed to the presence of AuNPs which enhanced the inhomogeneous local electric field at the interface between silicon substrate and the dielectric film [60]. This higher carrier density injected to the bulk accounts for the improved electroluminescence intensity before observed.

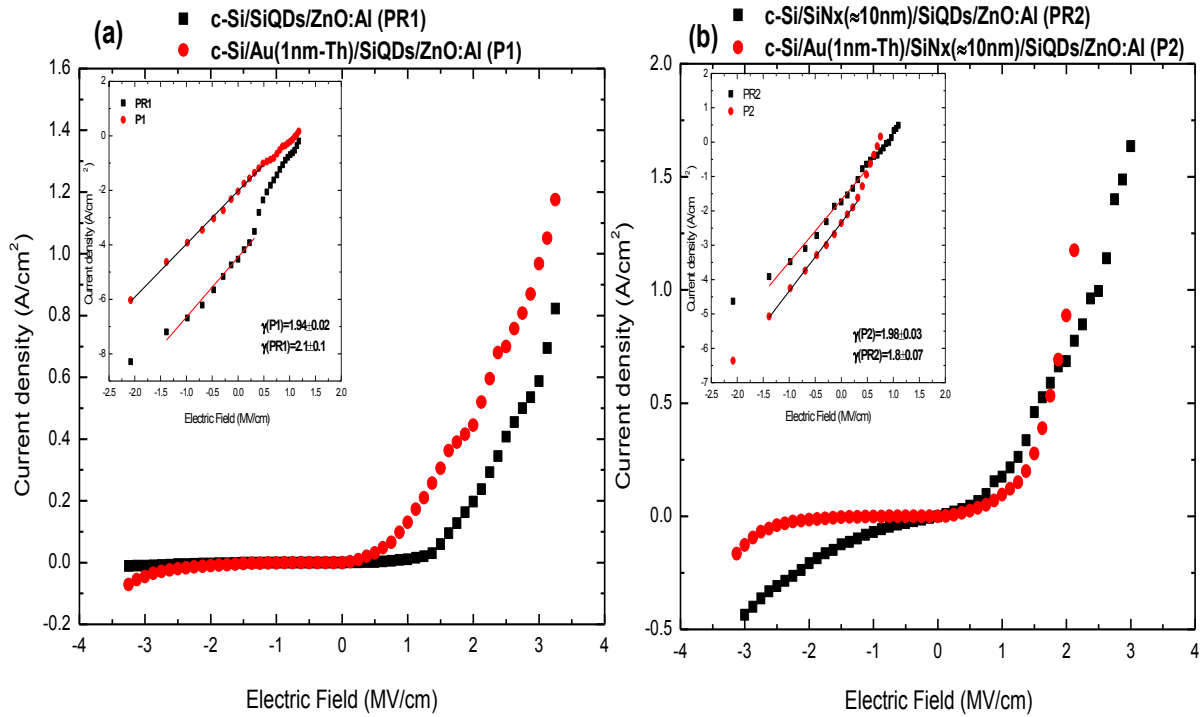


Figure (58) Current density-Electric field plots of the fabricated electroluminescent devices PR1, P1 (a), and PR2, P2 (b).

With the aim to recognize the electric field regions of these curves, its log-log plots are shown in the inset of figures (58a) and (58b). The fitting at low electric fields of all the samples gave rise to a slope γ close to 2, indicating a space charge limited current mechanism in which the current is dominated by charge carriers injected from the electrodes.

To further understand the role of gold nanoparticles and the thin SiNx in the fabricated samples, the current-voltage plots for three different devices of each structure are shown in figure (59). A double asterisk denotes the samples PR1, P1, PR2, P2. It can be noticed a repetitive behavior in those devices with AuNPs in forward and reverse bias, which suggests that these particles could help to constraint and/or distribute carriers at the c-Si/dielectric interface. The latter behavior was not observed in samples without metal nanoparticles where different threshold voltages were observed. Additionally, the reference devices with the SiNx layer (c-Si/SiNx/SiQDs/ZnO:Al) showed slightly higher currents under application of low positive voltage (ranging from ~ 0 -7 Volts) compared with those observed in the devices of the other structures.

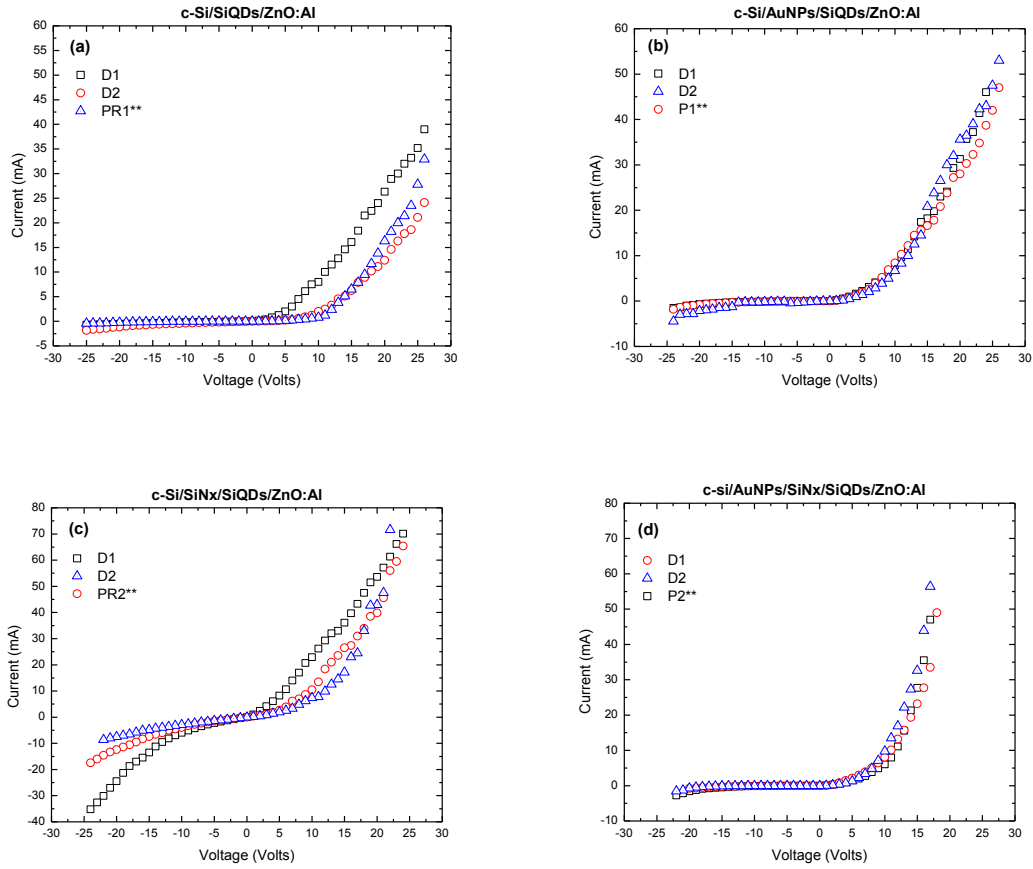


Figure (59) Current-voltage plots for three different devices of each fabricated structure.

Since the thin SiN_x layer (10±2 nm thickness) is nitrogen rich, its band gap is higher than that of the SiQDs layer as revealed Tauc plots (4.68 eV and 4.04 eV respectively). Thus, a higher electric field may be present in the SiN_x layer than in the SiQDs film of the PR2 sample. From other point of view, the total capacitance of the PR2 layered structure might be considered as the combination of the capacitances of the silicon substrate (C_{Si}), the SiN_x film (C_{SiN_x}) and the SiQDs film (C_{SiQDs}) in series, where the C_{SiQDs} is the sum of the capacitances of silicon nanocrystals (C_{Si-nc}) and the dielectric where they are embedded (C_{diel}) [11]. The equivalent circuit at equilibrium (without applied voltage) is shown in figure (60).

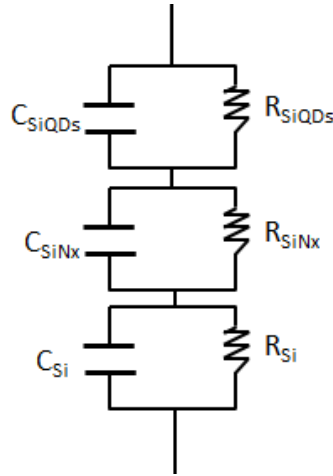


Figure (60) Equivalent circuit without applied voltage for the PR2 sample.

When the device is in accumulation region under forward bias, $C_{Si} \gg C_{SiNx}$ and C_{SiQDs} . Moreover, since the thickness of the SiNx film is lower than that of the SiQDs film $C_{SiNx} > C_{SiQDs}$. The latter is obtained from the capacitance in a parallel plate capacitor $C = \epsilon_0 \epsilon_r A/d$, where ϵ_0 and ϵ_r are the vacuum and relative permittivity, respectively, A is the surface area and d is the distance between the plates (a roughness estimation of the real part of the relative permittivity can be found from $n = (\epsilon_r)^{1/2}$). Then, $C_{SiNx} > C_{SiQDs}$ indicates that a higher charge density may be found in the c-Si/SiNx interface of the PR2 sample than in the c-Si/SiQDs interface of the PR1 reference sample without the SiNx layer, because the charge in the surface of the semiconductor for an ideal MIS capacitor is $Q_s = C_d V_d$ where Q_s =surface charge (coulombs), C_d =capacitance (Farads) and V_d =Volts (V).

For an ideal MIS capacitor the charge in the surface of the substrate should be compensated by the charge in the metal gate; however, for the real case of the PR2 sample non-idealities must be considered like different work functions of metal and semiconductor and interface states among others. As a result, the charge could not be compensated in the metal gate and carriers can be more easily injected from the c-Si/SiNx interface even at low electric fields to the bulk of the insulating. It has been reported that a local onset of the leakage current depends on the electric field strength [60]. This effect of increased current density injection to the insulating at low electric fields ($\sim 0.1.4$ MV/cm) in the PR2 sample seemed to be well hindered by gold nanoparticles in the P2 sample. When increased the electric field the current density of the P2 sample with AuNPs was higher than that of PR2.

Therefore, because of the observed in the samples with noble metal nanoparticles, lower threshold voltage observed in the P1 sample with regard to the P2 sample could be due to the presence of silicon nanodots at the c-Si/SiQDs interface allowing direct tunneling between Si islands [79] and/or silicon dangling bonds conduction paths [76]. On the other hand, this effect is reduced in the P2 sample with the SiNx dielectric due to the very lower density of silicon nanodots and silicon dangling bonds at the c-Si/SiNx interface. In both cases, AuNPs may homogenize the electric field at the interface at the same time that improve the injected current.

The F-N, P-F and TAT conduction mechanisms were fitted to the current-voltage data of the PR1, P1, PR2 and P2 samples at higher electric fields (~1.5-3 MV/cm). P-F mechanism was the best fitting for samples P1, P2 and PR2 (see Appendix B). For the PR1 sample TAT mechanism fitted better its curve. This mechanism could be dominant in this sample since it is well known that silicon rich silicon nitride films give rise to a higher number of silicon dangling bonds which can form conductive paths when the number of dangling bonds is high enough [11, 76]. Therefore, silicon nanodots growing from the first atomic layers on the substrate in addition with dangling bonds may have an important role for the current conduction to the bulk as carriers could flow to silicon nanocrystals through Si dangling bonds or direct tunneling.

The injected current efficiency in quantum-well lasers is described as the fraction of the injected current that recombines, both radiatively and non-radiatively, in the quantum well active region of the laser. The injected current efficiency is different from the internal quantum efficiency (η_{rad}), as the internal efficiency is defined as the fraction of the injected current that recombines radiatively in the quantum well active region [80].

External quantum efficiency is the ratio of the number of photons emitted and the number of electrons passing through the LED. Explicitly, it is the product of the *internal quantum efficiency* (radiative efficiency), η_{rad} ; *injection efficiency*, η_{inj} ; and *optical efficiency* (light extraction efficiency), η_{opt} :

$$\eta_{ext} = \eta_{inj} * \eta_{rad} * \eta_{opt}$$

It is possible to compare the EL efficiency of the samples indirectly by dividing the absolute integrated EL intensity to the injected current [17]. The EL efficiency of samples P1, PR1, P2 and PR2 are shown in figure (61). Efficiency in PR1 and P1 samples decreased as current injection increased. This may indicate a reduction of the current efficiency transport and whose origin in high power nitride LEDs could be: 1) carrier leakage, 2) large Auger recombination at high carrier density and 3) junction heating [81]. For the PR2 sample, the EL efficiency was the lowest and constant under all injected currents. The P2 sample depicted the highest EL efficiency increasing up to a maximum after which it diminished gradually.

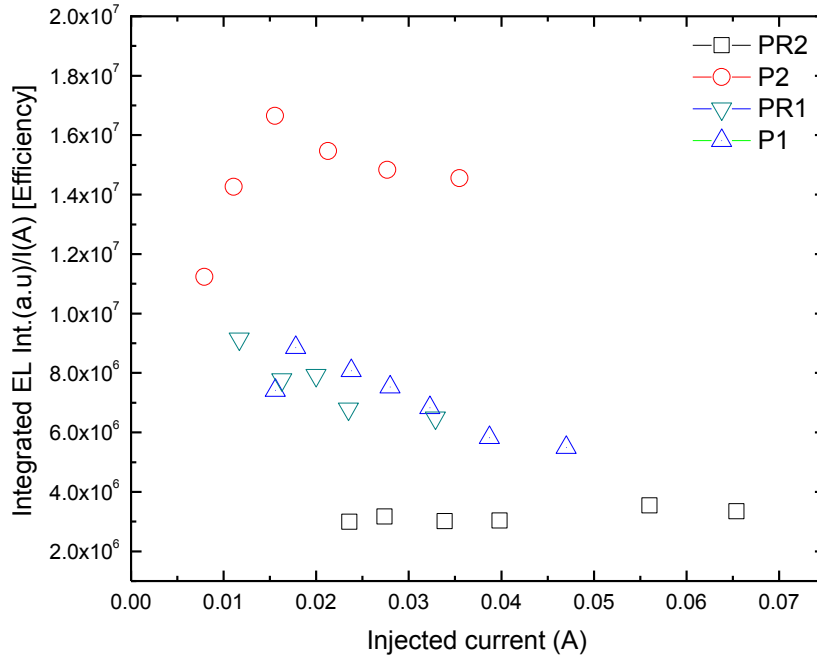


Figure (61) Integrated EL intensity/injected current vs injected current for the samples PR1, P1, PR2 and P2.

The energy band diagrams of the PR2 sample (with the thin SiNx layer) at equilibrium and in forward bias are shown in figures (62a) and (62b), respectively. The barrier height for electrons and holes are ~ 3 eV and 1.9 eV, respectively [17, 66]. Under low forward voltages (~ 0 -10 V) the injection of holes could be dominant and assisted by dangling bonds in the matrix or direct tunneling towards silicon nanodots. Even though this sample exhibited higher currents under low voltages its threshold voltage was lower than the EL turn on voltage (>10 V) which suggest high carrier leakage and/or strong non-radiative recombination. With increasing voltages the enhanced injection of carriers from the ZnO:Al/SiQDs and c-Si/SiNx interfaces gave rise to a higher number of radiative processes as the electroluminescence spectra validated. However, because of the addition of the SiNx layer higher charge accumulation in the silicon surface can be abruptly injected under low voltages. This process taking place in the samples with the thin SiNx film could be more easily affected by interface charges than the samples without it (P1, PR1). The gold nanoparticles added to the structure of the figure (62b) proved constraint the injected current and increase the radiative recombination; however, it is not clear if the augmented EL emission in the P2 sample is just an effect of the higher current injection from low voltages due to the SiNx layer.

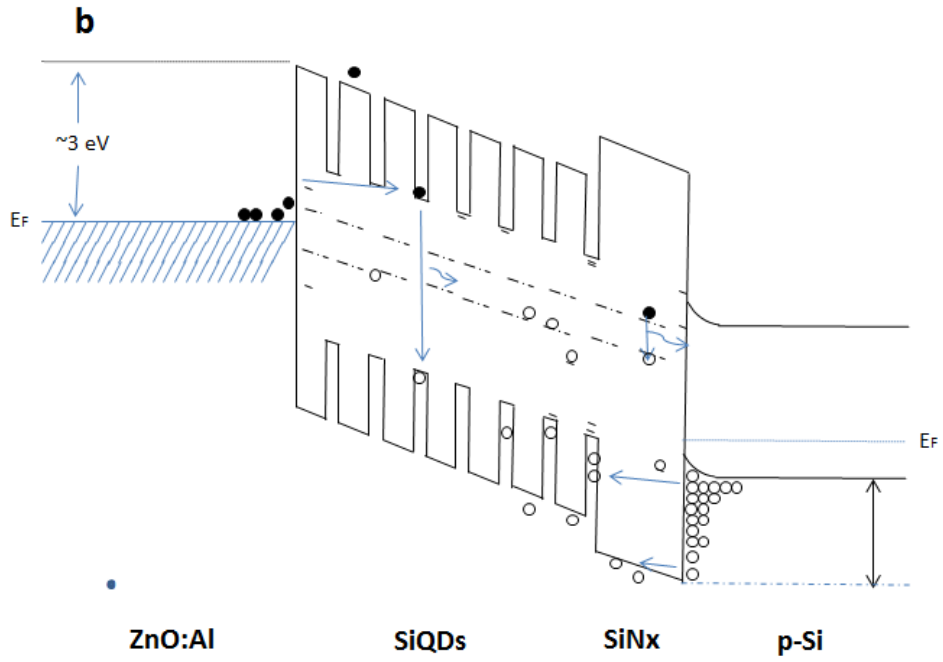
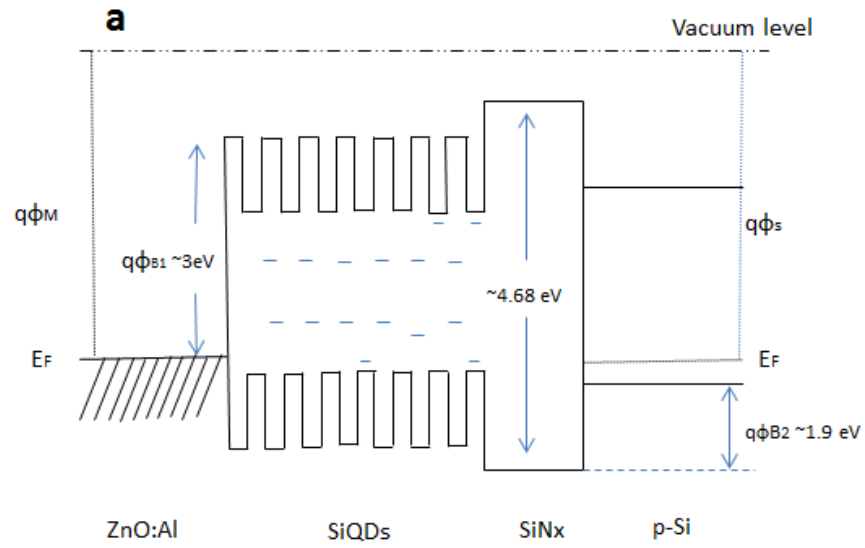


Figure (62) Energy band diagrams of the PR2 sample (with the thin SiNx layer) at equilibrium (a) and under forward bias (b).

6.3 Second stage of fabrication of metal-insulating-semiconductor devices based on SiQDs

With the aim to investigate the electrical behavior of devices with 5 and 10 nm thick of gold thin films, the following structures were fabricated:

P3) c-Si/Au(5nm thickness)/SiNx/SiQDs/ZnO:Al

P4) c-Si/Au(10nm thickness)/SiNx/SiQDs/ZnO:Al

The cleaning of the substrates and parameters used to deposit the different types of layers were those indicated in section 6.2.1. Despite of the fact that the high and roughness of gold layers of 5 nm and 10 nm thicknesses were higher than those of 1 nm thickness, it was used a 10 nm thin layer of SiNx in these devices because it was observed in the previous section that this layer could promote carrier injection.

6.3.1 Optical and electrical characterization

White electroluminescent emission spectra were observed in these samples in forward bias (Fig. 63). EL intensity increased with increasing voltage. The peak position in both samples was slight blue-shifted at around 580 nm compared with that of P2 sample (1 nm thickness of gold) at ~600 nm. The EL turn on emission started at 14V and 12V in samples P3 and P4, respectively. Voltage steps of 2V in sample P3 (5 nm thickness) were required to get observe increased intensity of the emission spectrum. Meanwhile, for sample P4 (10 nm thickness) the EL intensity increased by applying voltage steps of 1V. At the same applied voltages of 14V and 16V, the EL intensity in the P4 sample was around three and two fold higher than in P3 sample, respectively.

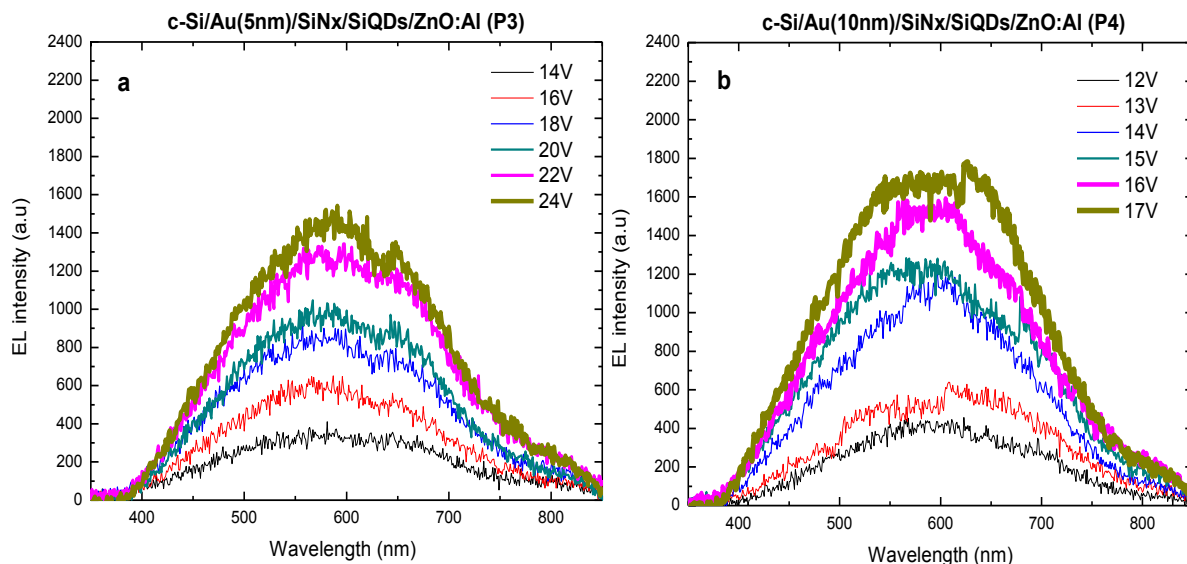


Figure (63) EL spectra of the samples P3 (a) and P4 (b).

The comparison of integrated EL intensity vs injected current of the samples P3, P4 and the sample P2 studied in the previous chapter is depicted in figure (64a). A lineal behavior was seen for all samples indicating that the radiative emission is related to the carrier injection. The P2 sample (1 nm thickness) showed the highest positive slope followed by samples P4 (10 nm thickness) and P3 (5 nm thickness).

Current density against electric field curves of the samples P2, P3, and P4 showed lower threshold voltage for the sample P4 as well as higher current injection in forward and reverse bias than in samples P2 and P3. The highest current density observed in P4 sample might be an effect of its highest roughness at the c-Si/SiN_x interface by the gold nanostructure when compared with those found at the interface of P2 and P3 samples. The latter because the interface topography induces a strong electric field located at the apex of protrusions [60, 82]. However, higher roughness in the P3 sample by means of gold nanoparticles did not improved the injected current when compared with that of P2 sample. This may be due to the effectiveness of the SiN_x layer like a barrier promoting higher accumulated charge at the silicon surface. A change in color of the SiQDs film with a 10 nm thickness gold nanostructure was observed with respect to its reference, which indicated higher thickness in the sample with gold metal. This suggests that the metal could act as catalyst during the insulating film deposition. Then, the covered surface, morphology and size of 10 and 5 nm thicknesses gold nanostructures could influence deposition of the dielectric film in a chemical and physical level changing its insulating properties.

The conduction mechanism Pool-Frenkel fitted well the samples P3 and P4 in the same way it did in P2 sample (Appendix B). Finally, the EL efficiency of samples P2, P3 and P4 is compared in figure (64c). The P3 sample exhibited a higher EL efficiency than the P4 sample; however, for higher currents it started decreasing gradually. Conversely, the EL efficiency raised slowly in the P4 sample when the current was increasingly injected on the device indicating a reduced influence of the droop phenomenon at higher current density for this sample. Moreover, the efficiency for the P2 sample (1 nm gold thickness) was the highest getting a maximum peak after which it started decreasing. Regardless this drop at higher current density, the efficiency in the P2 sample remained superior compared with those of samples P3 and P4. The SEM image of the cross section of the P4 sample and an image obtained with an optical microscope of a device of this structure after forward bias are shown in figure (65).

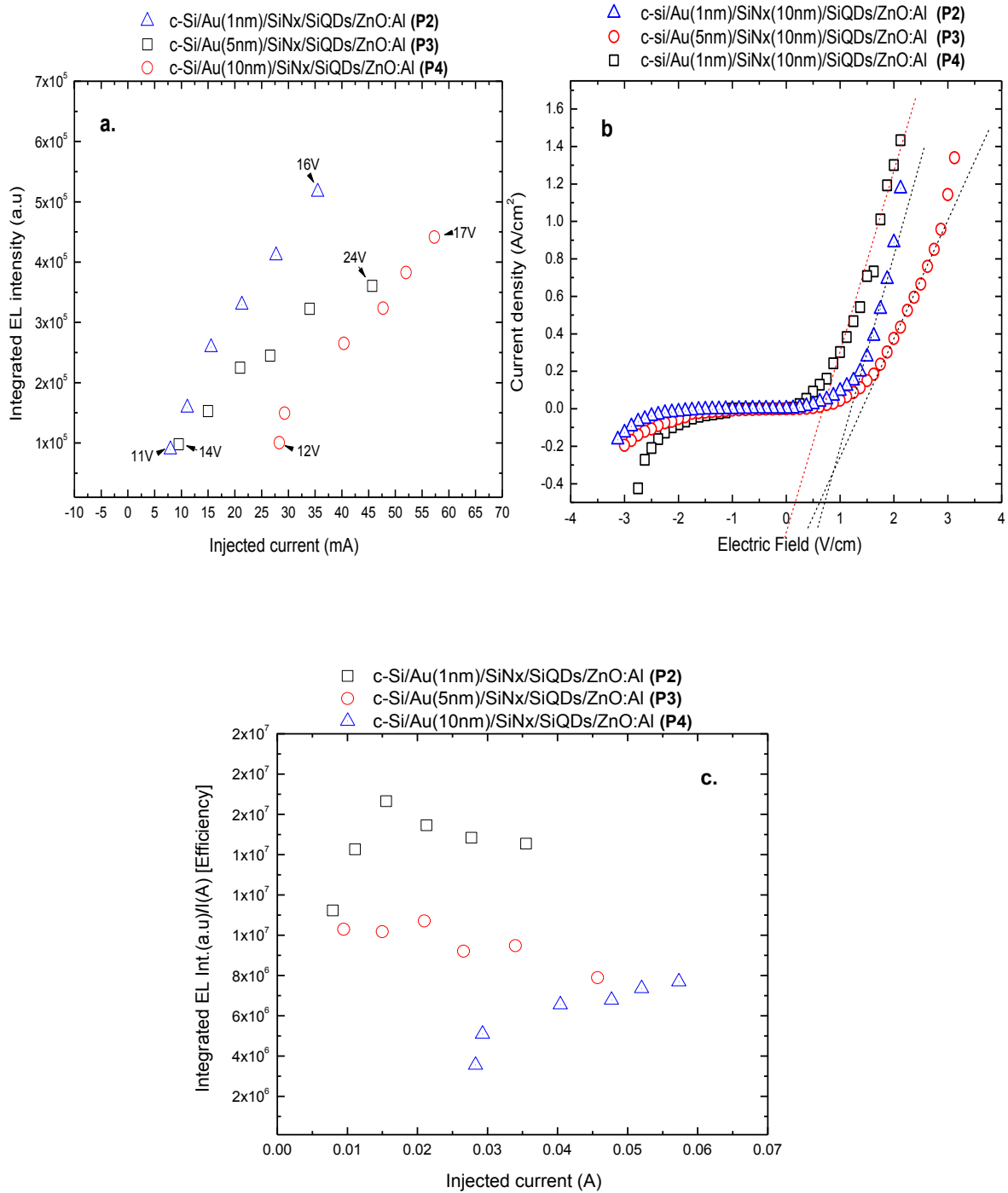


Figure (64) (a) Integrated EL intensity vs injected current (b) Current density vs electric field and (c) Integrated EL intensity/injected current vs injected current plots of the samples P2, P3 and P4 with gold nanostructures.

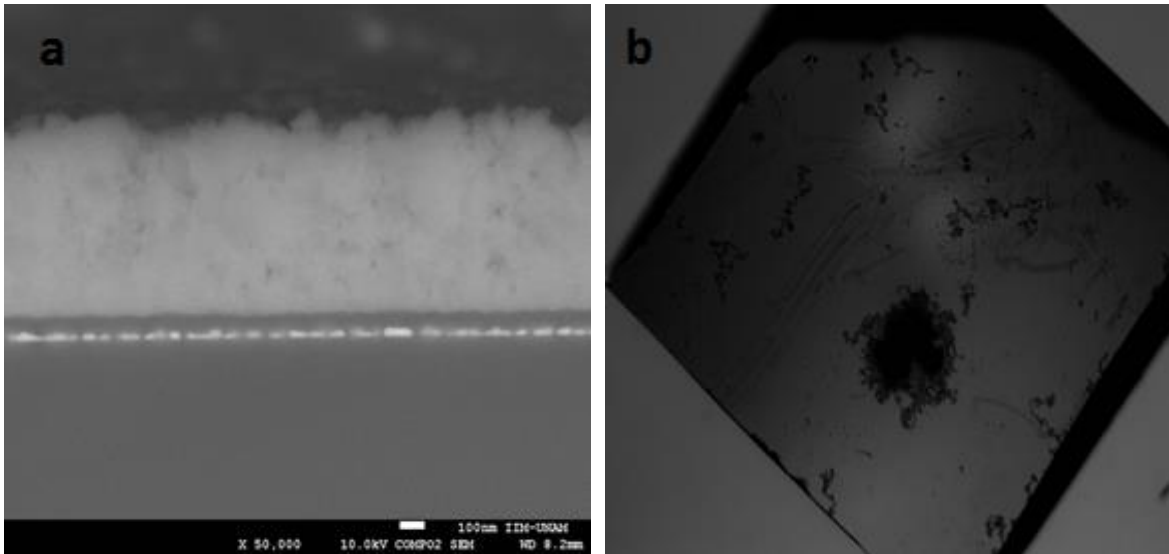


Fig. (65) (a) SEM image of the cross section of the P4 sample and (b) image obtained with optical microscope of a device after forward bias.

6.4 Conclusions

In the first stage of fabrication of light emission devices the optical and electrical properties of four electroluminescent structures based in silicon nanoparticles were studied. Light emission of the four samples could be observed at room temperature in a medium dark room with the naked eye. Some conclusions can be summarized as follows:

- White electroluminescence could be observed in all the samples under forward bias. Samples with 2.9 nm diameter gold nanoparticles (P1, P2) showed higher current injection and lower EL turn on voltage than their corresponding references. EL enhancement of 1.74 and 5.94 was observed in the P1 and P2 sample, respectively, at the same electric field.
- The highest EL efficiency was seen in the P2 sample increasing up to a maximum after which started to diminish gradually. On the other hand, EL efficiency in sample PR2 was constant and lowest. Likewise, EL efficiency in samples PR1 and P1 drooped with increasing current injection. Some explanations for this phenomenon are carrier leakage, large Auger recombination and junction heating.
- In spite of higher band gap of the SiN_x layer, it was found this could promote current injection to the bulk of SiQDs film probably due to higher accumulation charge at the surface of the silicon substrate. This effect might increase injection of hot carriers to the bulk of the insulating, which were constrain by the presence of gold nanoparticles in the PR2 sample as the current vs. voltage curves of different devices of the same structure showed.
- At low electric fields the conduction mechanism for all the samples (PR1, P1, PR2 and P2) was dominated by space charge. At high electric fields the Pool-Frenkel (P-F) mechanism was the best fitting for samples P1, P2 and PR2. For the PR1 sample the transport mechanism assisted by traps (TAT) fitted better its curve.
- As discussed in chapter three the origin of electroluminescence is mostly duo to exciton recombination in silicon quantum dots, although other kind of recombination centers as localized

defects in the matrix are involved as well. However, the performed electroluminescence measurements are not conclusive on the enhancement mechanism of PR2 sample, but the influence of the thin SiNx layer had an essential role when gold nanoparticles were close.

During the second fabrication stage were employed 5 nm and 10 nm gold thicknesses using the same configuration as in the P2 sample (c-Si/Au/SiNx/SiQDs/ZnO:Al). Thus, some of the conclusions are the following:

- Visible electroluminescence emission was observed in forward bias for the P3 and P4 samples. The peak position of these samples with 5 nm and 10 nm gold thicknesses (P3 and P4) was seen at around 580 nm. In both samples EL intensity increased with increasing voltages. The P4 sample had lower EL turn on voltage and also higher injected current. At the same applied voltages of 14V and 16V, the EL intensity in the P4 sample was around three and two fold higher than in P3 sample, respectively.
- The comparison of integrated EL intensity vs injected current of the samples P2, P3, and P4 showed a lineal behavior for all samples indicating that the radiative emission is related with carrier injection.
- Current density against electric field curves of the samples P2, P3, and P4 showed lower threshold voltage for the sample P4 as well as higher current injection in forward and reverse bias than in samples P2 and P3. The highest current density observed in P4 sample might be an effect of its highest roughness at the c-Si/SiNx interface by the gold nanostructure when compared with those found at the interface of P2 and P3 samples. The latter because the interface topography induces a strong electric field located at the apex of protrusions [60, 82]. However, higher roughness in the P3 sample by means of gold nanoparticles did not improved the injected current when compared with that of P2 sample. This may be due to the effectiveness of the SiNx layer like a barrier promoting higher accumulated charge at the silicon surface.
- The P3 sample exhibited a higher EL efficiency than the P4 sample; however, for higher currents it started decreasing gradually. Conversely, the EL efficiency raised slowly in the P4 sample when the current was increasingly injected on the device indicating a reduced influence of the droop phenomenon at higher current density for this sample. Moreover, the efficiency for the P2 sample (1 nm gold thickness) was the highest getting a maximum peak after which it started decreasing.

Bibliography

- [1] D. A. Muller, T. Sorsch, S. Moccio, F. H. Baumann, K. Evans-Lutterodt & G. Timp, *Nature*, Vol. 399 (1999).
- [2] William Gropp, Lecture 15: Moore's Law and Dennard Scaling, www.cs.illinois.edu.
- [3] G.Q. Lo, K. W. Ang, T. Y. Liow, Q. Fang, J. Zhang, S. Y. Zhu, J. F. Song, Y. Z. Xiong, F. F. Ren, M. B. Yu and D.-L. Kwong, *ECS Transactions*, 28 (1) 3-11 (2010).
- [4] Robert Joseph Walters, *Silicon Nanocrystals for Silicon Photonics*, California Institute of Technology 2007 Doctoral thesis.
- [5] Leonid Khriatchchev, *Silicon Nanophotonics*, Pan Stanford Publishing 2009.
- [6] L. T. Canham, *Applied Physics Letters*, 57 1046-1048 (1990).
- [7] Tsuyoshi Oguro, Hideki Koyama, Tsuyoshi Ozaki, and Nobuyoshi Koshida, *Journal of Applied Physics*, 81, 1407 (1997).
- [8] J. Fandiño, A. Ortiz, L. Rodríguez-Fernández, and J. C. Alonso, *Journal of Vacuum Science & Technology A* 22 570 (2004).
- [9] A. Benami, G. Santana, A. Ortiz, A. Ponce, D. R. Aguilar-Hernández, J. Contreras Puentes, and J. C. Alonso, *Nanotechnology* 18, 155704 (2007).
- [10] A. Benami, G. Santana, B. M. Monroy, A. Ortiz, J. C. Alonso, J. Fandiño, J. Aguilar-Hernández, and G. Contreras-Puentes, *Physica E* 38, 148 (2007).
- [11] A. Morales-Sanchez, J. Barreto, C. Dominguez, M. Aceves and J. A. Luna-López, *Nanotechnology* 20 045201 (2009).
- [12] M. Perálvarez, J. Barreto, Josep Carreras, A. Morales, D. Navarro-Urrios, Y. Lebour, C. Domínguez and B. Garrido, *Nanotechnology* 20 405201 (2009).
- [13] J. Bornacelli, J. A. Reyes Esqueda, L. Rodríguez-Fernández, J. L. Ruvalcaba-Sil, F. J. Jaimes, and A. Oliver, *Journal of Nanotechnology*, 863184 (2014).
- [14] J. Zhou, G. R. Chen, Y. Liu, J. Xu, T. Wang, N. Wan, Z. Y. Ma, W. Li, C. Song, and K. J. Chen, *Optics Express* 156 (2009).
- [15] D. Li, Y-B Chen, Y. Ren, J. Zhu, Y-Y Zhao and M. Lu, *Nanoscale Research Letters*, 7:200 (2012).
- [16] J. S. Biteen, D. Pacifici, N. S. Lewis and H. A. Atwater, *Nano Letters*, 5 1768–1773 (2005).
- [17] D. Li, F. Wang and D. Yang, *Nanoscale*, 5 3435-3440 (2013).
- [18] Feng Wang, Dongsheng Li, Deren Yang and Duanlin Que, *Applied Physics Letters* 100, 031113 (2012).
- [19] Silicon photonics. An introduction. Graham T. Reed, Andrew P. Knights, John Wiley & Sons, Ltd (17-20).
- [20] Silicon photonics, Lorenzo Pavesi, David J. Lockwood, Springer (17-25).
- [21] Introduction to Solid State Physics, Charles Kittel, Seventh Edition (18-20).
- [22] A.K. Panchal, D.K. Rai, M. Mathew and C.S. Solanki, *NANO: Brief Reports and Reviews*, Vol. 4, 5 265–279 (2009).
- [23] A. Rodriguez, J. Arenas, J.C. Alonso, *Journal of Luminiscence*, 132 2385-2389 (2012).
- [24] Device Applications of Silicon Nanocrystals and Nanostructures, Nobuyoshi Koshida, Springer.
- [25] Silicon Nanocrystals, Lorenzo Pavesi and Rasit Turan, Ed. Wiley.
- [26] N. Zheludev, *Nature Photonics*, Commentary, Vol. 1, (2007).
- [27] F. A. Harraza, , *Sensors and Actuators B* 202 897–912 (2014).
- [28] M. Wang, A Anopchenko, A. Marconi, E. Moser, S. Prezioso, L. Pavesi, G. Pucker, P. Bellutti and L. Vanzetti, *Physica E*, 41 912-915 (2009).
- [29] D. Li, Y-B Chen, Y. Ren, J. Zhu, Y-Y Zhao and M. Lu, *Nanoscale Research Letters*, 7:200, (2012).
- [30] C-H Lu, S-E Wu, Y-L Lai, Y-L li, C-P Liu, *Journal of Alloys and Compounds*, 585 460-464 (2014).
- [31] K. Okamoto, I. Niki, A. Shvartser, G. Maltezos, Y. Narukawa, T. Mukai, Y. Kawakami, and A. Scherer, *Physica Status Solidi*, 204 6 2103–2107 (2007).

- [32] Chemical Vapor Deposition, Srinivasan Sivaram, Springer Science+Business Media, LLC (1-3).
- [33] Stanley Wolf, Richard N. Tauber, Silicon processing for the VLSI Era, Vol. 1, Lattice Press (164, 171-172).
- [34] J. Fandiño, A. Ortiz, L. Rodríguez-Fernández, and J. C. Alonso, *Journal of Vacuum Science & Technology A* 22, 570 (2004).
- [35] Klaus Pagh Almqvist, Structural Characterization of Nanocrystalline Thin Films Grown by Magnetron Sputtering, University of Aarhus (2006) Doctoral Thesis [6-8].
- [36] Viguie JC, Spitz J. Chemical Vapor Deposition at Low Temperatures, *Journal of the Electrochemical Society*, 122: 585-8 (1975).
- [37] Hoda Amani Hamedani, Investigation of deposition parameters in ultrasonic spray pyrolysis for fabrication of solid oxide fuel cell cathode, Georgia Institute of Technology, Master thesis (2008) [24-26].
- [38] Radek Machán, Supported Phospholipid Bilayers and their Interactions with Proteins Studied by Ellipsometry, Atomic Force Microscopy and Confocal Fluorescence Microscopy, J. Heyrovský Institute of Physical Chemistry of ASCR, Thesis (2011).
- [39] R.M.A. Azzam, N.M. Bashara, Ellipsometry and polarized light, 2nd Edition, Elsevier, Amsterdam, 1987.
- [40] John C. Vickerman, Ian S. Gilmore, Surface Analysis, 2nd. Edition, John Wiley & Sons (47-49, 511-513).
- [41] Introduction to the Scanning Electron Microscope, Michael Dunlap & Dr. J. E. Adaskaveg, Facility for Advanced Instrumentation.
- [42] P. F. Trwoga, A. J. Kenyon, and C. W. Pitt, *Journal of Applied Physics*, 83 (1998).
- [43] L. Liu, C. S. Jayanthi, S. Y. Wu, *J Appl. Phys.*, 90 4143 (2001).
- [44] A. Benami, G. Santana, A. Ortiz, A. Ponce, D. R. Aguilar-Hernández, J. Contreras Puentes, and J. C. Alonso, *Nanotechnology* 18, 155704 (2007).
- [45] A. Benami, G. Santana, B. M. Monroy, A. Ortiz, J. C. Alonso, J. Fandiño, J. Aguilar-Hernández, and G. Contreras-Puentes, *Physica E* 38, 148 (2007).
- [46] A. Martínez, J. C. Alonso, L. E. Sansores, and R. Salcedo, *J. Phys. Chem. C* 114, 12427–12431 (2010).
- [47] J. Robertson and M. J. Powell, *Appl. Phys. Lett.* 44 4 (1984).
- [48] S. Jung, Y. Fujimura, T. Ito, and H. Shirai, *Solar Materials & Solar Cells* 74 421-427 (2002).
- [49] Hajime Shirai, *Thin Solids Films* 457 90-96 (2004).
- [50] F. Reizman and W. van Gelder, *Solid-State Electronics*, Vol. 10 7 625-632 (1967).
- [51] L. Jiang, X. Zeng, and X. Zhang, *Journal of Non-Crystalline Solids* 357 2187-2191 (2011).
- [52] B. S. Sahu, F. Delachat, A. Slaoui, M. Carrada, G. Ferblantier, and D. Muller, *Nanoscale Research Letters* 6 178 (2011).
- [53] G. Santana, B. M. Monroy, A. Ortiz, L. Huerta, and J. C. Alonso, *Applied Physics Letters* 88, 041916 (2006).
- [54] G. Scardera, T. Puzzer, I. Perez-Wurfl, and G. Conibeer, *Journal of Crystal Growth*, 310 3680-3684 (2008).
- [55] T. Grigaitis, A. Naujokaitis, S. Tumėnas, G. Juška, and K. Arlauskas, *Lithuanian Journal of Physics*, Vol. 55, No. 1, 35–43 (2015).
- [56] F-C Chiu, *Advances in Materials Science and Engineering*, (2014).
- [57] Physics of Semiconductor Devices, S. M. Sze, Kwok K. Ng, Wiley Interscience, 3er. Edition, (134-153).
- [58] J. C. Alonso, F.A. Pulgarin, B. M. Monroy, A. Benami, M. Bizarro, A. Ortiz, *Thin solid Films*, 518 3891–3893 (2010).
- [59] A. Morales-Sanchez, J. Barreto, C. Dominguez, M. Aceves and J. A. Luna-López, *Nanotechnology* 20 045201 (2009).

- [60] N. Gaillard, L. Pinzelli, and M. Gros-Jean, *Applied Physics Letters* 80, 133506 (2006).
- [61] Z. W. Pei, Y. R. Chang, and H. L. Hwang, *Appl. Phys. Lett.* 80 2839–2841 (2002).
- [62] R. Huang, J. Song, X. Wang, Y. Q. Guo, C. Song, Z. H. Zheng, X. L. Wu, and P. K. Chu, *Optics Letters* 37, 4 692-694 (2012).
- [63] A. Rodríguez-Gómez, A. García-Valenzuela, E. Haro-Poniatowski, and J. C. Alonso-Huitrón, *J. Appl. Phys.* 113, 233102 (2013).
- [64] R. Huang, K. Chen, H. Dong, D. Wang, H. Ding, W. Li, J. Xu, Z. Ma, and L. Xu, *Applied Physics Letters* 91, 111104 (2007).
- [65] R. Huang, D. Q. Wang, H. L. Ding, X. Wang, K. J. Chen, J. Xu, Y. Q. Guo, J. Song, and Z. Y. Ma, *Optics Express* 1144 (2010).
- [66] S. A. Cabañas-Tay, L. Palacios-Huerta, J. A. Luna López, M. Aceves-Mijares, S. Alcantara-Iniesta, S. A. Pérez-García, and A. Morales-Sánchez, *Semiconductor Science and Technology*, 30 (2015).
- [67] T. Oguro, H. Koyama, T. Ozaki, and N. Koshida, *J. Appl. Phys.* 81 3 (1997).
- [69] B-H Kim, C-H Cho, J-S Mun, M-K Kwon, T-Y Park, J. S. Kim, C. C. Byeon, J. Lee, and S-J Park, *Advanced Materials*, 20, 3100-3104 (2008).
- [70] Xue Feng, Fang Liu, Yidong Huang, *Optics Communications* 283 2758-2761 (2010).
- [71] S. Pillai, K. R. Catchpole, T. Trupke, G. Zhang, J. Zhao, and M. A. Green, *Applied Physics Letters* 88, 161102 (2006).
- [72] C. Louis, O. Pluchery, *Gold Nanoparticles for Physics, Chemistry and Biology*, Imperial College Press, 1st Edition.
- [73] K. Huang, N. Gao, C. Wang, X. Chen, J. Li, S. Li, X. Yang, and J. Kang, *Scientific Reports*, 4 4380.
- [74] X. Gu, T. Qiu, W. Zhang, P. K. Chu, *Nanoscale Research Letters*, 6 199 (2011).
- [75] A. Rodríguez, J. Arenas, A. L. Pérez-Martínez, and J. C. Alonso, *Materials Letters*, 125 44-47 (2014).
- [76] X. Jiang, Z. Ma, J. Xu, K. Chen, L. Xu, W. Li, X. Huang, and D. Feng, *Nature*, 5:15762 (2015).
- [77] X. Wang, K-P Chen, M. Zhao, and D. D. Nolte, *Optics Express*, 18, 24 24859 (2010).
- [78] B. Streetman and S. K. Banerjee, *Solid State Electronic Devices*, 6th Edition, PHI Learning.
- [79] D. J. DiMaria, J. R. Kirtley, E. J. Pakulis, D. W. Dong, T. S. Kuan, F. L. Pesavento, T. N. Theis, and J. A. Cutro, *Journal of Applied Physics*, 56 2 (1984).
- [80] N. Tansu, L. J. Mawst, *Journal of Applied Physics*, 97 054502 (2005).
- [81] H. Zhao, G. Liu, J. Zhang, R. A. Arif, and N. Tansu, *Journal of Display Technology*, 9 4 (2013).
- [82] M. C. V. Lopes, S. G. dos Santos, and C. M. Hasenack, *J. Electrochem Soc.* 143 1021 (1996).

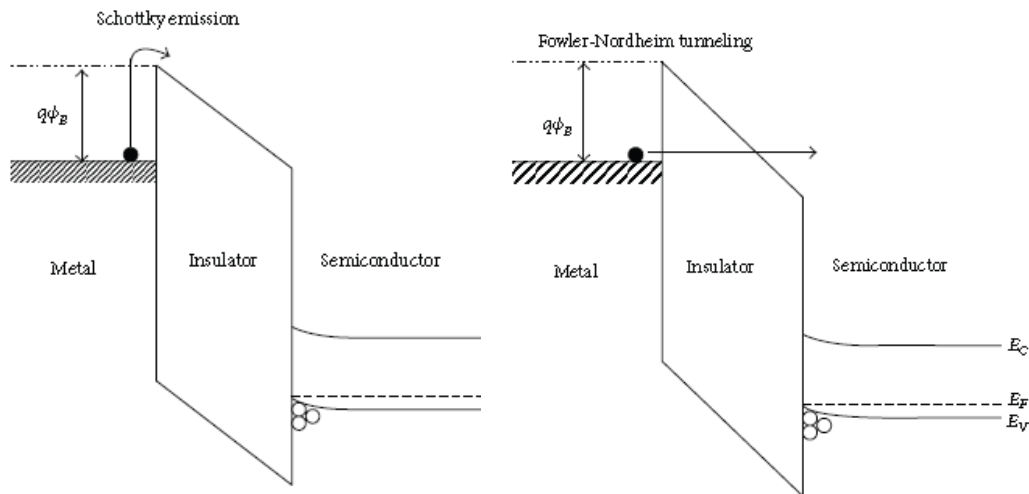
Appendix A

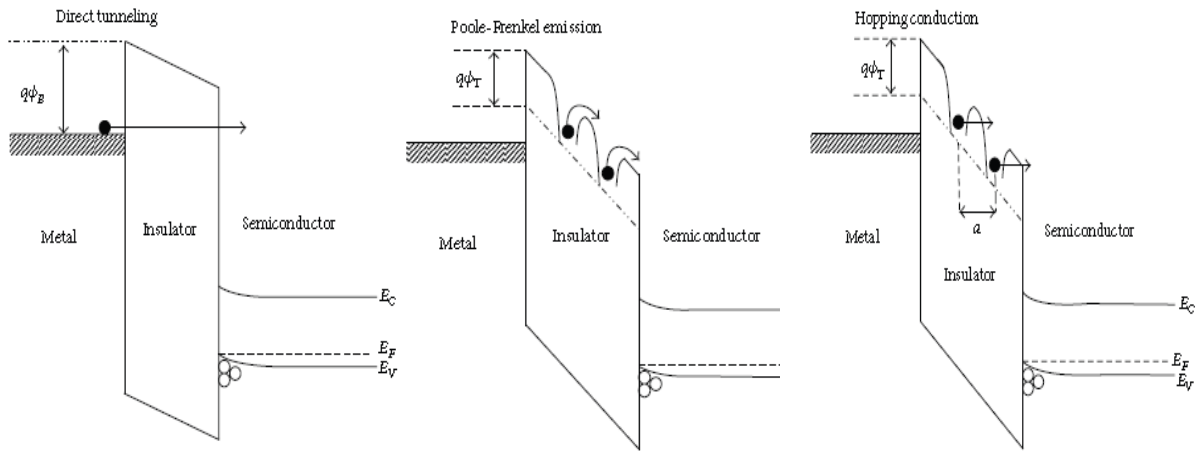
Table (1A) Basic conduction processes in insulators.

Process	Expression	Voltage and temperature dependence
Tunneling	$J \propto E^2 \exp \left[-\frac{4\sqrt{2m^*}(q\phi_B)^{3/2}}{3qhE} \right]$	$\propto V^2 \exp^{-b/V}$
Thermionic emission	$J = A^{**}T^2 \exp \left[-\frac{q(\phi_B - \sqrt{qE/4\pi\epsilon_i})}{kT} \right]$	$\propto T^2 \exp \left[\frac{q}{kT} (a\sqrt{V} - \phi_B) \right]$
Frenkel-Pool emission	$J \propto E \exp \left[-\frac{q(\phi_B - \sqrt{qE/\pi\epsilon_i})}{kT} \right]$	$\propto V \exp \left[\frac{q}{kT} (2a\sqrt{V} - \phi_B) \right]$
Ohmic	$J \propto E \exp \left[-\frac{\Delta E_{ac}}{kT} \right]$	$\propto V \exp \left[-\frac{c}{T} \right]$
Ionic conduction	$J \propto \frac{E}{T} \exp \left[-\frac{\Delta E_{ai}}{kT} \right]$	$\propto V/T \exp \left[-\frac{d'}{T} \right]$
Space-charge-limited	$J = \frac{9\epsilon_i\mu V^2}{8d^3}$	$\propto V^2$

A^{**} =effective Richardson constant, ϕ_B barrier height, E =electric field in insulator, ϵ_i = insulator permittivity, m^* =effective mass, d =insulator thickness, ΔE_{ac} =activation energy of electrons, ΔE_{ai} = activation energy of ions, $V \sim Ed$, $a = \sqrt{(q/4\pi\epsilon_i d)}$, b , c , and d' are constants [57].

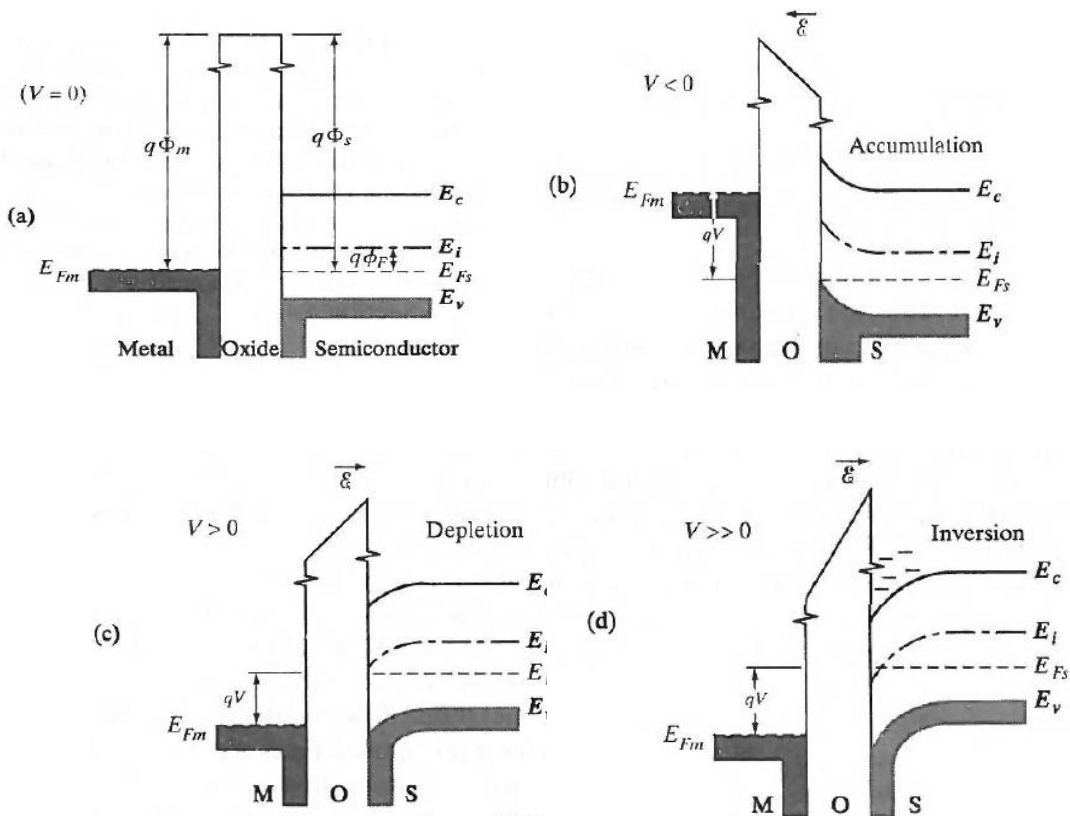
Schematic energy band diagrams of some of the main transport mechanisms in metal-insulating-semiconductor structure. Figures were obtained of [56].





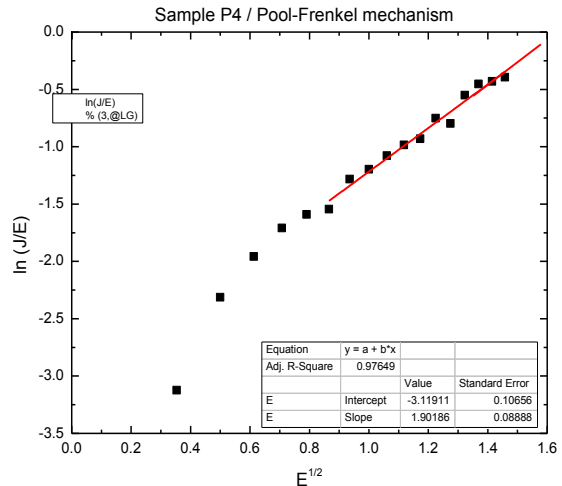
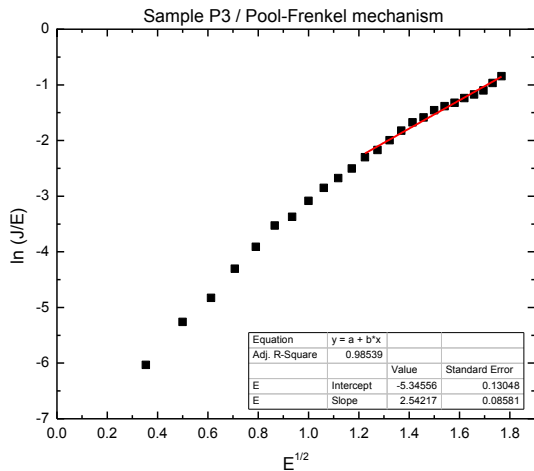
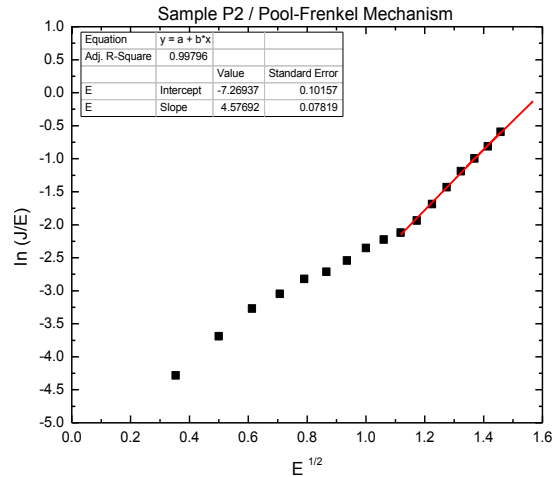
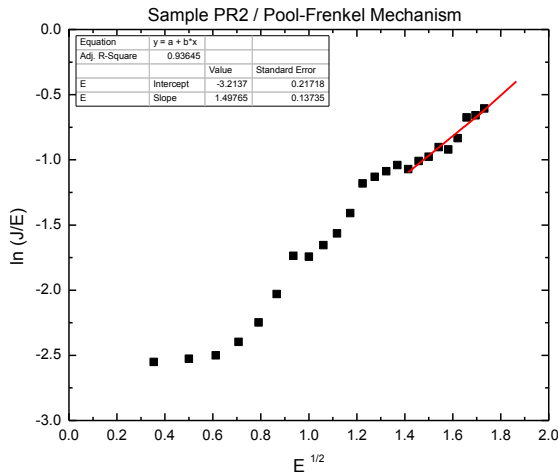
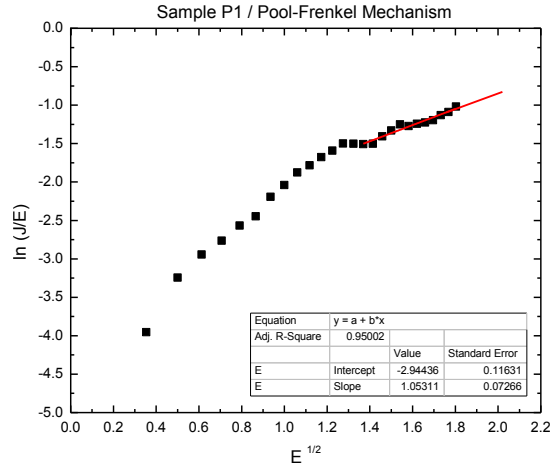
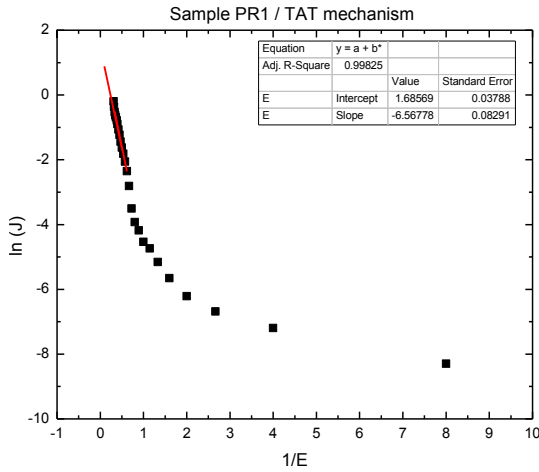
Metal-oxide-semiconductor (MOS) capacitor

Band diagram for the ideal MOS structure using a p-type semiconductor at: (a) equilibrium; (b) negative voltage applied to the metal produces hole accumulation in the semiconductor; (c) positive voltage depletes holes from the semiconductor surface; (d) a larger positive voltage causes inversion [78].

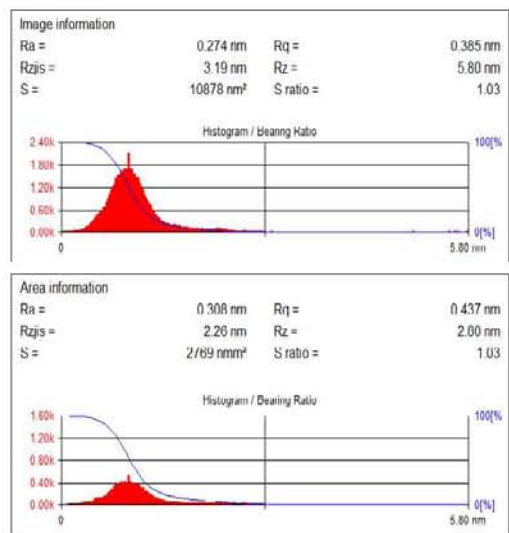
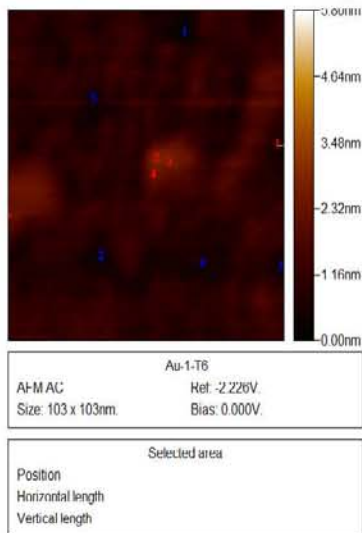
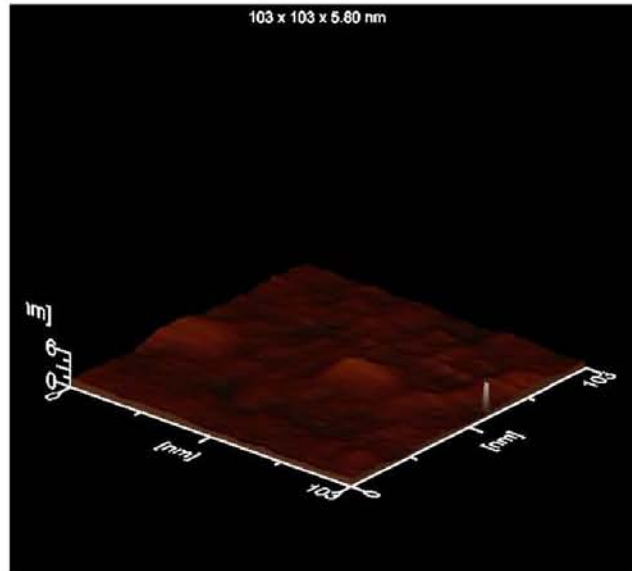


Appendix B

Fitting of the current density-electric field characteristics in the high electric field region of the PR1, P1, PR2, P2, P3 and P4 samples.



AFM image in topographic mode of 2.9 nm diameter gold nanoparticles (Au-A) on silicon.
 Ra=roughness, Rz=height.





Chem. Sci., 2014, 5, 102–108 | 102

Photoluminescence enhancement from silicon quantum dots located in the vicinity of a monolayer of gold nanoparticles†

 A. I. Muñoz-Torres,^a A. Rodríguez-Gómez,^{b,c} J. A. Arenas-Alatorre^b and J. C. Martínez-Ortíz^b

In this work we show that it is possible to carry out a functional coupling between a thin film of silicon quantum dots on a substrate (silicon quantum dots (SQDs) on a substrate) and gold nanoparticles by using a very well controlled growth technique. In this case, the microstructure is controlled by using a plasma enhanced chemical vapor deposition (PECVD) and sputtering. The coupled structure shows a 100% of photoluminescence (PL) enhancement compared with the SQDs without the gold monolayer. The SQDs used in this work were an average diameter of 10 nm, a surface density of 6.0×10^{11} particles per cm² and a monolayer film area of 500×500 nm². Additionally, the gold nanoparticles were prepared with the following characteristics: the particles are embedded in a silicon nitride matrix showing a spherical shape, an average diameter of 25 nm, a surface density of 2.0×10^{11} particles per cm² and a monolayer film area of 500×500 nm². We found that there is an optimum separation distance between SQDs and the gold monolayer to achieve the maximum photoluminescence enhancement. For our structure, the optimum distance was 10 nm. We conclude that there could be a combined physical mechanism of the enhancement of a photoluminescence limited by the variation of the electronic mechanisms of the primary layer.

 Received 26th September 2013
Accepted 27th October 2013

 DOI: 10.1039/C3RA00011A
www.rsc.org/advances

Introduction

Silicon is extensively used in the present silicon technology industries due to its physical characteristics, abundance and its natural occurrence in nature.¹ However, silicon quantum applications are serious because its optical band structure is indirect or its emission efficiency is very low.²

A great number of researchers have studied the spherical three-dimensional regions of not more than 10 nm in diameter, which align on a substrate, the maximum of the valence band and the minimum of the conduction band occurs. This phenomenon is known as quantum confinement effect (QCE).^{3–5} The QCE greatly improves the silicon quantum luminescent (QL) and electroluminescent (EL) efficiencies to reach 100%.^{6–8} The utilization of QCE allows to increase the energy of the emission energy.^{9,10}

By using the QCE some research groups have tried to manipulate silicon at the nanoscale to manufacture the quantum devices ranging from quantum gate to light emitting diodes (LEDs) for multiple purposes.^{11–13} Unfortunately, although the PL emission in silicon has increased, but in the QCE,^{14–16} there are not yet enough to realize the full range of silicon based devices that the modern society demands.

Some researchers have tried several methods to improve the amount of the integrated emission intensity from silicon emitting quantum dots (SQDs) which are synthesized by several well known uncoordinated noble metal particles.^{17–20} Therefore, the fabrication of several silicon quantum dots (SQDs) on a substrate is a very important issue in the design of quantum devices based on silicon.²¹ However, it must be emphasized that the quantum processes of silicon based quantum dot emitting structures which show photoluminescence enhancement are not so much related to a knowledge of the electronic mechanisms as in these kind of structures have been studied by two research groups (Murray et al.²² and Deason et al.²³) and both groups are showing that by using silicon quantum dots on a substrate to their preparation.

In these works published by Murray et al. the band structure could be manipulated in four ways: (1) the introduction of Si atoms into a Si₃N₄ matrix,²⁴ (2) the introduction of a germanium or hydrogen atoms to generate SiQDs and (3) the introduction

^a Unidad de Nanotecnología, Instituto Tecnológico y de Estudios Superiores de Occidente, Av. de las Américas 1000, Toluca, México D.F., México

^b Unidad de Física, Universidad Autónoma de Occidente, Av. de las Américas 1000, Toluca, México D.F., México, E-mail: arenas@uao.mx

^c Unidad de Ingeniería y Tecnología, Instituto Tecnológico y de Estudios Superiores de Occidente, Av. de las Américas 1000, Toluca, México D.F., México. E-mail: ortiz@uao.mx
† This article is part of a collection of articles published in this journal as part of the special issue 'Photoluminescence in Silicon Quantum Dots', edited by J. C. Martínez-Ortíz, published in the journal RSC Advances, 2014, 4, 99–101.

dates in SiO_2 and Si_3N_4 (1) is done with high precision means (i.e. in a scanning transmission electron microscope) by the following steps and performed in a cleanroom: gold layer coating and etching of SiO_2 and Si_3N_4 surface; silicon nanowire particles coating by means of magnetron sputtering. Meanwhile, fabrication of $\gamma\text{-SiO}_2$ and $\gamma\text{-Si}_3\text{N}_4$ in a similar way as SiO_2 and Si_3N_4 is in a cleanroom. However, fabrication of $\gamma\text{-SiO}_2$ and $\gamma\text{-Si}_3\text{N}_4$ is done in a cleanroom for a large area (i.e. ~ 10 cm²) in a cleanroom, which is not suitable for the process.

The results revealed by this paper are showing a heterogeneity in growth of two different phases character when using metal nanowire particles and based on the analysis of micrographs images (Fig. 1a, b). First, the present experimental results of $\gamma\text{-SiO}_2$ and $\gamma\text{-Si}_3\text{N}_4$ are the first of the FL enhancement, respectively in the FL enhancement fields under the growth of $\gamma\text{-SiO}_2$ and $\gamma\text{-Si}_3\text{N}_4$ in different degrees of FL enhancement when SiO_2 and Si_3N_4 are deposited on metal particles in an homogeneous manner. To test these effects, we use to compare the distances between silicon and metal particles are related to order to primary generating and to enhance characteristics. However, the main concern is to make the silicon nanowire (NW) in a similar way as the process of the FL enhancement in a regular functional commercial device, which is (a) fabrication techniques must be highly compatible with those used in microelectronic industry; (b) it is essential to give a comprehensive description of particle characteristics of both metal and SiO_2 and Si_3N_4 ; and (c) it should be clarified the emission relationship between FL enhancement and the separation distance between SiO_2 and metal particles.

In this work, we have realized a multilayered structure (coupling silicon to gold) which exhibits a useful FL enhancement. For its fabrication, we have combined Remote Plasma Enhanced Chemical Vapor Deposition (RPCVD) and Sputtering techniques in a second order laser system with a mirror with those used in the microelectronic industry (i.e. dry, low temperature, vacuum and final fabrication). Our paper reflects thorough study of size and particle density of both gold and silicon nanoparticles; and it is also briefly discussed the role played by the surrounding medium in which particles are embedded when the FL enhancement is achieved. First, $\gamma\text{-SiO}_2$ and $\gamma\text{-Si}_3\text{N}_4$ synthesis have been done using gold nanoparticles of the separation distances between SiO_2 and the metal layer of gold nanoparticles (AuNP) in order to obtain the enhancement.

Experimental section

The AuNPs were prepared using a Cassagnum 160 Sputter Coater with a target (99.9999% purity) of different regions in a plasma. Quartz and silicon targets (100 μm thickness) of $\gamma\text{-SiO}_2$ and $\gamma\text{-Si}_3\text{N}_4$ were used as substrates. All the deposition masks of substrates were vacuum cleaned with 100°C of ethylene and acetone. All the substrates were cleaned by Scotch-Brite to remove dust and residue. Two thin films of silicon (~ 10 nm) with different thickness (~ 10 nm) were deposited on a silicon substrate using a Remote Plasma Evaporation Chamber Vapor Deposition

(RP-EVD) system (model 100-300) with laser beam operation mode under 85 Torr. In this mode, a mixture of SiH_4 and Cl_2 gas flow rates of the laser beam were used to react in a volume of 100 cm³ of quartz with a silicon permeator. The flow rates of Cl_2 , SiH_4 and SiH_2Cl_2 were 10, 75 and 5 sccm, respectively for all the deposition films. For evaporation of AuNP was similar to 600 sccm for purifying all gas flow to maintain a silicon particle formation with a flow rate of Cl_2 and SiH_2Cl_2 and 100 sccm for growing silicon with a flow rate of SiH_4 . The thickness of these layers was varied for all the fabricated samples by controlling the flow rate time.

3D fluorescence was used to measure the mass (M) of the films using a model 74000a FL-3D permeator (SiH_4) gas with a FL-3D gas flow rate (~ 650 sccm). FL-3D measurement of SiO_2 measurements were carried out in a laboratory mark room at ambient temperature using an emission field of view (FOV) in a 5 mm x 5 mm FL-3D beam emerging at 220 nm (λ_{exc} 300 nm). The FL-3D data were recorded with a HiResMax spectrofluorometer using an optical detector an optical fiber normal to the sample emission. The detection limit (DL) of mass measurement measurements were carried out in the range from 200 to 1000 nm using a detection limit 25 km² and 10 nm in the six quantum mode of the sample size of the substrate of the AuNP and $\gamma\text{-SiO}_2$ were confirmed by high resolution electron microscopy (HRTEM) and high angle annular dark field (HAADF) using a field emission gun (FEI 2000S) which operates at 200 kV near the aberrator focus with a theoretical point-to-point resolution of 0.19 nm. The HRTEM images in planar view of these samples were recorded with a CCD camera and treated with a digital analysis program. A Field Emission Scanning Electron Microscope (FEI Quanta 2000) was used to observe shape and distribution of the AuNPs for different growing times.

Results and discussion

The first concern here is the possible existence of an optimum separation distance between SiO_2 and AuNPs for our system, we realized our structure in three stages. First stage reports and discuss the methodology we used to fabricate the multilayered structure, second stage of the SiO_2 and AuNP, and in the third stage we discuss the role played by the surrounding medium in which particles are embedded when the FL enhancement is achieved. First, $\gamma\text{-SiO}_2$ and $\gamma\text{-Si}_3\text{N}_4$ synthesis have been done using gold nanoparticles of the separation distances between SiO_2 and the metal layer of gold nanoparticles (AuNP) in order to obtain the enhancement.

Fabrication and selection of the emission field (SiO₂)

Quantum confinement (QC) in silicon nanowires can be found due to strong quantum confinement. Strong QC can enhance the quantum yield of the emission field (E-field) size of the quantum system (e.g., nm³). The quantum yield of the photodiode of

with a transition from silicon nanowire to silicon quantum dots, and the quantum dots will become quasi-circles³⁵. Then, we cannot expect the maximum photoluminescence for these emitter fields conformed by clusters with sizes below 5 nm. The efficiency of the design of emitter fields is related to the film thickness of SiQDs and the SiQD size.

On the other hand, and in order to avoid in a feasible extent the non-radiative recombination from energy carriers in the films, passivation of silicon quantum dots was carried out by means of a methyl methyl oxysulfonate (MMSO), which has demonstrated diminished dangling bonds and therefore the non-radiative recombination³⁶.

The Fig. 1 contains the photoluminescence spectra of several thin films manufactured by SiQDs embedded in a silicon nitride matrix. These samples were used in a previous work³⁷ as a comparison of the experimental system against theoretical calculations. With the exception of sample 1, which has a film thickness of 375 nm, all other samples of the group have film thickness ranging between 75 and 125 nm. The integrated intensity measured as a function of the excitation wavelength for the different samples (see Fig. 2) is around 10¹⁰ photons/s. The excitation intensity was 100 mW/cm² (1.5 mW/cm² for SiQDs range size 2–5 nm).

By maintaining constant the previously mentioned deposition conditions, but changing the SiQDs size, we will find that the maximum intensity of the photoluminescence spectrum in eqn (1) is a tool that allows us to grow SiQDs in a controlled way³⁸:

$$I_{PL}(\lambda) = -0.9079 \times A^{1.05} - 57.8838 \quad (1)$$

where A is the area under any of the SiQDs PLDs. This tool allows us to keep the area of the PLDs constant.

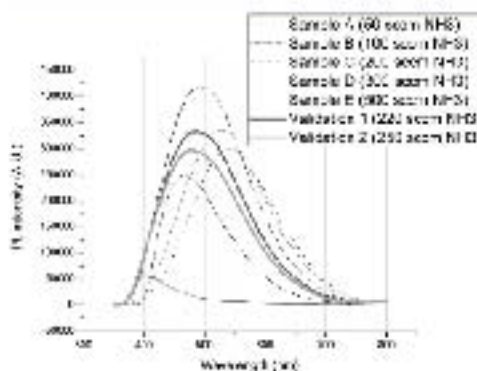


Fig. 1 Photoluminescence spectra of several thin films containing SiQDs embedded in a silicon nitride matrix. The samples were used in a previous work³⁷ as a comparison of the experimental system against theoretical calculations. With the exception of sample 1, which has a film thickness of 375 nm, all other samples of the group have film thickness ranging between 75 and 125 nm. The integrated intensity measured as a function of the excitation wavelength for the different samples (see Fig. 2) is around 10¹⁰ photons/s. The excitation intensity was 100 mW/cm² (1.5 mW/cm² for SiQDs range size 2–5 nm). Source data are provided as a Supplemental Information file.

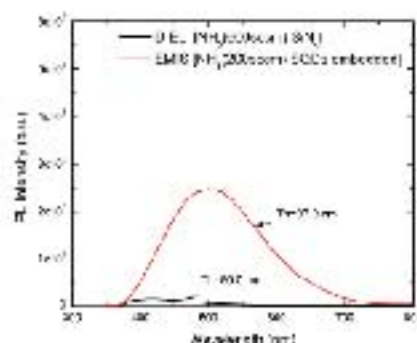


Fig. 2 Comparison between photoluminescence spectra from ENDS and DMS films. ENDS (600 nm SiQDs) and DMS (200 nm SiQDs) are shown. Both films were about the same thickness. The integrated PL intensity from the ENDS area is 22.1 times higher than DMS area.

It is important to take into consideration that blue shifts will occur for sizes with the same peak intensity of emission. An appropriate example is seen in the comparison spectrum of sample 1 from Fig. 1, which has a four times bigger thickness than sample C, but a ten times lower integrated intensity. Hence, when the films grow up to a certain thickness, it is possible to grow films with high very close to each other, with the help of a controlled emission, and the growth is controlled by eqn (2):

The Fig. 2 shows the emission spectra from ENDS film (600 nm SiQDs) and DMS film (200 nm SiQDs). ENDS and DMS film thicknesses are similar thicknesses, 600 nm and 200 nm, respectively. However, ENDS has a four times higher PL intensity than DMS film. The higher PL intensity of ENDS film results from the higher optical emission area of ENDS film. The growth of the SiQDs size into the spectrum of emission^{39,40} (the growth of the SiQDs size) will use DMS type growth, but it will use a process when the diameter of SiQDs is smaller than the DMS film thickness. The PL intensity of ENDS film is 22.1 times higher than DMS film. Hence, it is worth to note that thickness in both ENDS and DMS films can be controlled by variations in the optical emission.

A HAADF image (high-angle annular dark-field image) is shown in Fig. 3. A millimetric film still shows a very good quality of the film, as observed, confirming a good SiQD growth. This image gives rise to the largest PL integrated intensity within the range of 400–800 nm. A HRTEM micrograph is shown in the inset (SI). The observation quality of the SiQDs indicates a very high quality of silicon quantum dots. On the other hand, the low contrast between matrix and SiQDs is expected due either to the low element or to the components of the system. From these pictures, it is possible to see in detail the SiQDs morphology, most of the particles show spherical shapes, but there are also some particles with branched, conical shapes in a lower proportion. The identified spherical shapes confirm a confinement in three directions and therefore their nature of emitting quantum dots.

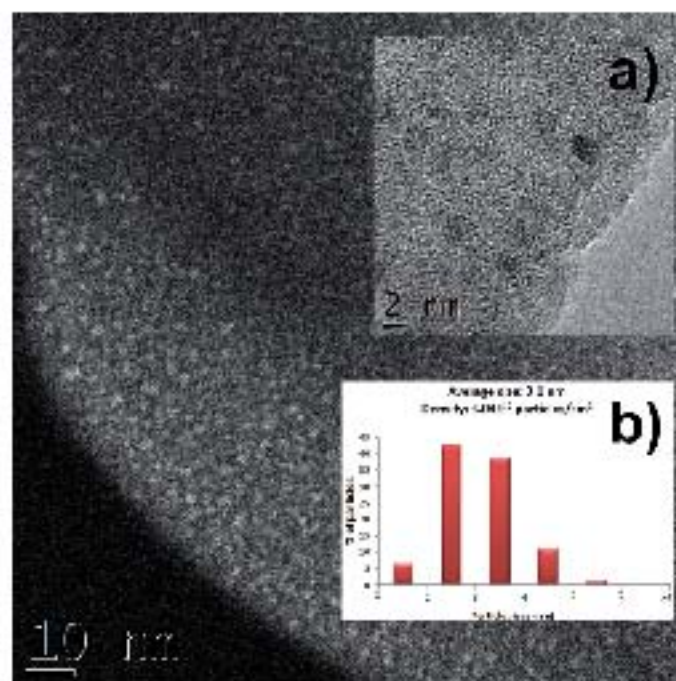


Fig. 2 HAADF-TEM image of Au@Pt nanoparticles deposited on the substrate. Inset of this image shows spherical Au@Pt nanoparticles with a 2 nm scale bar. (b) Histogram of the size distribution of Au@Pt nanoparticles. Average size is 3.1 nm and standard deviation is 0.5 nm (3.1 ± 0.5 nm).

Moreover, inset of Fig. 2 shows a histogram with the size distribution of Au@Pt film. The size is 3.1 nm, while the σ is about 0.5×10^2 particles nm^{-3} . By using well-known eqn (2), and a value of 1.18 eV to $k_{\text{Au@Pt}}$, we calculate the quantum confinement energy $E_{\text{Au@Pt}}$ resulting in a value of 1.9 eV nm^{-3} , which is in good agreement with data mentioned above. It is associated with the loss of kinetic energy of the electrons.⁴⁴

$$E_{\text{Au@Pt}} = E_{\text{Au@Pt}} + C_{\text{Au@Pt}} \quad (2)$$

Taking into account the quantum confinement effect, the structure of the design with the advantages of Au@Pt film and the highest possible size for a film grown in our RF-MS system, and hence, only the biggest Au integrated low size (σ) since the value of $k_{\text{Au@Pt}}$ is included in all our calculations. The design of a functional Au@Pt layer can depend on the deposition rate. The value was 1.5 eV nm^{-3} . Part of that rate on the substrate is 0.5 eV nm^{-3} .

Design of the gold monolayer (Au@Pt)

Non-stoichiometric metal alloys have distinct properties compared to the stable section of the electro-negative spectrum. Due that the location of these resonances depends on the size and on the film thickness and size of the particles,

they are an excellent resource for monitoring the quality and reproducibility of the goldnanoparticles monolayer.⁴⁵ For this surface analysis, we used the resonance location method to measure a large number of nanoparticles produced on a large surface of gold nanoparticles.

A specific way to describe the non-stoichiometry of a metal alloy is by using the $\text{Au}^{\text{Au}}/\text{Pt}^{\text{Au}}/\text{Pt}^{\text{Pt}}$ ratio. In a similar question, several criteria that must be made in order to grow a spherical monolayer of Au@Pt nanoparticles on a substrate are: (i) the growing rate and the position of the Au@Pt, which depends on changes in a determined substrate and second, the linear relationship between deposition time and particle average diameter (σ and ρ), which depends on larger deposition times, the bigger the Au@Pt.

To obtain monolayer gold particles, it is generally widely known that in thin films these systems are used when they grow thin layers of a few nanometers, so that the formation of spherical particles. The location of the plasmonic resonance in a non-stoichiometric gold thin film is difficult to reproduce because there are always slight changes in the location, even using identical deposition parameters. These changes are attributed to an unpredictable location of the electric field surrounding the particles, based on its composition. Thus, when the metal surface particles vaporize. Nevertheless, the growth of gold particles and reproducibility increases significantly, because the

absorption spectrum of any system, so identification of the single layer is easy.

Fig. 10 exhibits Fig. 10(a)–(c) the absorption spectra of the deposited thin samples. About 20% of the nanoparticles in sample 3 have collided, forming a larger and irregular particle. The increase of particle energy promotes an angle reduction and Au₂S₂ increases, which in turn results in a sharp drop of R_{sp} with a low value of R_{sp} during the resonance process and decreases its reliability by increasing on the thickness of the system. In general, that R_{sp} values are needed. The surface beyond growth a long time to deposition time will make R_{sp} to decrease and the resonance angle will increase. A thin metal layer is deposited at a 2-Pico-Francis of SPV in a 90 s of 90 seconds deposition can be found in 2E1 (Fig. 10[†]).

Engineering of the coupled silicon-gold structure

The structure of the coupled system is a combination of a metal coupling between FDTD simulation and structure. A KIKS method is used to get the existence of the FDTD simulation as a concept term in order to obtain an enhancement of photo-luminescence from the coupled system. All tested structures were fabricated as follows: (i) deposition of a gold monolayer (AuNP) over a silicon wafer, (ii) deposition of a Diels layer over the AuNP, (iii) deposition of a PMMA film over the previous deposited Diels layer. Dimensions of the Diels layer was adjusted by a range of thicknesses (e.g. thin layers of 10 nm, 15 nm, 20 nm, etc.) as an alternative. A typical film was carefully adjusted to a thickness of 10 nm with a thickness of 10 nm (Fig. 10(a)–(c) and Table 1).

In Fig. 6 we showed the absorption spectra of some layered structures on quartz substrate: (i) absorption spectrum of Diels layer (10 nm), (ii) absorption spectrum of gold nanoparticles surrounded by Diels layer (10 nm), (iii) absorption spectrum of gold nanoparticles surrounded by Diels layer (30 nm). As it is expected, Diels layer's transmission decreases with a slight

shift to a lower wavelength from 600 nm to 550 nm. The reflection spectra were also FDTD simulation results for AuNP's geometry distribution. The simulation is possible to select the resonance peak of the local surface plasmon at 550 nm (2.2 eV). Likewise, it can be noticed by the absorption spectrum of AuNP@Diels structure the presence of the metal nanoparticles resonance peak very close to that of the AuNP@Diels assembly in spite of different thickness of the Diels. The high homogeneity of the silicon nitride's thickness (100 nm) KIKS layers can be done in a high accuracy. The maximum error of a 10 nm gold monolayer, therefore, the above-described multilayer structures will not change the optical properties of each layer (see Table 1 for details).

From Fig. 6 can be observed four different configurations of the proposed structures (from Diels layer of 0, 20, 60 and 90 nm) and they correspond to the thickness of 0, 5, 10 and 15 nm, respectively, for each configuration. There were two results as reference without AuNP deposited on the silicon substrate for common comparison cases, i.e. only AuNP (100 nm) and AuNP only (20 nm) in our findings, were used in this first simulation as a guide. The presence of the Diels layer in a system of a Diels layer did not have change in the PL enhancement intensity in spite of the presence of Au nanoparticles in one of the structures (Fig. 6). In this case, the Fig. 6(a)–(c) were given the results of Diels before the AuNP thin deposition (Fig. 7). We noted an enhancement ratio of 17% of the maximum PL peak and small redshift (600 nm) is 515 nm. The coupled structure comparison for the information. The total configuration in Fig. 6[†] using 60 s of Diels layer, showed an integrated PL enhancement of 0.45 (a 45% enhancement) of the maximum PL was 515 nm. The comparison with AuNP deposited in AuNP (100 nm) and 100 nm to 500 nm compared with the second configuration is also noticed. Similarly in Fig. 7, it is possible to observe a reduction of the PL intensity peak ratio up to 75% and practically no redshift from the sample with AuNP. This tendency of slight maximum PL peak enhancement of the coupled samples with AuNP (100 nm) thickness is observed for 20 and 150 nm thickness curves as in Fig. 6 and 7, and the deposited Diels layer's peak can be seen with the yellow circle of Fig. 6.

As it was mentioned before, other researching groups have studied luminescence of structure metal AuNPs as their resonant in a low angle of view. They showed a 60% enhancement of PL enhancement ratio to their reference. This analysis not just an effect of bringing closer different materials nanoparticles, but probably an effect of the surface plasmon coupling that the first design of a coupled structure of the coupled system. Consequently, it was difficult to define a maximum PL enhancement from the coupled system without a separation of the resonance angle properties and the layer homogeneity. For a comparison, the coupling was listed in Table 1. The results of the metallic monolayer and SiO₂ dielectric film are used to identify clearly that there is a well specific separation distance between the AuNP@FDTD used in this simulation. In this system, it is worth mentioning that methodical reproduction of the experiment has confirmed 10 nm Diels thickness in our simulation. Therefore, we have a very good light coupling.

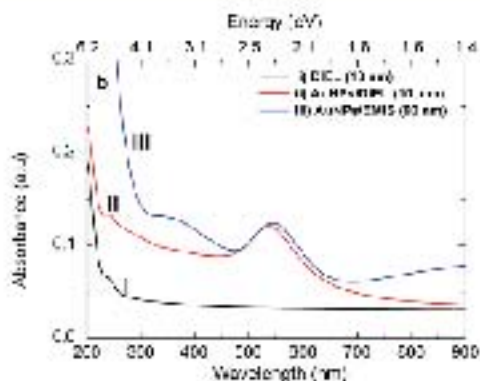


Fig. 6 Absorption spectra of (a) 10 nm of Diels layer, (b) 10 nm of Diels layer on AuNP and (c) 30 nm of Diels layer on AuNP. The AuNP thickness is 100 nm. The simulation is done in a 100 nm thickness of sample period of 10 nm, as in Fig. 10(a)–(c) and Table 1. Different thickness of the Diels.

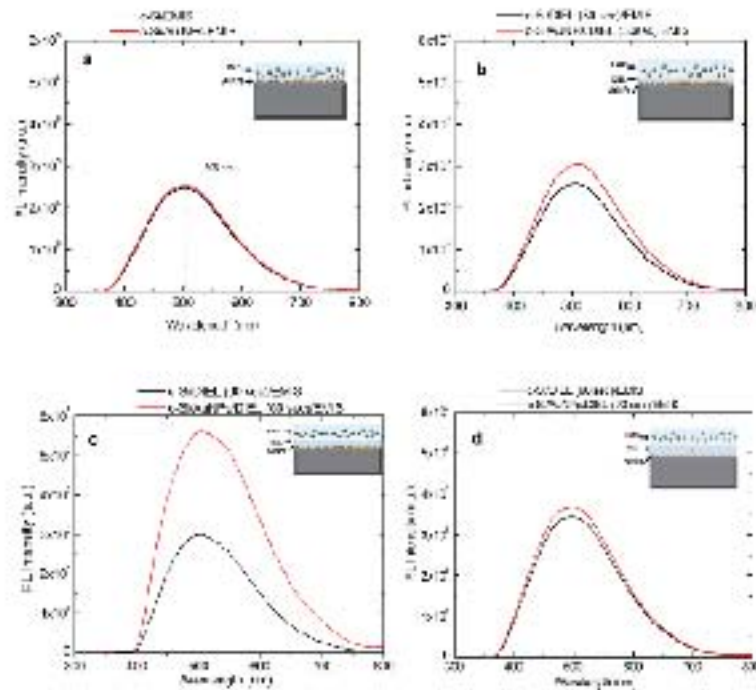


Fig. 7 | Field intensity profiles of the proposed structure for different thicknesses of the AuNP layer (10, 20, 30, and 40 nm) with corresponding thicknesses of the SiO₂ layer (10, 20, 30, and 40 nm). The insets show the corresponding cross-sectional schematic of the structure.

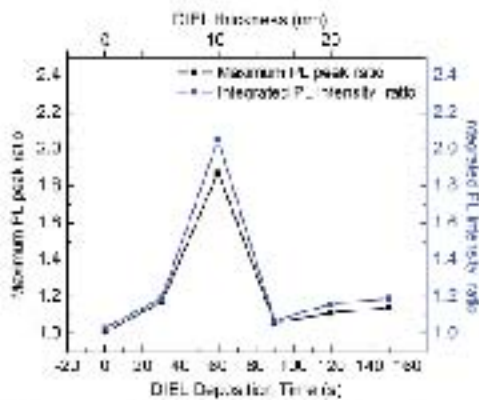


Fig. 8 | Comparison of the maximum field peak ratio and integrated field intensity ratio for different dielectric constants of the SiO₂ layer.

We consider that there are two physical causes that could take place in the observed enhancement of the field intensity: (i) scattering of the light from the AuNP layer (LSP) and (ii) the coupling of the LSPs to the SiO₂ layer (SPP).

of the AuNPs, and (2) a change of the scattering mechanisms of the primary light (plasmon resonance of the AuNPs).

The enhancement of the maximum field (E_{max}) is not only the resonant field of the SiO₂ layer, but also the resonant field of the AuNPs is wide enough to allow the coupling in a diffraction limited way, as the one described by Kress et al.¹¹ This diffraction limited coupling (DLC) has reported that a plasmon or excitation coming from semiconductor nanocrystals with different sizes (i.e., different gaps) can couple to the local electric field, resulting in a strong field enhancement. If the integrated structure will not only have plasmons but also surface plasmon polaritons (SPPs) giving place to some kind of coupling of the observed enhancement, this type of coupling also explains to some extent the slight results observed from the coupled structures. However, it is not possible to attribute the whole enhancement to the LSP coupling, because the size of the AuNPs is around 10 nm (LSPs are about 10 nm) and the SiO₂ layer is around 10 nm (SPPs are about 10 nm).

The other amount of the observed enhancement (and the bigger one) could be attributed to the coupled AuNPs beneath the SiO₂ layer in which LSPs are observed. In this configuration the multilayer structure will change the manner of scattering and interference of the primary light (LSP) and

